2-25-2024

# Characterizing the Causal Role of SVEP1 in Human Disease

Jared S. Elenbaas
*Washington University in St. Louis*

WASHINGTON UNIVERSITY IN ST. LOUIS

Division of Biology and Biomedical Sciences
Molecular Genetics and Genomics

Dissertation Examination Committee:
Nathan Stitziel, Chair
Carmen Halabi
Robert Mecham
Joel Schilling
Amber Stratman

# Characterizing the Causal Role of SVEP1 in Human Disease

by
Jared S. Elenbaas

A dissertation presented to
Washington University in St. Louis
in partial fulfillment of the
requirements for the degree
of Doctor of Philosophy

May 2024
St. Louis, Missouri

# Table of Contents

# List of Figures

# Acknowledgments

I am grateful for the support and dedication of numerous mentors who have provided me with an extensive scientific toolbox. Dr. David Arnosti provided the first opportunity for me to explore interesting biological questions. Hans Hansen taught me the principles of heredity through the lens of plant hybridization and botany. Dr. Bishr Omary gave me the confidence to pursue medical scientist training at the highest level. In conjunction with Dr. Dhiman Maitra, he taught me an array of biochemical and cellular techniques, along with the nuances of animal models and drug screening technologies. Dr. Nathan Stitziel, my PhD mentor, embodies the role of a physician scientist and taught me to use innovative translational approaches to answer critical questions related to human disease. He also developed my intellectual independence, an asset that will pay dividends in the next stages of my career. I am grateful to my thesis committee, fellow lab members, peers, and collaborators; each were also instrumental in my scientific development. I also thank the educators and administrators who enabled me to learn and grow throughout the years. I am appreciative to the numerous sources of funding that made my doctoral research possible, including F30HL152521 from the National Institutes of Health. Finally, I thank my wife and son for their love and inspiration.

Jared S. Elenbaas

*Washington University in St. Louis*

*May 2024*

Dedicated to my family.

ABSTRACT OF THE DISSERTATION

Characterizing the Causal Role of SVEP1 in Human Disease

by

Jared S. Elenbaas

Doctor of Philosophy in Biology and Biomedical Sciences

Molecular Genetics and Genomics

Washington University in St. Louis, 2024

Professor Nathan Stitziel, Chair

Sushi, von Willebrand factor type A, EGF and pentraxin domain containing 1 (SVEP1) is a poorly understood, putative extracellular matrix protein. Several human traits and diseases are associated with SVEP1, including coronary artery disease, hypertension, type 2 diabetes, glaucoma, dementia, longevity, and platelet reactivity. This dissertation establishes a causal link between SVEP1 and human disease using Mendelian randomization and mouse models. It also provides insights into the disease mechanisms of the protein, including a novel interaction between SVEP1 and the orphan receptor Platelet endothelial aggregation receptor 1. The relevance of this interaction to platelet biology and its potential role in cardiometabolic disease is discussed. The viability of inhibiting SVEP1 to treat or prevent disease is also evaluated.

# Preface

Cardiometabolic disease is the greatest cause of global mortality, according to the World Health Organization. Understanding the development of these diseases is critical to the generation of novel strategies to treat and prevent disease. Our work uses a human-first approach to addressing this problem; this aligns our questions with human biology and maximizes the applicability of its answers.

# Chapter 1

# SVEP1, an enigmatic ECM protein related to vascular biology and chronic disease

## 1.1 Abstract

Sushi, von Willebrand factor type A, EGF and pentraxin domain containing 1 (SVEP1) is a large extracellular matrix protein comprised of numerous repeat domains. The protein plays a critical role in vascular development, platelet reactivity, and human chronic disease, including coronary artery disease and dementia. SVEP1's numerous disease associations make it an intriguing candidate for therapeutic intervention. The integrin α9β1 and PEAR1 receptors interact with SVEP1 to influence cell behavior, including promoting cell adhesion and AKT/mTOR signaling, but additional binding partners likely exist. The precise mechanisms by which SVEP1 contributes to vascular biology and chronic disease remain poorly understood and should be the focus of future investigation.

## 1.2 Introduction

Sushi, von Willebrand factor type A, EGF and pentraxin domain containing 1 (SVEP1) is a poorly understood, putative extracellular matrix (ECM) protein (1, 2). Upon cloning the gene and analyzing its sequence in 2000, Gilgès et al. named it Polydom for its many domains. It is now referred to by its descriptive name, SVEP1, which was derived from its constituent domains. SVEP1 is primarily produced by mesenchymal cells and is thought to be integrated within the matrix (2, 3) (Chapter 5). The protein also circulates in plasma (4, 5). SVEP1 promotes cell

adhesion and proliferation (2, 3) (Chapter 5), but the precise mechanisms behind these SVEP1-induced cell behaviors remain poorly defined.

Recent genomic and proteomic studies have identified associations between SVEP1 and a stunning number of human diseases. Gaining a deeper understanding of this protein and how it contributes to disease is of great interest. Here, we review the human disease associations of SVEP1, the evidence supporting its role in development and disease, our limited understanding of the structure and function of the protein, and the gaps in our knowledge of the protein.

## 1.3 Associations of SVEP1 with human traits and disease

A profound number of associations between SVEP1 and human traits or diseases have been reported. Here, we will focus on those associations with the strongest supporting evidence and independent replication. In 2016, the Myocardial Infarction Genetics and CARDIoGRAM Exome Consortia Investigators reported a robust association between a coding variant in *SVEP1* (rs111245230, p.D2702G) and coronary artery disease (CAD) (6). This variant also associated with blood pressure and type 2 diabetes, but not with lipids. The SVEP1 p.D2702G variant associated with increased plasma SVEP1 (3, 7), and individuals with higher plasma levels of SVEP1 had increased incident CAD and type 2 diabetes. Plasma SVEP1 was also reported to associate with increased systolic blood pressure and poor survival post-incident CAD (7). A recent genomic study identified an association between SVEP1 and Takayasu arteritis, lending support to its potential role in vascular biology (8). A machine learning proteomic surrogate for cardiovascular outcomes includes SVEP1 as one of the top plasma proteins predictive of myocardial infarction, stroke, heart failure, or death (9).

Single nucleotide polymorphisms (SNPs) that modify plasma levels of SVEP1 can be used as instrumental variables to test whether the protein causally relates to disease. This instrumental

variable analysis is termed Mendelian Randomization (MR) and mimics a clinical trial, since confounding alleles are randomized at meiosis to isolate the exposure (plasma SVEP1, in this instance). MR of plasma SVEP1 levels suggests SVEP1 promotes type 2 diabetes (3, 7), hypertension, and CAD (3) in humans. SVEP1 is known to leak into the plasma from origin tissues (10), thus plasma SVEP1 levels may approximate its content within tissue. For this reason, the MR provides limited insight into the anatomical location of SVEP1's pathological effects but supports a causal role of SVEP1 in disease.

Another group of diseases that associate with SVEP1 is glaucoma. A separate variant within SVEP1 (rs61751937, SVEP1p.R229G) was found to associate with open angle glaucoma in a genome wide association study (GWAS) of adults (11). Another coding variant within SVEP1 (rs761025824, SVEP1p.R997C) was found in four of five affected members of a family of patients with primary congenital glaucoma and a mutation in *TEK* (12). Exposure of HUVECs to SVEP1 R997C resulted in less *TEK* expression than wildtype SVEP1, suggesting SVEP1 may modulate *TEK*-related primary congenital glaucoma (12). Deletion of *Svep1* in neural crest cells of mice resulted in defects within Schlemm's canal and increased intraocular pressure, supporting a causal role of SVEP1 in primary congenital glaucoma.

A recent MR study reported SVEP1 as the measured plasma protein with the strongest causal association with dementia (13). Additional studies have also identified genetic and proteomic associations between SVEP1 and aging or cognitive decline (9, 14, 15). For example, Lehallier et al. identified SVEP1 as the fastest accelerating plasma protein during aging (16). A causal association between plasma SVEP1 and decreased parental lifespan has also been reported (17). The same SVEP1 variant that associates with open angle glaucoma (SVEP1p.R229G) is also associated with platelet reactivity in response to adenosine di-phosphate (ADP) (18). This variant

and others within the locus containing *SVEP1* associate with additional platelet traits, including mean platelet volume and platelet count (19). We recently reported using MR that SVEP1 is causally related to these traits (Chapter 5). Variation within the locus containing SVEP1 is also associated with numerous additional hematological parameters, including red blood cell traits (20) and white blood cell counts (19). Death from septic shock also associations with SVEP1 (21), consistent with its association with hematological traits.

The disease associations are of SVEP1 are broad, but themes related to the pathophysiology of these diseases provide clues to the protein's function. Chronicity, age, and vascular dysfunction are shared characteristics of many of these disease associations, for example. Several of these diseases directly relate to vascular health, and others, including heart failure (22), glaucoma (12, 23), and dementia (24), also relate to vascular dysfunction. Animal models support a role of SVEP1 in the vasculature and will be discussed below.

## 1.4 Animal model insights into SVEP1

Mice lacking SVEP1 exhibit marked edema beginning during mid-gestation and die immediately after birth (25, 26), suggesting improper vascular development. Indeed, compared to controls, the lymphatic vessels and capillaries of these mice are significantly disrupted (25-27). Zebrafish lacking Svep1 have similar lymphatic defects, suggesting the role of SVEP1 in lymphatic development is evolutionarily conserved (25). Further studies in zebrafish have revealed a role of Svep1 in blood vessel anastomosis (28). The highly vascular placenta expresses remarkably high levels of *SVEP1* (29), consistent with a role of SVEP1 in vascular development. Further, mice lacking SVEP1 in neural crest-derived cells developed a hypomorphic Schlemm's canal and disrupted vasculature within the eye (27). Together, these data demonstrate that SVEP1 plays a broad role in vascular development. SVEP1 is thought to be expressed by mesenchymal cells and

responded to by adjacent endothelial cells (3, 25, 26), but our understanding of its developmental mechanisms remains limited.

SVEP1 is crucial for vascular patterning in mouse and zebrafish, and analysis of genetic variation within *SVEP1* in humans strongly suggests that loss of SVEP1 is not developmentally tolerated (30). However, the preponderance of diseases associated with SVEP1 are chronic and manifest after several decades of life. Prior to the proteomic and MR reports of SVEP1 in humans, we and others hypothesized that SVEP1 may protect against atherosclerosis in mice. Atherogenic mouse models of *Svep1* haploinsufficiency (3, 31) and inducible knockout of vascular smooth muscle cell-specific *Svep1* (3) were used to test this hypothesis. To our surprise, both models of SVEP1 deficiency had lower plaque burden and complexity when compared to control mice. This finding was consistent in the aortic root, aortic arch, and the whole aorta (3). MR analyses support this finding by concluding that elevated levels of SVEP1 are detrimental in human chronic disease (7, 13), including coronary artery disease (3)(Chapter 5). Interestingly, Winkler et al. concluded the opposite when using the same mouse model and phenotypic measurements (31). That study contained control and experimental groups composed of differing proportions of male and female mice, however, raising concerns of confounding (32, 33). The same study reports high levels of CXCL1 in the *Svep1*$^{+/-}$ mice. We have been unable to reproduce this finding in several model systems (3) (Chapter 5. and unpublished). Further studies will be needed to clarify the role of SVEP1 in murine atherogenesis.

Mice lacking SVEP1 post development have also been phenotyped using blood pressure measurements, vascular reactivity assays, and metabolic assays, but no significant differences were observed compared to littermate controls (Chapter 5). Complete blood counts revealed that mice lacking SVEP1 had increased lymphocytes and white blood cell counts, in addition to

increased red blood cell counts (Chapter 5). These findings overlap with the hematological associations of *SVEP1* in humans and suggest the protein may regulate hematopoiesis (19). These mice had similar platelet counts, compared to controls, but their platelets had fewer platelet pre-activation markers in response to ADP. Exogenous SVEP1 induced activation and aggregation of platelets ex vivo (Chapter 5), supporting the role of SVEP1 in promoting platelet activation. Together, these animal findings align with the human disease associations of SVEP1 and implicate the protein in vascular and platelet biology, as well as hematopoiesis.

## 1.5 The structure and function of SVEP1

The domains contained within SVEP1 have guided our hypotheses about its biological functions and remain an important consideration. SVEP1 was cloned using degenerative reverse transcriptase polymerase chain reaction for sequences that code for EGF domains (1). These domains are constituents of many ECM proteins and transmembrane receptors, including receptor tyrosine kinases and Notch family members. EGF domains often interact with each other on adjacent proteins and may depend on the availability of calcium (34). SVEP1 contains a single VWA domain, named after von Willebrand factor (35) and found in numerous ECM proteins. Many VWA domains contain metal ion-dependent adhesions sites (MIDAS) (36) and function within protein complexes (35, 37) or receptor-ligand interactions. Approximately half of SVEP1 is comprised of repeat CCP domains. CCP domains may govern protein interactions, including within the complement family (38). HYR domains are often found in association with CCPs and are also contained within SVEP1 (39). HYR domains are found within hyalin and are thought to govern cell adhesion and protein-protein interaction (39). SVEP1 also contains repeat Ephrin receptor-like domains. These domains are characteristic of the ephrin type A and B

tyrosine kinase receptors but are of uncertain function. SVEP1 also contains a number of potential glycosylation sites (40) and has been detected in glycoproteomic studies (41, 42). Recombinant murine SVEP1 is efficiently secreted from cells and is cleaved in the process (2). This generates fragments of approximately 125 and 300 kDa under reducing and denaturing conditions. We have confirmed this cleavage event and its end products in a similar expression system (3). Our size exclusion purification of recombinant, Myc-tagged SVEP1 suggests it exists in a multimeric state. We have also observed agglutination of anti-Myc magnetic beads in the presence of SVEP1 and $Ca^{2+}$, supporting multimerization.

Cellular behavior and signaling assays have provided numerous insights into our understanding of SVEP1. Exposure of cells to immobilized recombinant SVEP1 is generally the most appropriate approach to these assays, since SVEP1 is thought to be immobilized within the extracellular matrix of tissues. A variety of cells adhere to SVEP1 in a dose-dependent manner (2, 3) (Chapter 5), consistent with the functions of the domains that comprise the protein. Certain cell types also proliferate rapidly in response to SVEP1 (3). SVEP1-induced cell proliferation has been shown to depend on integrin α9β1 and Notch signaling (3); however, the specificity of these effects is unclear. Future studies will be necessary to dissect the precise mechanisms of SVEP1's effects on cell behavior.

The first and most recognized binding partner for SVEP1 is integrin α9β1 (2). ITGA9 heterodimerizes only with ITGB1 to form integrin α9β1 (43). Integrin α9β1 binds to residues 2636–2644 within a CCP domain in the C-terminus of murine SVEP1 (2). SVEP1-induced cell adhesion depends on integrin α9β1 in rhabdomyosarcoma cells (2), and integrin signaling is activated in various cells exposed to SVEP1 (3). It is unclear, however, whether the cellular effects of inhibiting integrin α9β1 in the context of SVEP1 exposure are specific to SVEP1 or

apply to integrin α9β1 more broadly. Integrin α9β1 is expressed on a wide variety of cell types, particularly muscle and epithelia (44) and is known for its role in various developmental processes, including lymphangiogenesis (45) and hematopoiesis (46) through the regulation of cell growth, migration, differentiation, and other behaviors. The phenotype of *Itga9*$^{-/-}$ mice resembles that of *Svep1*$^{-/-}$ mice but is notably milder (25, 47). Surprisingly, the zebrafish Svep1 lacks the integrin α9β1 binding domain altogether (25). Furthermore, a vascular smooth muscle cell (VSMC)-specific *Itga9*$^{-/-}$ mouse model fails to phenocopy the atherogenesis phenotypes of VMSC-specific *Svep1*$^{-/-}$ mice (Jung et al, communicated). This suggests SVEP1 has additional binding partners with relevance in vivo.

We recently demonstrated an interaction between SVEP1 and Platelet and Endothelial Aggregation Receptor 1 (PEAR1), an orphan receptor tyrosine kinase-like protein. The recombinant proteins co-immunoprecipitate and plasma levels of SVEP1 in humans are influenced by PEAR1 levels, suggesting PEAR1 sequesters SVEP1 from the plasma. SVEP1 and PEAR1 causally and concordantly relate to platelet phenotypes and CAD, consistent with their interaction being in the causal pathway for these outcomes (Chapter 5). Mice with constitutive loss of *Pear1* do not phenocopy the developmental defects observed in *Svep1*$^{-/-}$ mice, but PEAR1 has been implicated in similar biological pathways, including angiogenesis (28, 48) and platelet biology (49-51). Exposure of platelets, endothelial cells, and human coronary artery smooth muscle cells (hCAMSCs) to SVEP1 results in robust AKT/mTOR activation that is dependent on PEAR1 and its associated signaling mechanisms. This finding is of particular interest, since AKT/mTOR signaling plays a key role in the development and disease processes associated with SVEP1 (52-60).

We have also identified several basement membrane proteins that may interact with SVEP1 using a proteomic screen, suggesting the protein integrates with the basement membrane after secretion (Chapter 5). Antibodies reportedly identifying SVEP1 in situ have not been not rigorously validated, and the studies reporting staining did not include the necessary controls, such as genetic knockouts (61). The risk of false-positive SVEP1 staining is high, given that many of the domains contained within the protein are also contained within other ECM proteins. Mouse models lacking *Svep1* have a markedly more severe developmental phenotype than *Itga9* and *Pear1* knockout mice, suggesting the existence of additional binding partners and/or partial redundancy of the receptors. Additional SVEP1 binding partners have also been proposed, but their characterization remains limited. These include members of the complement (62), Notch (3), and angiopoietin family (26). Further investigation will be necessary to characterize SVEP1's tissue distribution, protein interactions, and how its interactions contribute to its biological functions. Given that cells may express multiple receptors to SVEP1, it is interesting to speculate that SVEP1 may serve as a signaling nidus and coordinate cell behavior through multiple signaling pathways.

## 1.6 Conclusions and future directions

SVEP1 is a complex and intriguing ECM protein. It plays a critical role in vascular development and chronic disease despite being less abundant than many ECM proteins. The protein is produced primarily by mesenchymal cells and likely integrated with the basement membrane, where it can influence a variety of cells. Our understanding of SVEP1 distribution in tissue is largely based on transcriptional approaches and may not accurately reflect the protein localization. A rigorous characterization of SVEP1 in situ and the reagents that purportedly detect it will be critical for future investigation. Neighboring cells, including endothelial cells,

express integrin α9β1 and/or PEAR1 and respond to SVEP1 in vitro. Future studies will be necessary to characterize additional SVEP1 binding partners and determine if and how they interact with each other. Structure-function studies will be important to map these interactions and understand their contribution to SVEP1's function.

SVEP1 can be measured in the plasma using aptamer-based proteomics; this allows for epidemiological evaluation of the protein in large cohorts of people (4, 63, 64). Genetically determined alterations in plasma levels of the protein enables causal assessments of its role in human traits and disease. These population-level data and animal models strongly support a deleterious role of SVEP1 in chronic disease, particularly of disease related to age-associated vascular dysfunction. The activation of mTOR signaling by SVEP1 in various vascular cells may underlie its association with age-related disease, since this signaling pathway is closely related to aging and disease in numerous organisms, including mammalian species (56). A therapeutic window likely exists to block SVEP1 activity, since variation of plasma SVEP1 levels is, in part, genetically determined. SVEP1 exists within the extracellular space, making SVEP1 a priority candidate therapeutic target for chronic disease.

SVEP1 is a fascinating protein that remains poorly understood. The recently discovered associations of the protein with human disease point to an underlying disease mechanism that has yet to be characterized. Future studies, described herein, will be critical in advancing our understanding of this protein's impact on human biology. This dissertation builds on this chapter, beginning with the evidence that SVEP1 promotes atherosclerosis by interacting with VSMCs. It then discusses the cardiometabolic effects of SVEP1 depletion and concludes with evidence of a novel SVEP1 interaction. The final chapter summarizes the important questions related to SVEP1 that remain unanswered.

# Chapter 2

# SVEP1 is a human coronary artery disease locus that promotes atherosclerosis[1]

## 2.1 Abstract

A low-frequency variant of sushi, von Willebrand factor type A, EGF and pentraxin domain containing protein 1 (SVEP1), an extracellular matrix protein, is associated with risk of coronary disease in humans independent of plasma lipids. Despite a robust statistical association, if and how SVEP1 might contribute to atherosclerosis remained unclear. Here, using Mendelian randomization and complementary mouse models, we provide evidence that SVEP1 promotes atherosclerosis in humans and mice and is expressed by vascular smooth muscle cells (VSMCs) within the atherosclerotic plaque. VSMCs also interact with SVEP1, causing proliferation and dysregulation of key differentiation pathways, including integrin and Notch signaling. Fibroblast growth factor receptor transcription increases in VSMCs interacting with SVEP1 and is further increased by the coronary disease associated *SVEP1* variant p.D2702G. These effects ultimately drive inflammation and promote atherosclerosis. Taken together, our results suggest that VSMC-derived SVEP1 is a pro-atherogenic factor and support the concept that pharmacological inhibition of SVEP1 should protect against atherosclerosis in humans.

## 2.2 Introduction

Cardiometabolic diseases are leading causes of morbidity and mortality, and their prevalence is increasing (65-72). Although approved treatments can help ameliorate these diseases, residual

[1] This chapter is adapted from a manuscript published in *Science Translational Medicine*, Volume 13, Issue 586 (3). https://www.science.org/doi/10.1126/scitranslmed.abe0357

disease risk remains a substantial problem. Statin medications, for example, lower plasma cholesterol concentrations and reduce risk of coronary events by 20-30% (73), highlighting both substantial residual risk and an unmet need for identifying alternative treatment strategies. Human genetics is a powerful approach to uncover potential therapeutic targets and to date more than 160 loci have been robustly associated with coronary artery disease (CAD) (74). At most loci, however, the causal gene is unknown, presenting a major bottleneck and hindering the translation of these findings into new therapies. We previously performed a large-scale exome-wide association study of low-frequency protein altering variation in an attempt to identify genes for CAD and discovered a highly conserved missense polymorphism in *SVEP1* (p.D2702G) that associated with an increased risk of disease (Odds Ratio = 1.14 per risk allele) (6). This CAD risk variant (hereafter referred to as SVEP1$^{CADrv}$) was not associated with an effect on plasma lipids but had a modest positive association with blood pressure and type 2 diabetes (6), suggesting this variant may broadly contribute to the progression of cardiometabolic disease. *SVEP1*, also known as polydom, encodes a large extracellular matrix protein with sushi (complement control protein), von Willebrand factor type A, epidermal growth factor-like (EGF), and pentraxin domains (1, 75). This gene was originally discovered in a screen for Notch-interacting proteins, as it contains Notch-like repeat EGF-domains (75). The only protein currently known to directly interact with SVEP1 is integrin α9β1 (76), a provisional matrix-binding integrin that is linked to increased blood pressure in humans (77, 78). Integrin α9β1 binds to the same protein domain that harbors the variant residue in SVEP1$^{CADrv}$ (76) and both proteins also play critical roles in development, including lymphatic patterning (79, 80). Despite strong statistical evidence linking *SVEP1* with CAD, its direct causality and potential disease-associated mechanisms were unclear. Here, we sought to determine if and how SVEP1

may influence the development of atherosclerosis. Given the overlapping disease associations between SVEP1 and integrin α9β1, their shared biological functions, and the proximity of the variant to integrin α9β1's binding site, we focused our mechanistic studies on cell types that play a prominent role in atherosclerosis and express either *SVEP1*, Integrin alpha-9 (*ITGA9*), or both genes.

## 2.3 Results

### 2.3.1 SVEP1 is expressed by arterial VSMCs under pathological conditions

To begin characterizing the role of SVEP1 in the pathogenesis of atherosclerosis, we searched for disease-relevant tissues and cell types that express *SVEP1*. Expression data from the Genotype-Tissue Expression (GTEx) project indicated that human arterial tissue, including coronary arteries, express *SVEP1* (Figure 2.1A). To confirm arterial expression, we used in situ hybridization on tissue explants from the aortic wall and left internal mammary artery (LIMA) of patients with established coronary artery disease. *SVEP1* expression was detected within cells staining with the vascular smooth muscle cell marker smooth muscle α-actin (SMα-actin) (Figure 2.2A). VSMCs are known to increase synthesis of certain extracellular matrix proteins in response to various pathological stimuli (81); therefore, we assessed expression data from relevant disease specimens to determine if this also applies to SVEP1. Indeed, *SVEP1* expression was higher within human atherosclerotic tissue from carotid explants relative to patient-paired adjacent and macroscopically intact tissue (82) (Figure 2.1B). Athero-prone arterial tissue explants from patients with diabetes also expressed more *SVEP1* compared to patients without diabetes (81) (Figure 2.1C).

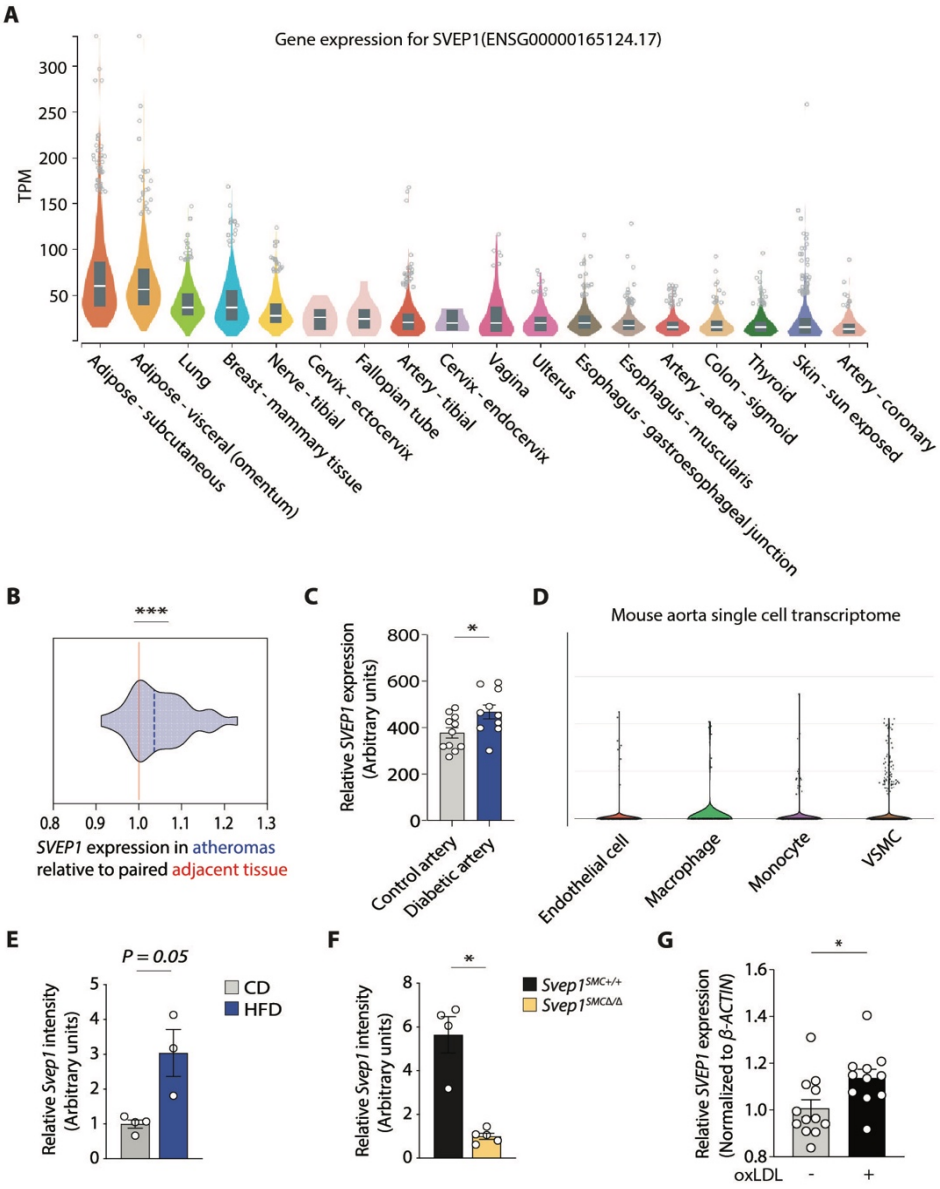


Figure 2.1 *SVEP1* expression in health and disease.
(A) Abbreviated list of human GTEx tissues in order of *SVEP1* expression. (B) *SVEP1* expression in human atherosclerotic carotid arterial tissue, relative to adjacent, paired arterial tissue. Red line represents the reference tissue. Data collected from GEO GSE43292. Paired t-test. (C) *SVEP1* expression in medial and intimal explants from control and diabetic patients. Data collected from GEO GSE13760. Two-tailed t-test. (D) *Svep1* expression in relevant cell types of the murine aorta as previously published (83). (E) Quantification of *Svep1* fluorescence intensity in murine atherosclerotic plaque. (F) Quantification of *Svep1* fluorescence intensity in plaque from $Svep1^{SMC+/+}$ and $Svep1^{SMC\Delta/\Delta}$ mice. (G) *SVEP1* expression by human CASMCs with or without the addition of oxLDL for 72 hr. $n$ = 3-5/group (E-F) or 11-12/group (G); $N$ = 3 (G). Statistical significance calculated by Mann-Whitney test (E and F) or two-tailed t-test (G). The bar graphs depict the mean ± SEM. $*P < 0.05$; $***P < 0.001$.

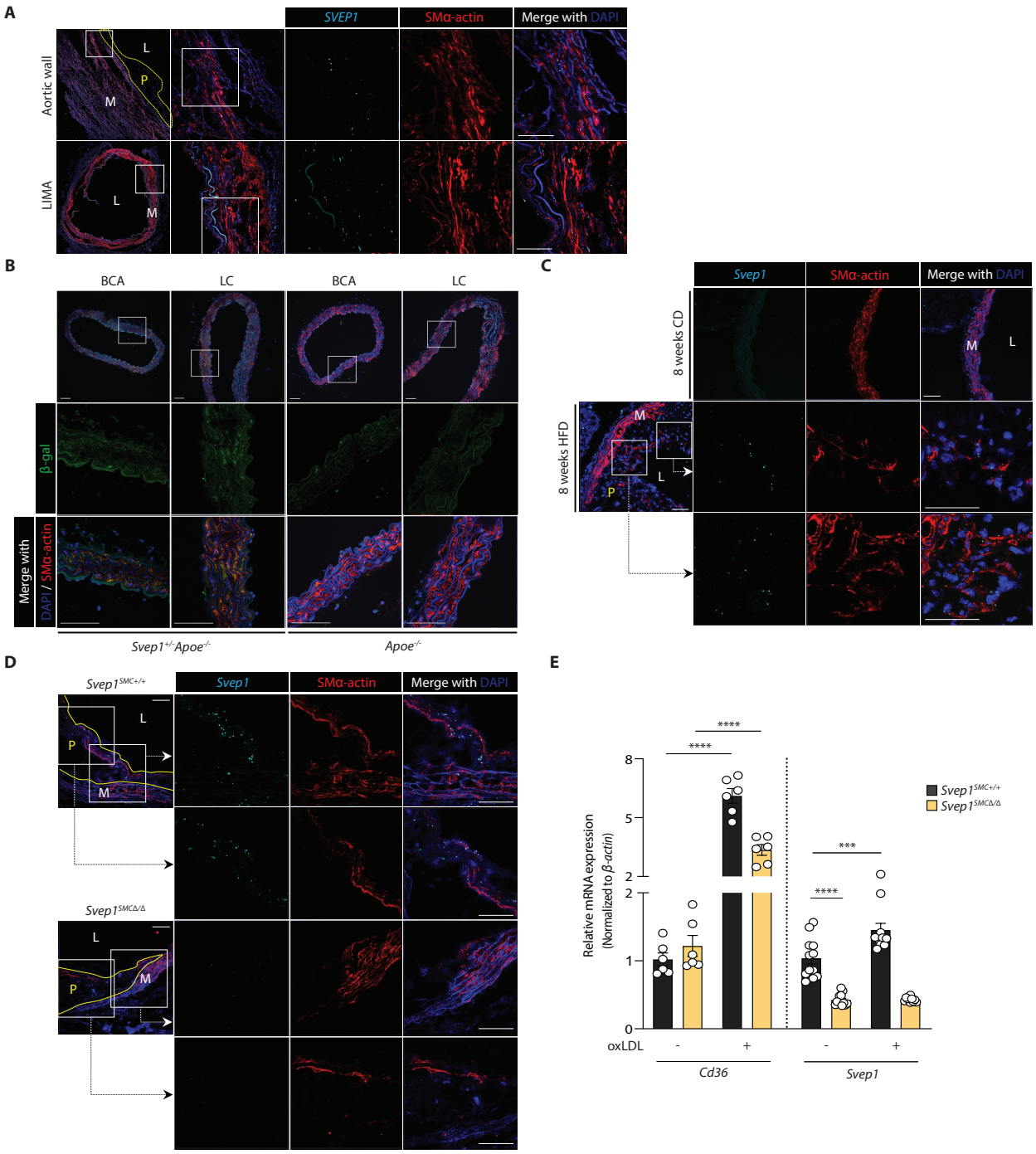


Figure 2.2 *SVEP1* is expressed by VSMCs under pathological conditions. (A) Expression of *SVEP1* in human aortic wall and LIMA cross-sections from patients using in situ hybridization (ISH). (B) β-gal expression in the aortic root, BCA (brachiocephalic artery), LC (lesser curvature) from 8-week-old *Svep1*$^{+/-}$*Apoe*$^{-/-}$ and *Apoe*$^{-/-}$ mice.(C) Expression of *Svep1* using ISH in the aortic root from young (8-week-old) CD-fed and 8 weeks of HFD-fed *Apoe*$^{-/-}$ mice. (D) Expression of *Svep1* using ISH in the aortic root from *Svep1*$^{SMC+/+}$ and *Svep1*$^{SMC\Delta/\Delta}$ mice after 8 weeks of HFD feeding. Outlined areas indicate the regions magnified in the next

panels. Tissues in (A-D) were co-stained with the VSMC marker, SMα-actin. Scale bars, 50 μm. M, media; L, lumen; P, plaque. (E) *Cd36* and *Svep1* expression in primary VSMCs from $Svep1^{SMC+/+}$ and $Svep1^{SMC\Delta/\Delta}$ mice with or without the addition of oxLDL for 48 hr ($n$ = 6-12/group, $N$ = 2). Data were analyzed with an unpaired nonparametric Mann-Whitney test. The bar graphs depict the mean ± SEM. ***$P < 0.001$; ****$P < 0.0001$.

To determine whether murine *Svep1* expression recapitulated human *SVEP1* expression, and may therefore be a viable animal model to study its effects on disease, we obtained mice expressing a lacZ reporter under the native *Svep1* promotor of a single allele because mice with homozygous *Svep1* deficiency have developmental defects and die from edema at embryonic day 18.5 (26, 79). Within healthy arterial tissue of young mice, we observed low β-gal expression, mostly colocalizing with VSMCs (Figure 2.2B). These data are consistent with published single-cell studies that identify VSMCs within the healthy murine aorta as a minor source of *Svep1* expression (83) (Figure 2.1D). To determine if murine *Svep1* expression was increased in the development of atherosclerosis, as in humans, we assayed expression within mouse arterial tissue after inducing experimental atherosclerosis by feeding atheroprone ($Apoe^{-/-}$) mice a Western, high-fat diet (HFD) for 8 weeks. $Apoe^{-/-}$ mice fed a standard chow diet (CD) served as non-atherogenic controls. After 8 weeks of an atherogenic HFD, we observed a 2-fold increase in *Svep1* expression relative to CD fed control mice (Figure 2.2C, 2.1E). This expression was colocalized with neointimal cells that co-stained with SMα-actin, suggesting VSMC expression (Figure 2.2C).

Multiple cell types have been demonstrated to gain expression of VSMC markers in the context of atherosclerosis (84). Therefore, to test the hypothesis that VSMC-derived cells within the neointima are the predominate source of SVEP1, we generated $Apoe^{-/-}$ mice with VSMC-specific knockout of *Svep1* ($Svep1^{flox/flox}Myh11\text{-}Cre^{ERT2}Apoe^{-/-}$; hereafter referred to as $Svep1^{SMC\Delta/\Delta}$) and mice with unaltered *Svep1* expression ($Svep1^{+/+}Myh11\text{-}Cre^{ERT2}Apoe^{-/-}$; hereafter referred to as

*Svep1*$^{SMC+/+}$), which served as controls. *Svep1* expression was assessed using in situ hybridization within the neointima of the aortic root of both groups after 8 weeks of HFD feeding. Indeed, while we observed robust *Svep1* expression in control mice, neointimal *Svep1* expression was nearly undetectable in *Svep1*$^{SMC\Delta/\Delta}$ mice (Figure 2.2D, 2.1F). These data indicate that VSMC-derived cells are the predominant source of SVEP1 in atherosclerotic plaque.

Given the increased expression of *Svep1* under atherosclerotic conditions in mice and humans, we tested the ability of atheroma-associated oxidized low-density lipoprotein (oxLDL) to directly induce *Svep1* expression in VSMCs. Exposure to oxLDL increased *Svep1* expression by 48% in primary VSMCs from *Svep1*$^{SMC+/+}$ mice but not *Svep1*$^{SMC\Delta/\Delta}$ mice, compared to vehicle-treated control cells (Figure 2.2E). Both *Svep1*$^{SMC+/+}$ and *Svep1*$^{SMC\Delta/\Delta}$ cells increased expression of *Cd36*, indicating they were activated upon binding of oxLDL with its receptor (85). Exposure to oxLDL also modestly induced *SVEP1* expression in human primary coronary artery smooth muscle cells (CASMCs, not shown).

Taken together, these data demonstrate that *SVEP1* is produced locally by VSMCs in atherosclerotic disease and are consistent with prior studies which concluded that SVEP1 is produced by cells of mesenchymal origin (26, 79). Further, these data suggest that SVEP1 may play a direct role in the pathogenesis of atherosclerosis and that mouse models are an appropriate means to interrogate this question.

### 2.3.2 SVEP1 drives atherosclerotic plaque development

To study the effect of *Svep1* on atherosclerosis, we fed *Apoe*$^{-/-}$ and *Svep1*$^{+/-}$*Apoe*$^{-/-}$ mice a HFD for 8 weeks and analyzed the resulting atherosclerotic plaque burden. There were no observed differences between genotypes in body weight, plasma total cholesterol, triglycerides, and glucose (Figure 2.3A, B). Relative to controls, however, *Svep1*$^{+/-}$*Apoe*$^{-/-}$ mice had a reduction in

plaque burden (as characterized by the percentage of surface area staining positive with Oil Red O) in the aortic arch and whole aorta by en face preparations, as well as in sectioned aortic roots (Figure 2.3C, D). The effect of *Svep1* haploinsufficiency on reducing the development of atherosclerotic plaque in the aortic arch and en face aorta was notably greater than in the aortic root, perhaps reflecting differences in VSMC embryonic origin and biology (86). *Svep1* haploinsufficiency also resulted in reduced macrophage staining within the aortic root neointima, as determined by the percentage of area staining positive for Mac3 (Figure 2.3E). We did not appreciate marked differences in measures of plaque stability, such as area staining positive for VSMC markers or necrotic core size, although collagen content was modestly higher in atheromas from control mice compared to *Svep1*$^{+/-}$*Apoe*$^{-/-}$ mice (Figure 2.4).

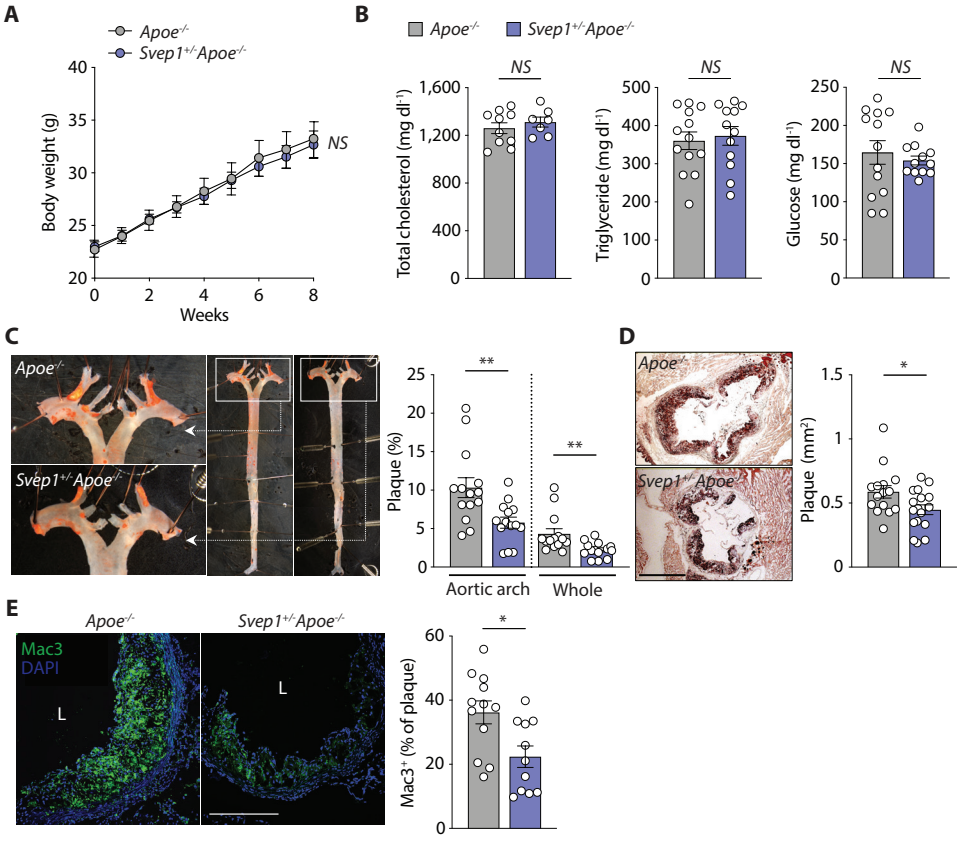


Figure 2.3 *Svep1* haploinsufficiency abrogates atherosclerosis.

(A) Body weight of *Apoe*$^{-/-}$ and *Svep1*$^{+/-}$*Apoe*$^{-/-}$ mice during HFD feeding. (B) Plasma total cholesterol, triglycerides, and glucose of mice after HFD feeding. (C) En face Oil Red O-stained murine aortas. Outlined areas indicate the aortic arch regions magnified in left panels. Quantification of Oil Red O-stained area in each aortic arch and whole artery. (D) Oil Red O-stained murine aortic root cross-sections. Quantification of Oil Red O-stained area. Scale bar, 500 µm. (E) Mac3 staining in murine aortic root sections. Quantification of Mac3 as a percentage of plaque area. Scale bar, 200 µm. M, media; L, lumen; P, plaque. $n$ = 7-17/group (A-E). Data were analyzed with a one-way ANOVA (A) or unpaired nonparametric Mann-Whitney test (B-E). The bar graphs depict the mean ± SEM. *$P$ < 0.05; **$P$ < 0.01; *NS*, not significant.

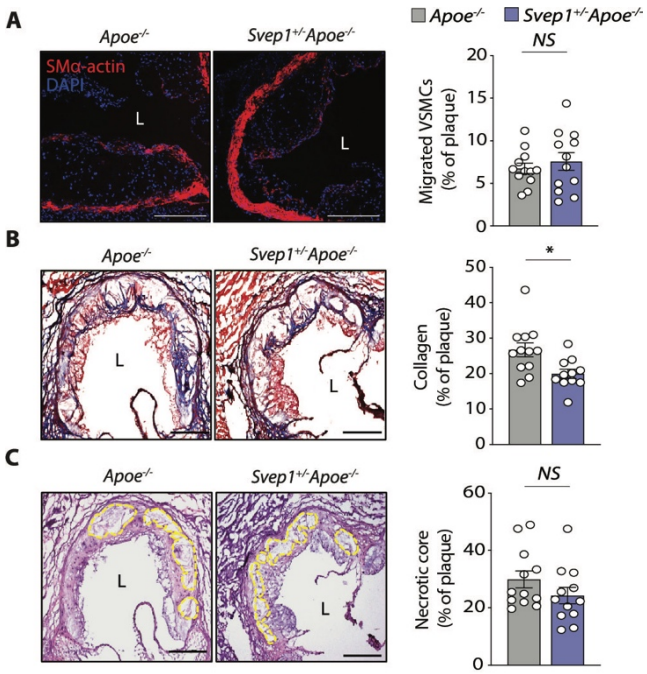


Figure 2.4 *Svep1* haploinsufficiency does not significantly alter plaque composition after 8 weeks of HFD feeding.
(A) SMα-actin staining of murine aortic roots. Quantification of area staining for SMα-actin as a percentage of plaque is shown on the right. Scale bar, 500 µm. (B) Collagen staining of murine aortic roots using by Masson's trichrome. Quantification of collagen as a percentage of plaque area is shown on right. (C) Necrotic core outlined on H&E-stained murine aortic roots. Quantification of necrotic core area as a percentage of plaque area shown on right. $n$ = 11-12/group (A-C). Scale bars in B and C, 200 µm. L, lumen. All data were analyzed with unpaired nonparametric Mann-Whitney test, and shown as the mean ± SEM. *$P$ < 0.05; *NS*, not significant.

We then tested the hypothesis that the atherogenic effects of SVEP1 could be attributed to its synthesis by VSMCs using *Svep1*$^{SMC\Delta/\Delta}$ and *Svep1*$^{SMC+/+}$ mice, as previously described. As with

*Svep1* haploinsufficiency, loss of *Svep1* in VSMCs did not significantly alter body weight, plasma cholesterol, triglycerides and glucose concentrations (Figure 2.5A, B) following 8 weeks of HFD feeding. Also consistent with our *Svep1* haploinsufficiency model, *Svep1*$^{SMC\Delta/\Delta}$ mice had decreased plaque burden plaque in the aortic arch, whole aorta, and aortic root (Figure 2.5C, D), as compared to *Svep1*$^{SMC+/+}$ control mice. Additionally, atheromas from *Svep1*$^{SMC\Delta/\Delta}$ mice contained less macrophage staining and necrotic core area, indicators of plaque instability, and unaltered collagen content (Figure 2.6A-C).

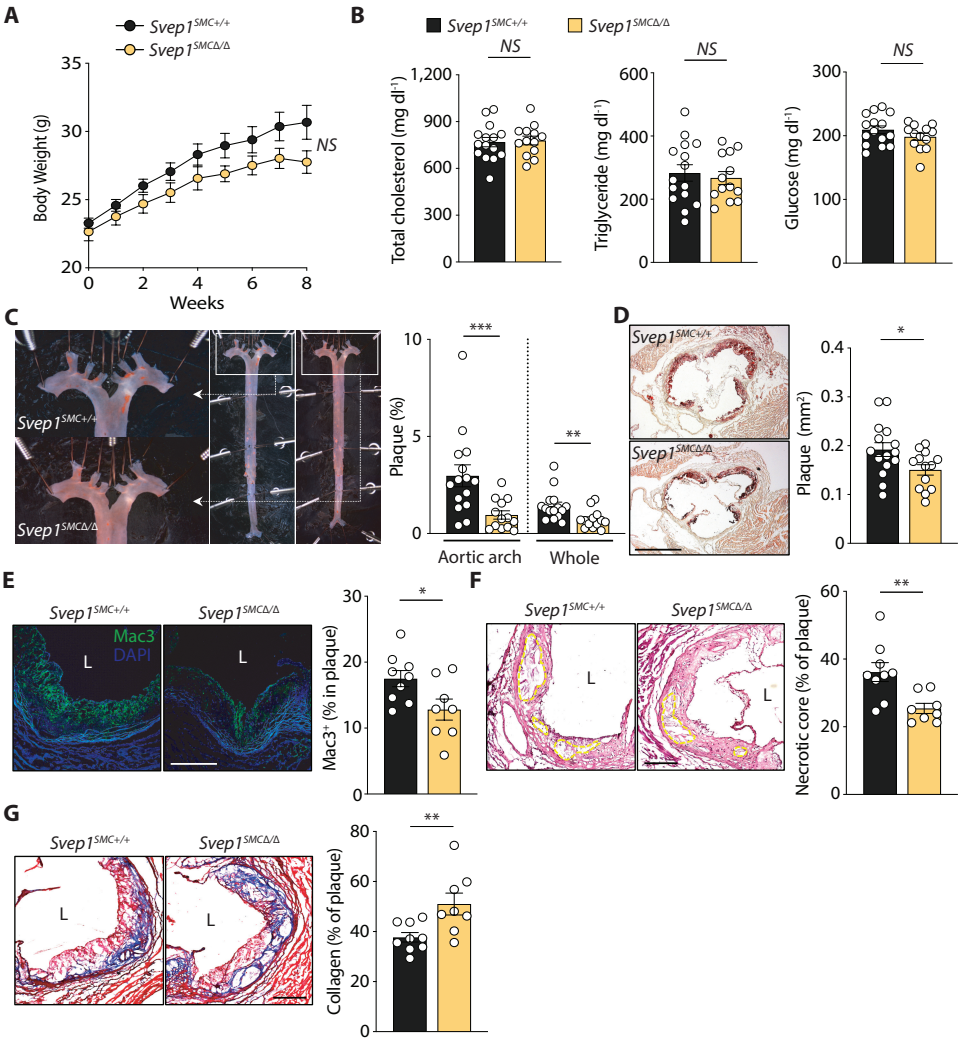


Figure 2.5 VSMC-specific *Svep1* deficiency reduces atherosclerosis and plaque complexity. (A) Body weight of *Svep1*$^{SMC+/+}$ and *Svep1*$^{SMC\Delta/\Delta}$ mice during HFD feeding. (B) Total plasma cholesterol, triglycerides, and glucose in mice. (C) En face Oil Red O-stained murine aortas.

Outlined areas indicate the aortic arch regions magnified in left panels. Quantification of Oil Red O-stained area in each aortic arch and whole artery. (D) Oil Red O-stained murine aortic root cross-sections. Quantification of Oil Red O-stained area. Scale bar, 500 µm. (E) Mac3 staining of murine aortic roots. Quantification of Mac3 as a percentage of plaque area. (F) Necrotic core of murine aortic roots outlined on H&E-stained sections. Quantification of necrotic core as a percentage of plaque area. (G) Collagen staining of murine aortic roots using Masson's trichrome stain. Quantification of collagen as a percentage of plaque area. Scale bars, 200 µm. M, media; L, lumen; P, plaque. *n* = 13-15/group (A- D) or 8-9/group (E-G). Data were analyzed with a one-way ANOVA (A) or unpaired nonparametric Mann-Whitney test (B-G). The bar graphs depict the mean ± SEM. **P* < 0.05; ***P* < 0.01; ****P* < 0.001; *NS*, not significant.

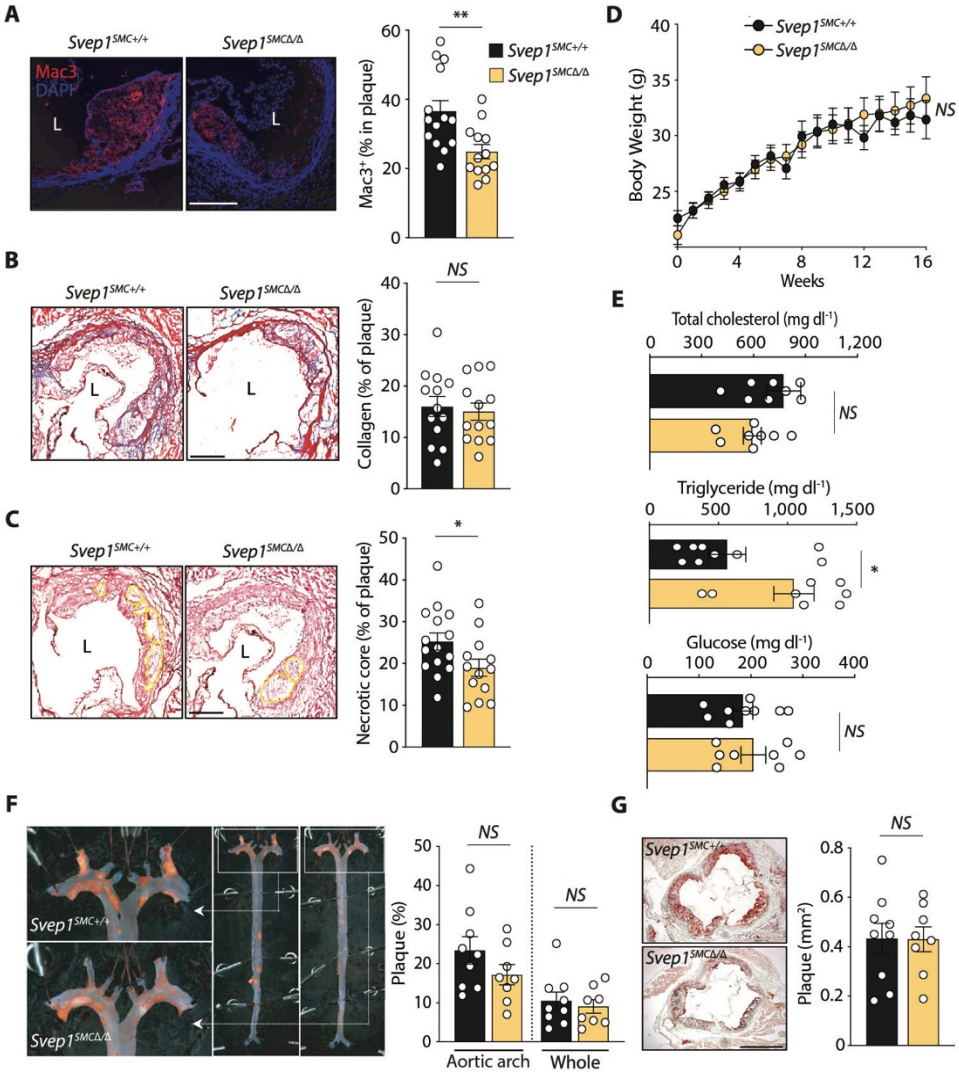

Figure 2.6 VSMC-specific *Svep1* deficiency reduces atherosclerosis and plaque complexity, continued.
(A) Mac3 staining of murine aortic root. (B) Collagen staining of murine aortic root by Masson's trichrome stain.(C) Necrotic core of murine aortic root outlined on H&E-stained sections, quantification of respective parameters on the right of each image (A-C). (D) Body weight of $Svep1^{SMC+/+}$ and $Svep1^{SMC\Delta/\Delta}$ mice during HFD feeding. (E) Plasma total cholesterol, triglycerides, and glucose from mice. (F) En face Oil Red O-stained murine aortas. Outlined areas indicate the aortic arch regions magnified in left panels. Quantification of Oil Red O-stained area in each aortic arch and whole artery. (G) Oil Red O-stained murine aortic root cross-sections. Quantification of Oil Red O-stained area. $n$ = 8-15/group (A-G). Scale bars, 50 μm (in A), 200 μm (in B and C), 500 μm (in G). 8 weeks of HFD feeding (A-C), and 16 weeks of HFD feeding (D-G). Data were analyzed with One-way ANOVA test (D) or unpaired nonparametric Mann-Whitney test (A-C, E-G) and shown as the mean ± SEM. *$P < 0.05$; **$P < 0.01$; *NS*, not significant.

Given the observations that loss of *Svep1* in VSMCs resulted in a dramatic reduction in plaque size in the setting of 8 weeks of HFD feeding, we extended the length of plaque development to investigate the effect of SVEP1 on advanced plaque lesions. After treatment with tamoxifen, $Svep1^{SMC+/+}$and $Svep1^{SMC\Delta/\Delta}$ mice were fed HFD for 16 weeks. Again, no differences were observed in body weight (Figure 2.6D), plasma cholesterol, and glucose concentrations (Figure 2.6E) between groups. Triglycerides were higher in the $Svep1^{SMC\Delta/\Delta}$ mice with nominal significance ($P = 0.046$), but this was not observed at other timepoints or in the haploinsufficiency model. Although we did not detect a statistically significant effect of VSMC-specific *Svep1* deletion on atherosclerotic plaque burden (Figure 2.6F, G), plaques from $Svep1^{SMC\Delta/\Delta}$ mice tended to be smaller and were both less complex and more stable than controls. These indicators of an altered plaque phenotype include decreased neointimal macrophage staining (Figure 2.5E) and necrotic core size (Figure 2.5F), in addition to greater collagen content (Figure 2.5G). Taken together, these experimental atherosclerosis data suggest that SVEP1 drives atherosclerosis and increases plaque complexity in mice.

### 2.3.3 SVEP1 is causally related to cardiometabolic disease in humans

Due to the relationship we discovered between SVEP1 depletion and reduced atherosclerosis across our mouse models, we wondered if the human *SVEP1* CAD-associated D2072G missense polymorphism was associated with altered SVEP1 expression in humans. We did not find that this allele (or other alleles in linkage disequilibrium) associated with changes in *SVEP1* mRNA expression in GTEx (Figure 2.7A), however we did find that the 2702G risk variant ($SVEP1^{CADrv}$) was associated with a significant increase in circulating plasma SVEP1 protein concentration ($P = 8 \times 10^{-14}$; Figure 2.8A) as measured by two independent aptamers (Figure 2.7B) from participants in the INTERVAL study (4), suggesting that increased SVEP1 protein concentrations were associated with increased risk of CAD. We then tested if this was true for other genetic variants influencing SVEP1 plasma protein concentrations. Using published data from the INTERVAL study (4), we cataloged *cis*-acting variants that associated with SVEP1 protein concentration at a genome-wide ($P < 5 \times 10^{-8}$) level of statistical significance (Figure 2.8B). We performed Mendelian randomization (87) using a subset of these variants in linkage equilibrium ($r^2 < 0.3$) and found that increased SVEP1 protein was causally related to increased CAD risk ($P = 7 \times 10^{-11}$; Figure 2.8C, D). We also asked if SVEP1 protein concentration was causally related to increased risk for hypertension and type 2 diabetes due to the prior associations we observed for the $SVEP1^{CADrv}$ allele with these risk factors. Indeed, we found that increased SVEP1 protein was causally related to both hypertension ($P = 2 \times 10^{-15}$; Figure 2.7C) and type 2 diabetes ($P = 0.0004$; Figure 2.7D).

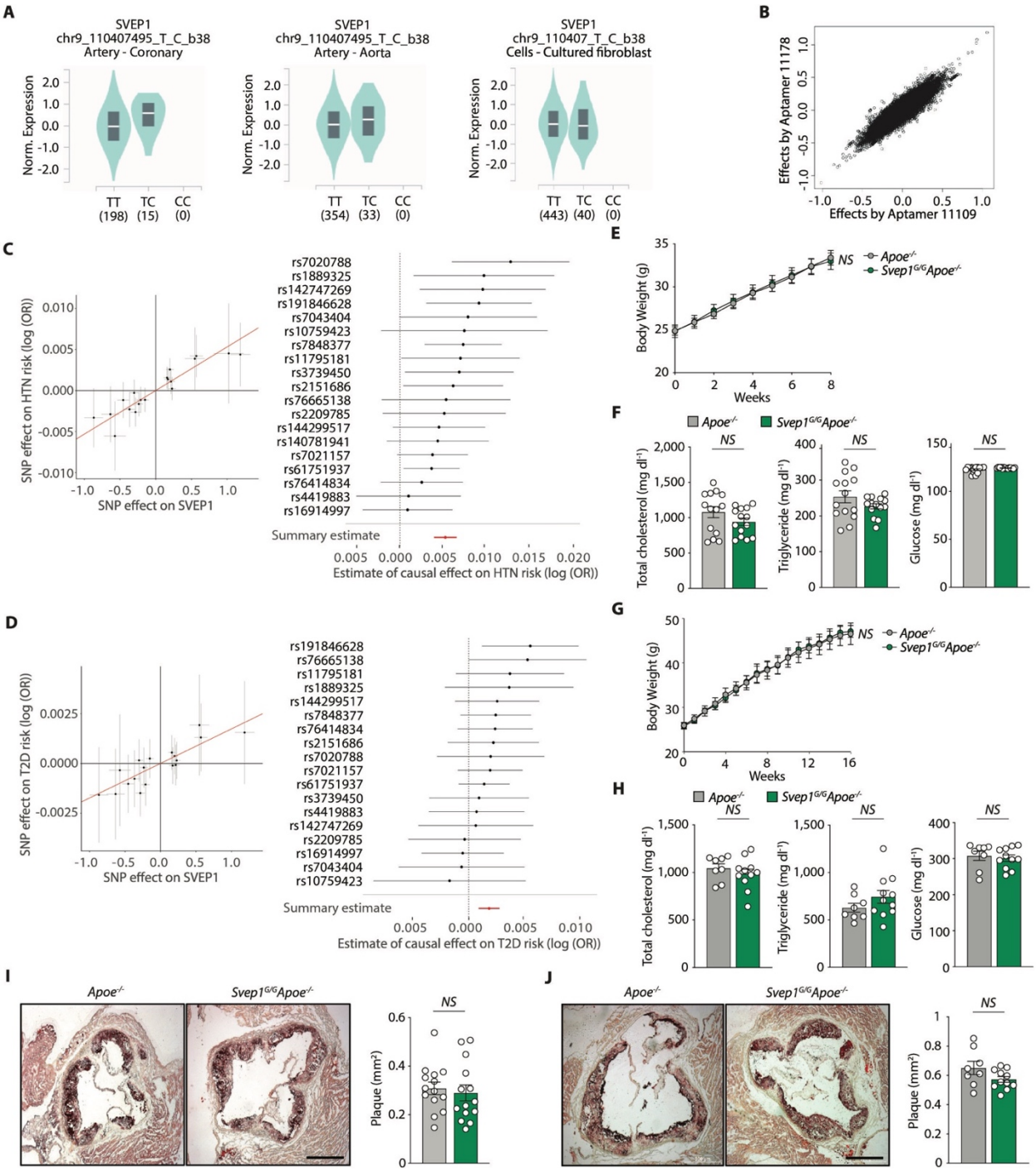


Figure 2.7 The effect of the CAD-associated *SVEP1* D2702G missense polymorphism and SVEP1 protein concentration in humans and mice.

(A) Relative mRNA expression by genotype as measured in the GTEx project. There is no significant difference in *SVEP1* expression by *SVEP1* D2702 genotype in coronary artery ($P$ = 1.0), aorta ($P$ = 0.32), or cultured fibroblasts ($P$ = 0.9), with the latter being included as it is the highest expressing cell sample in GTEx. All GTEx data are from human cells or tissues. (B) The effect of each chromosome 9 variant on human plasma SVEP1 protein concentration as estimated by the SVEP1.11109.56.3 and SVEP1.11178.21.3 aptamers. (C, D) The respective leftward panels indicate the estimated effect (with 95% confidence intervals) of each variant included in the Mendelian randomization analysis on plasma SVEP1 expression and risk of hypertension (HTN, C) or type 2 diabetes (T2D, D). The red line indicates the causal effect estimate ($P = 2 \times 10^{-15}$ for HTN; $P$ = 0.0004 for T2D). The respective rightward panels indicate the estimated causal effect (with 95% confidence intervals) of each single nucleotide polymorphism (SNP) included in the Mendelian randomization analysis for a one unit increase in SVEP1 concentration. These are plotted along with the overall summary estimate from the causal analysis. (E) Body weight of $Apoe^{-/-}$ and $Svep1^{G/G}Apoe^{-/-}$ mice during 8 weeks of HFD. (F) Total plasma cholesterol, triglyceride and glucose of mice after 8 weeks of HFD. (G) Body weight of $Apoe^{-/-}$ and $Svep1^{G/G}Apoe^{-/-}$ mice during 16 weeks of HFD. (H) Total plasma cholesterol, triglyceride and glucose of mice after 16 weeks of HFD. Oil Red O-stained aortic root cross-sections of mice after 8 weeks of HFD (I), and 16 weeks of HFD (J). Quantification of Oil Red O-stained area in murine aortic root sections. $n$ = 8-14/group (E-J). Scale bar, 500 μm (in I and J). The bar graphs depict the mean ± SEM. *NS*, not significant.

A

| rsID | Reference allele | Alternate allele | Protein impact | Effect | *P* value |
|---|---|---|---|---|---|
| rs11124523 | T | C | SVEP1 D2702G | 0.48 | $8 \times 10^{-14}$ |

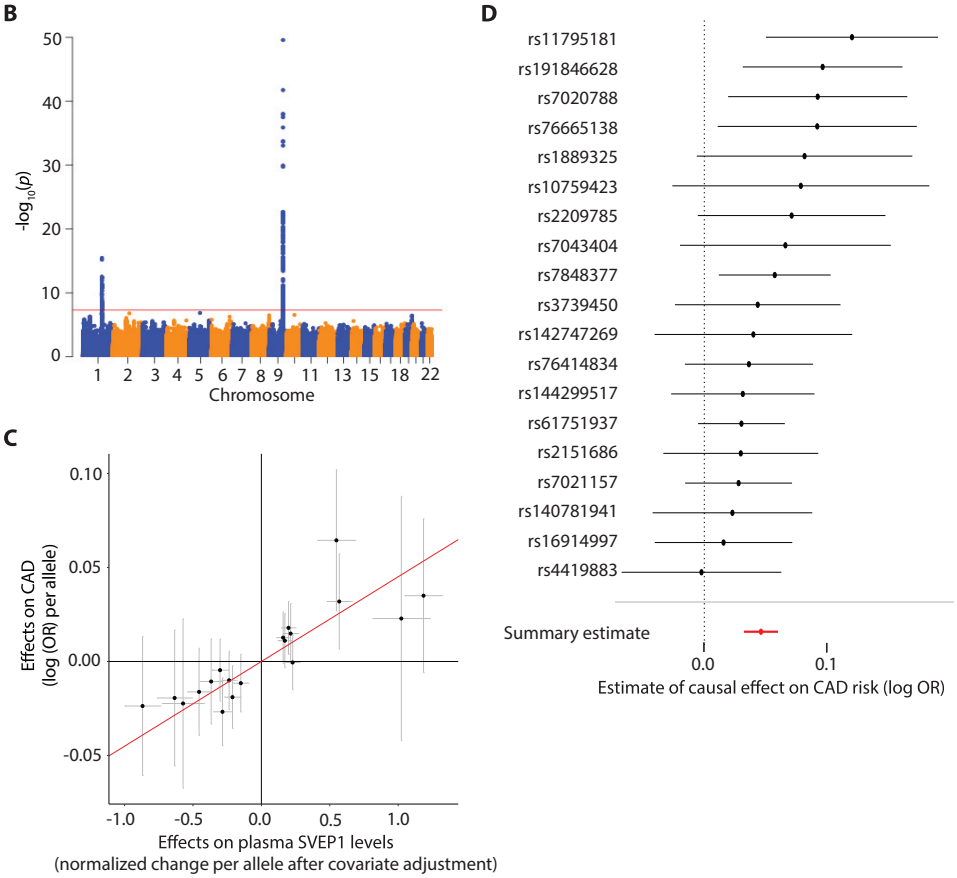


Figure 2.8 Plasma SVEP1 is causally related to CAD in humans.
(A) The effect of the CAD-associated *SVEP1* p.D2702G allele on plasma SVEP1 expression in humans. Effect refers to the change per alternative allele (2702G) in units of normalized protein concentration after adjusting for covariates as previously described (4). (B) Genome-wide Manhattan plot for variants associated with plasma SVEP1 in humans. The $-\log_{10}(P)$ of the association with SVEP1 concentration is plotted for each variant across the genome according to chromosomal position (X-axis). The red line indicates genome-wide significance ($P < 5 \times 10^{-8}$). The association peak on chromosome 9 overlies the *SVEP1* locus. (C) Estimated effect (with 95% confidence intervals) of each variant included in the Mendelian randomization analysis on plasma SVEP1 expression and CAD risk. The red line indicates the causal effect estimate ($P = 7 \times 10^{-11}$). (D) The estimated causal effect (with 95% confidence intervals) of each SNP included in the Mendelian randomization analysis for a one unit increase in SVEP1 concentration is plotted along with the overall summary estimate from the causal analysis.

To investigate how the human SVEP1$^{CADrv}$ missense polymorphism might impact CAD risk, we generated homozygous mice harboring the human SVEP1$^{CADrv}$ at the orthologous murine

position (*Svep1*$^{2699G/2699G}$; hereafter referred to as *Svep1*$^{G/G}$). These mice were bred with *Apoe*$^{-/-}$ mice to generate *Svep1*$^{G/G}$*Apoe*$^{-/-}$ mice. We were not able to detect differences in body weight, serum total cholesterol, triglycerides, and glucose (Figure 2.7E-H) between groups after feeding HFD. We also did not appreciate a significant difference between groups in the development of atherosclerotic plaque at either 8 or 16 weeks of HFD feeding (Figure 2.7I, J). Although our prior human genetic study revealed a robust association with an increased risk of CAD, the effect of the SVEP1$^{CADrv}$ in humans was modest, in which each copy of the G allele was associated with a 14% increased risk of disease. If an effect size in mice is similarly modest, further investigation would require a very large number of animals, presenting both pragmatic and ethical barriers. To circumvent these concerns, subsequent functional interrogation of the SVEP1$^{CADrv}$ was performed in vitro.

### 2.3.4 SVEP1 induces proliferation and integrin signaling in VSMCs

To begin characterizing the mechanism by which SVEP1 drives atherosclerosis, we sought to identify receptors and associated cell types that interact with SVEP1 in the extracellular space. Integrin α9β1 is the only protein known to interact with SVEP1 and the two proteins colocalize in vivo (76). Integrins are transmembrane, heterodimeric receptors that respond to the extracellular environment and influence numerous aspects of atherosclerosis (88, 89). Therefore, we hypothesized that integrin α9β1 (and associated cell-types) may be involved in SVEP1-mediated atherosclerosis. The α9 subunit (ITGA9) is known to exclusively heterodimerize with β1 (ITGB1), therefore assessing *ITGA9* expression is a reliable proxy for integrin α9β1 expression. Integrin α9β1 expression has been documented in airway epithelium, smooth muscle, skeletal muscle, hepatocytes, and epithelial cells (76, 90-96), yet arterial tissue expresses the most *ITGA9* of all GTEx tissues (Figure 2.9A). In situ hybridization confirmed that *ITGA9* is

broadly expressed in the human aortic wall and LIMA, predominately colocalizing with VSMCs (Figure 2.10A). Likewise, VSMCs of the murine aorta expressed *Itgα9* (Figure 2.10B). Consistent with these data, single cell studies of the murine aorta indicated that VSMCs express *Itgα9* (Figure 2.9B) (83). Given the established role of VSMCs in CAD (84), their expression of integrin α9β1, and the local expression patterns of SVEP1 in disease, we tested the hypothesis that VSMCs respond to SVEP1 in a cell-autonomous manner to promote atherosclerosis.

The extracellular matrix (ECM) plays a critical role in orchestrating cellular responses to tissue injury, including promoting cell proliferation and differentiation (84, 97). We therefore assessed the proliferation of neointimal *Svep1*$^{SMC\Delta/\Delta}$ and *Svep1*$^{SMC\ +/+}$ VSMCs using immunofluorescent staining of the proliferation marker mini-chromosome maintenance protein-2 (MCM-2). Among cells expressing smooth muscle actin, fewer stained positive for MCM-2 in *Svep1*$^{SMC\Delta/\Delta}$ mice as compared to *Svep1*$^{SMC\ +/+}$ controls after HFD feeding for 8 weeks (Figure 2.10C), suggesting SVEP1 induces VSMC proliferation.

To further explore the effects of SVEP1 on VSMCs, we generated and purified recombinant SVEP1 and its orthologous CAD risk variant (SVEP1$^{CADrv}$) using a mammalian expression system. We tested the response of primary VSMCs to SVEP1 that was immobilized on culture plates, reflecting an overexpression-like assay while maintaining its physiologic context as an extracellular matrix protein (in contrast to genetic overexpression). VSMCs adhered to SVEP1 in a dose dependent manner (Figure 2.10D). Exposure to both SVEP1 variants induced dose-dependent VSMC proliferation, based on bromodeoxyuridine (BrdU) incorporation (Figure 2.10E). As a point of reference, we used oxLDL, a proliferative stimulus relevant to atherosclerosis, in addition to SVEP1 to test VSMC proliferation; strikingly, SVEP1 induced more VSMC proliferation than oxLDL (Figure 2.10F). Exposure to a combination of oxLDL and

SVEP1, as exists within the atheromatous environment, caused the greatest amount of VSMC proliferation (Figure 2.10F). Human coronary artery smooth muscle cells (CASMCs) also proliferated in response to SVEP1 (Figure 2.9C). Murine macrophages exposed to SVEP1 did not proliferate in the absence or presence of oxLDL (Figure 2.9D), suggesting that SVEP1 is not a proliferative stimulus for all cell types.

Integrin α9β1 is expressed by VSMCs, binds to SVEP1, and drives proliferation in some cell types (90). Therefore, to begin to interrogate the molecular mechanisms by which SVEP1 influences VSMCs, we tested whether SVEP1 exposure could induce integrin signaling in VSMCs. We seeded cells to wells coated with bovine serum albumin (as an inert protein control), Vascular cell adhesion molecule 1 (VCAM-1, a low affinity integrin α9β1 ligand), or SVEP1 (a high affinity integrin α9β1 ligand). Cells adherent to SVEP1 had increased phosphorylation of canonical integrin signaling kinases, such as focal adhesion kinase (FAK), Paxillin (Pax), and Src, as well as downstream MAPK kinases, ERK and p38 (Figure 2.10G), relative to an inert protein control. SVEP1$^{CADrv}$ had similar effects as SVEP1 on integrin signaling in VSMCs (Figure 2.9E). We then tested if SVEP1-induced proliferation was dependent on integrin α9β1. Since Itgα9 exclusively heterodimerizes with Itgβ1, we used siRNA knockdown of *Itgα9* to disrupt integrin α9β1. The proliferative effect of SVEP1 was completely inhibited by knockdown of *Itgα9* using two different siRNA constructs (Figure 2.10H), suggesting that integrin α9β1 is necessary for SVEP1-induced VSMC proliferation.

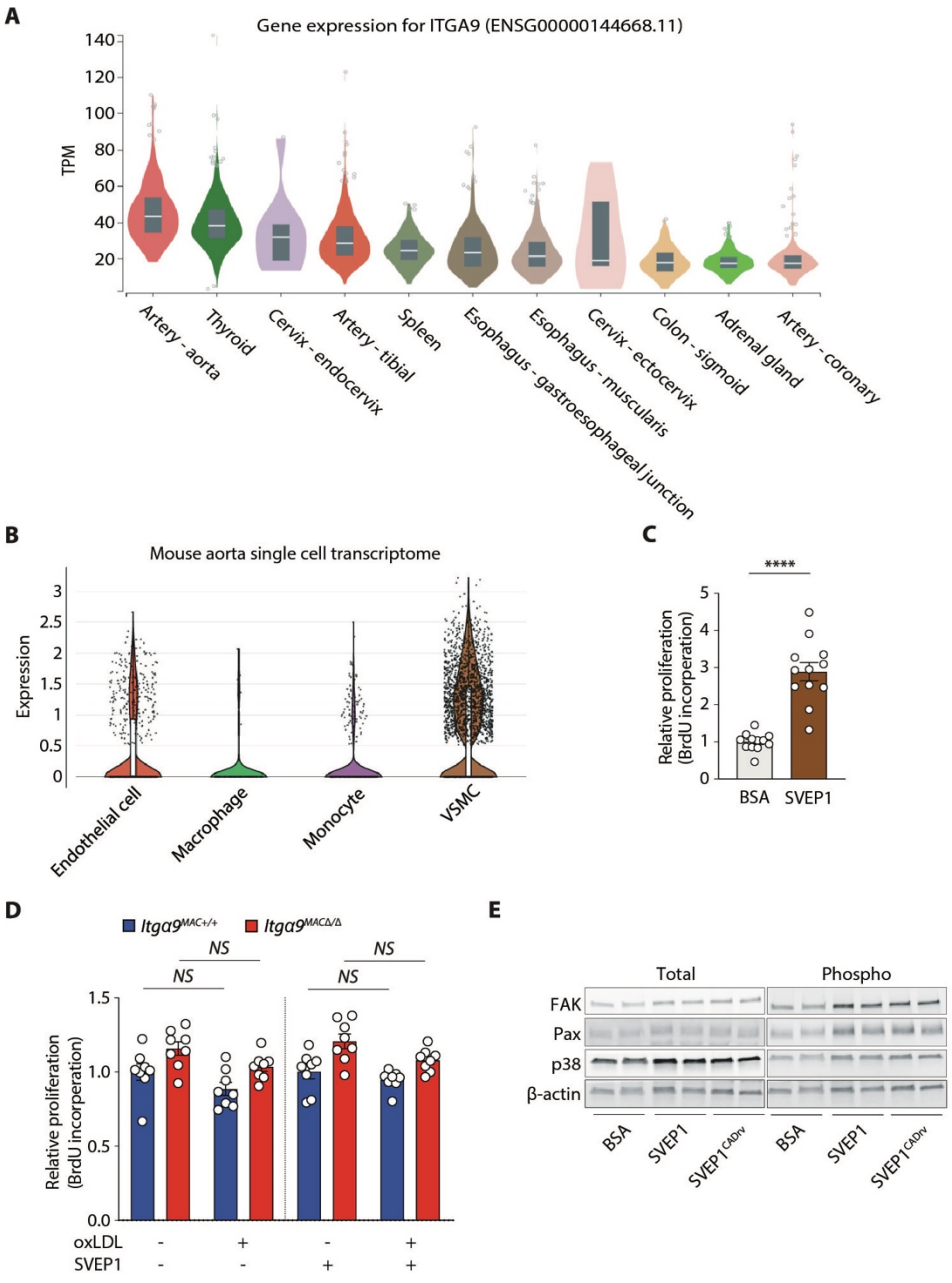
A
Gene expression for ITGA9 (ENSG00000144668.11)
TPM
140
120
100
80
60
40
20
Artery - aorta
Thyroid
Cervix - endocervix
Artery - tibial
Spleen
Esophagus - gastroesophageal junction
Esophagus - muscularis
Cervix - ectocervix
Colon - sigmoid
Adrenal gland
Artery - coronary
B
Mouse aorta single cell transcriptome
Expression
3
2.5
2
1.5
1
0.5
0
Endothelial cell
Macrophage
Monocyte
VSMC
C
****
Relative proliferation (BrdU incorperation)
5
4
3
2
1
0
BSA
SVEP1
D
Itgα9MAC+/+
Itgα9MACΔ/Δ
NS
NS
NS
NS
Relative proliferation (BrdU incorperation)
1.5
1.0
0.5
0.0
oxLDL - + - +
SVEP1 - - + +
E
Total
Phospho
FAK
Pax
p38
β-actin
BSA
SVEP1
SVEP1CADlv
BSA
SVEP1
SVEP1CADlv

Figure 2.9 *Itgα9* is expressed in both VSMCs and macrophages in mouse arteries. (A) Abbreviated list of human GTEx tissues in order of *ITGA9* expression. (B) *Itgα9* expression in the murine aorta. Data collected from (83). (C) Proliferation of human CASMCs in response to immobilized SVEP1. Statistical significance calculated by two-tailed t-test. (D) Proliferation of murine $Itga9^{MAC+/+}$ and $Itga9^{MAC\Delta/\Delta}$ macrophages. Cells were grown on with immobilized SVEP1 or BSA for 8 hr and then treated with 50 µg ml$^{-1}$ oxLDL in the culture media for 36 hr. Incorporated BrdU was measured by ELISA. Data were analyzed with One-way ANOVA test, and shown as the mean ± SEM. *NS*, not significant. $n$ = 8-12 (C-D). (E) Immunoblots of proximal integrin signaling kinases and downstream p38 from murine VSMCs adhered to control, or SVEP1, or SVEP1$^{CADrv}$-treated plates. β-actin was used as loading control. The bar graphs depict the mean ± SEM. ****$P < 0.0001$.

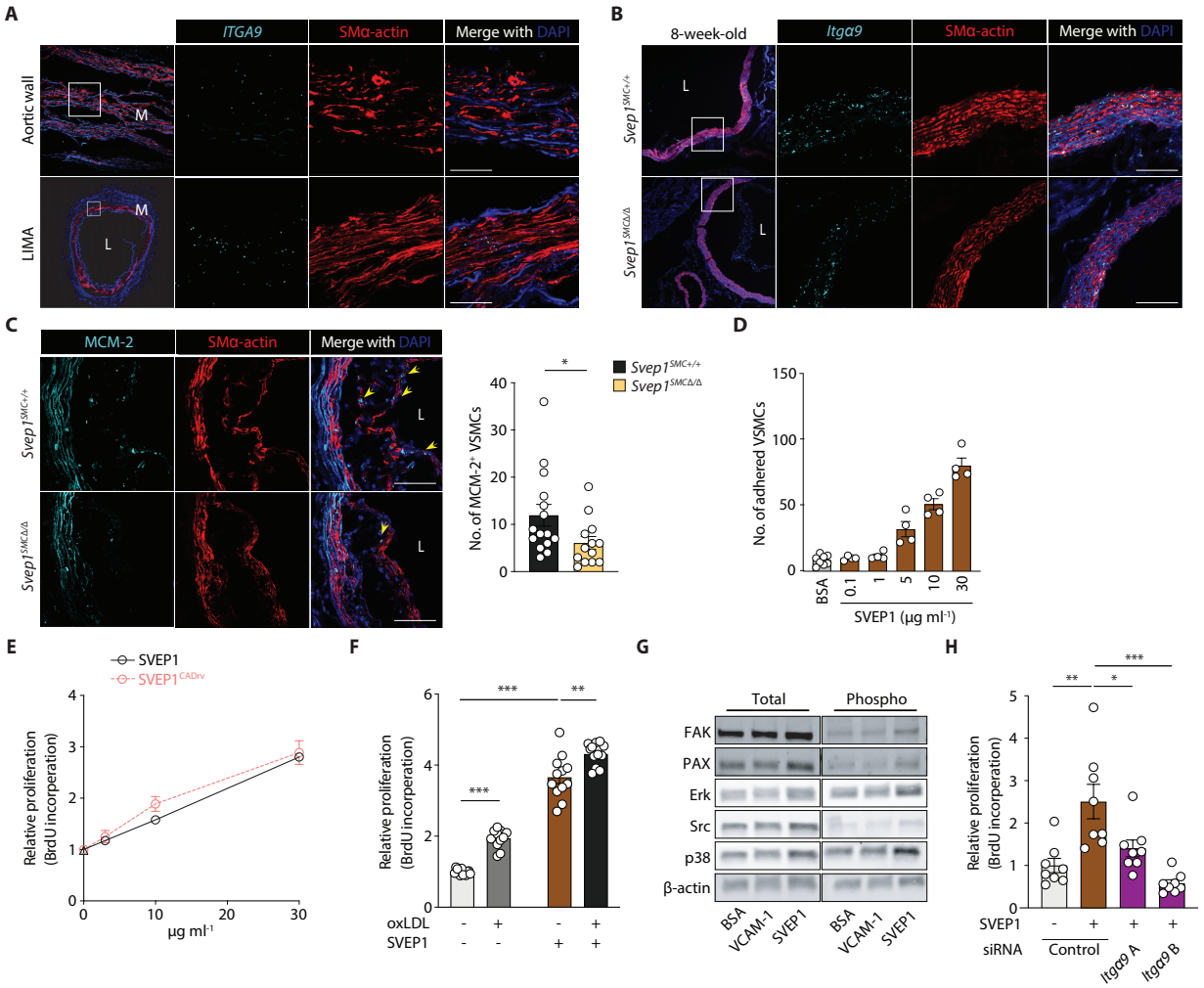


Figure 2.10 SVEP1 induces *Itgα9*-dependent proliferation in VSMCs. (A) *ITGA9* expression in human aortic wall and LIMA cross-sections from patients using ISH. M, media; L, lumen. (B) Expression of *Itgα9* in the aortic root from 8-week-old $Svep1^{SMC+/+}$ and $Svep1^{SMC\Delta/\Delta}$ mice using ISH. Outlined areas indicate the regions magnified in the next panels. Scale bar, 50 µm. (C) MCM-2 immunofluorescent staining of aortic root regions from $Svep1^{SMC+/+}$ and $Svep1^{SMC\Delta/\Delta}$ mice after 8 weeks of HFD feeding. Yellow arrows indicate MCM-

$2^+$/SMα-actin$^+$ cells within plaque. Quantification of MCM-$2^+$/SMα-actin$^+$ cells ($n$ = 13-15/group). Scale bars = 50 μm. Tissues in (A-C) were co-stained with the VSMC marker, SMα-actin. (D) Adhesion of murine VSMCs to increasing concentrations of immobilized SVEP1. Adhered cells were counted manually and normalized to wells lacking SVEP1. (E) Proliferation of murine VSMCs in response to increasing concentrations of immobilized SVEP1 and SVEP1$^{CADrv}$ using a BrdU incorporation assay. (F) *Svep1*$^{SMC\Delta/\Delta}$ murine VSMCs were incubated in wells precoated with 30 μg ml$^{-1}$ SVEP1 protein or BSA (as vehicle control) and treated with or without 50 μg ml$^{-1}$ oxLDL in the culture media for 36 hr. Proliferation was determined by BrdU incorporation. (G) Immunoblots of integrin signaling kinases and downstream kinases of murine VSMCs adhered to control, VCAM-1, or SVEP1-treated plates. β-actin was used as loading control. (H) Murine VSMCs were transfected with control or *Itga9*-targetted siRNAs and grown on immobilized SVEP1 or BSA. Proliferation was determined by BrdU incorporation. $n$ = 4-12/group; $N$ = 2-3 for D-H. Data were analyzed using an unpaired nonparametric Mann-Whitney test (C) or a two-tailed t-test (F and H). The bar graphs depict the mean ± SEM. *$P < 0.05$; **$P < 0.01$; ***$P < 0.001$.

### 2.3.5 SVEP1 and SVEP1$^{CADrv}$ regulate key VSMC differentiation pathways

We sought to characterize the response of primary VSMCs to the wildtype SVEP1 and SVEP1$^{CADrv}$ proteins using an unbiased methodology. Cells were collected after 20 hours of growth on the indicated substrate and transcriptomic analysis was performed using RNA-sequencing. Pathway and gene ontology analysis was used to determine the shared and unique transcriptional response to the SVEP1 variants. Consistent with previous findings, cell adhesion and proliferation-related pathways and terms were enriched in the shared transcripts of cells exposed to either SVEP1 variant. These include ECM-receptor interaction, focal adhesion, integrin-mediated signaling, positive regulation of cell proliferation, and proliferative and mitogenic pathways (Figure 2.11A, B). A striking number of differentiation and development-related pathways and terms were also enriched in cells exposed to the SVEP1 variants. These include angiogenesis, cell differentiation, and wound healing, among others (Figure 2.11A, B).

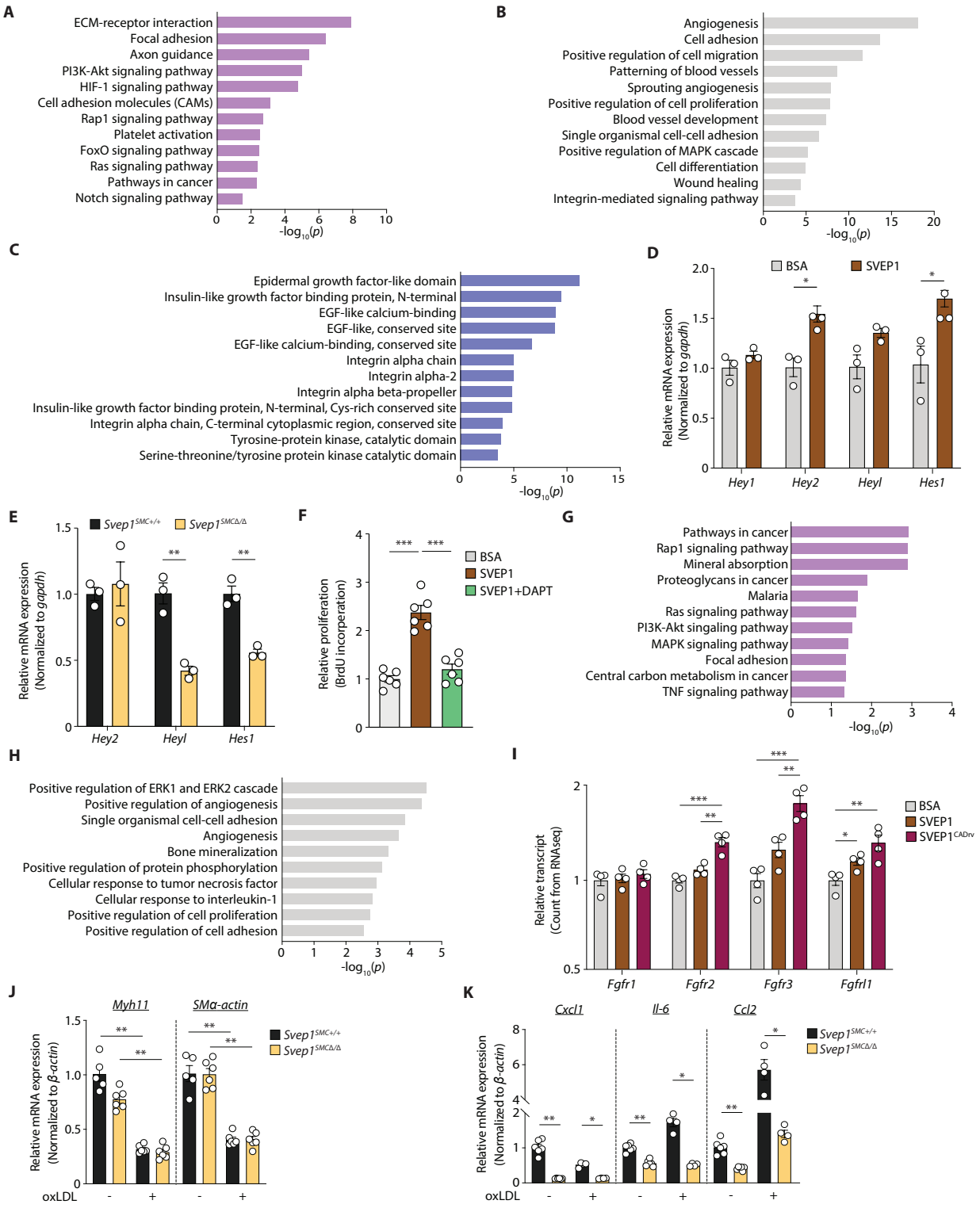


Figure 2.11 SVEP1 modulates key VSMC-developmental pathways.
(A-C) Common transcriptional response of murine VSMCs to SVEP1 and SVEP1$^{CADrv}$ proteins. Dysregulated (A) Kyoto Encyclopedia of Genes and Genomes (KEGG) pathways, (B) Gene Ontoloty (GO) term molecular functions, and (C) InterPro domains. Top 5 dysregulated categories plus additional, select categories are included. Bars represent -log$_{10}$ of *P* values (*n* =

4/group). (D) Transcription of canonical Notch target genes in murine VSMCs after 4 hours of adhesion to SVEP1, relative to BSA. (E) Basal transcription of Notch target genes in *Svep1*$^{SMC+/+}$ and *Svep1*$^{SMC\Delta/\Delta}$ murine VSMCs. (F) Proliferation of murine VSMCs in response to immobilized SVEP1. Cells were treated with DMSO (carrier) or 25 μM DAPT. Proliferation was determined by BrdU incorporation. $n$ = 3-6/group; $N$ = 2-3 for D-F. (G-H) Differential transcriptional response of murine VSMCs to SVEP1 and SVEP1$^{CADrv}$ proteins. Dysregulated (G) KEGG pathways, and (H) GO term molecular functions. Top 5 dysregulated categories plus additional, select categories are included. Bars represent -$\log_{10}$ of $P$ values. (I) Bar graph of *Fgfr* transcript counts from murine VSMC RNAseq. Each transcript is normalized to the BSA control group. $n$ = 4/group for G-I. (J, K) qPCR of (J) VSMC markers, and (K) inflammatory markers of murine VSMC cultured with or without 50 μg ml$^{-1}$ oxLDL for 24 hr ($n$ = 4-6/group; $N$ = 2). Data were analyzed using a two-tailed t-test (D-F and I-K). The bar graphs depict the mean ± SEM. *$P$ < 0.05; **$P$ < 0.01; ***$P$ < 0.001.

SVEP1 contains different and repeating domains that are known to play critical developmental roles and may therefore be governing the effects of SVEP1 on VSMCs. Further, although *Svep1*$^{-/-}$ and *Itgα9*$^{-/-}$ mice have similar phenotypes of edema and lymphatic defects (26, 79), the phenotype of *Svep1*$^{-/-}$ mice is markedly more severe [death by embryonic day 18.5 vs postnatal day 12 (47)], suggesting that ITGA9 may have partial redundancy with an additional receptor(s) for SVEP1. To search for evidence of additional domain interactions, we cross-referenced the transcriptional profile of VSMCs to the SVEP1 variants with InterPro (98), a database of protein domains. In addition to integrin-related domains, transcripts that code for EGF-like domain-containing proteins were highly differentially expressed in cells exposed to SVEP1 (Figure 2.11C). Repeat EGF-like domains often interact, as occurs in Notch signaling, suggesting SVEP1's repeat EGF-like domains may be playing an important, but as of yet undescribed role in the biological function of SVEP1 (98). Indeed, transcripts related to Notch signaling were dysregulated in cells exposed to SVEP1 (Figure 2.11A).

As an orthogonal approach to interrogating SVEP1's mechanisms and potential binding partners, we sought to identify homologues in distantly related species. The Drosophila protein, uninflatable, is a potential orthologue of SVEP1 (99) and contains a region defined by three

ephrin-receptor like domains, followed by tandem EGF-repeats and a Laminin-G domain (100), mirroring a region of SVEP1 that contains a highly similar sequence of domains. Inhibition of uninflatable in Drosophila larvae results in defective tracheal development, analogous to the vascular defects observed in zebrafish Svep1 mutants (101, 102). Uninflatable has been shown to bind and modulate Notch signaling in Drosophila (101, 103, 104). These findings, in addition to the RNAseq analysis, led us to hypothesize that SVEP1 may also modulate Notch signaling. VSMCs express multiple Notch receptors (105), thus, we tested the impact of SVEP1 on Notch signaling in VSMCs. This was assessed by seeding VSMCs on tissue culture plates treated with SVEP1 or BSA (as an inert control protein) for 4 hours, since Notch signaling is highly temporally regulated (106). Cells grown on SVEP1 had increased expression of canonical Notch targets *Hey2* and *Hes1* even without overexpression of a Notch receptor (Figure 2.11D). Conversely, primary VSMCs collected from *Svep1*$^{SMC\Delta/\Delta}$ mice had decreased transcription of Notch target genes (Figure 2.11E), supporting the regulation of Notch signaling by SVEP1. SVEP1-induced proliferation was also completely abrogated upon Notch inhibition by the γ-secretase inhibitor DAPT (Figure 2.11F). It is possible that Notch and integrin receptors may cooperatively regulate the effects of SVEP1, similar to that reported on non-canonical ECM Notch regulators Microfibrillar-associated protein 5 (MFAP5) and Epidermal growth factor-like protein 7 (EGFL7) (107).

Our experimental atherosclerosis models and Mendelian randomization analysis indicate that both SVEP1 variants are atherogenic, with SVEP1$^{CADrv}$ having the greater atherogenicity of the two. We therefore investigated the differential transcriptional responses of VSMCs to the SVEP1 variants. This analysis revealed that many proliferation-related pathways were disproportionately regulated by the variants (Figure 2.11G, H). Further exploration identified differential expression

of the fibroblast growth factor (FGF) receptor family between the variants. The FGFR family is also sub-categorized within several of the most differentially regulated pathways and terms. FGF signaling is proatherogenic in VSMCs (108), so we assessed the effect of each variant on the direction and magnitude of transcription of each FGF receptor expressed by VSMCs. Consistent with their relative atherogenicities, SVEP1 increased expression of FGF receptors but exposure to SVEP1$^{CADrv}$ resulted in higher expression of FGF receptors (Figure 2.11I). These data suggest that increased FGF signaling may contribute to the increased CAD risk associated with SVEP1$^{CADrv}$.

Given the fundamental role of integrin, Notch, and FGFR signaling in regulating VSMC phenotype, we assessed the effects of SVEP1 in response to oxLDL, an inflammatory stimulus relevant to atherosclerosis. Upon oxLDL stimulation, both *Svep1*$^{SMC+/+}$ and *Svep1*$^{SMC\Delta/\Delta}$ VSMCs decreased the expression of contractile markers *Myh11* and *SMα-actin* (Figure 2.11J), and increased expression of the inflammatory marker C-C motif chemokine ligand 2 (*Ccl2*) (Figure 2.11K), confirming an inflammatory response to oxLDL. C-X-C motif chemokine ligand 1 (*Cxcl1*), interleukin-6 (*Il-6*), and *Ccl2* expression was lower in *Svep1*$^{SMC\Delta/\Delta}$ VSMCs than *Svep1*$^{SMC+/+}$ controls, suggesting that SVEP1 may be a pro-inflammatory stimulus in VSMCs under atherosclerotic conditions.

### 2.3.6 SVEP1 promotes inflammation in atherosclerosis

To investigate how the loss of *Svep1* influences pathways involved in the development of atherosclerosis at the tissue level, we performed RNA-seq analyses on mRNA extracted from aortic arches of *Svep1*$^{SMC+/+}$and *Svep1*$^{SMC\Delta/\Delta}$ mice after 8 weeks of HFD. Loss of *Svep1* in VSMCs altered inflammatory pathways upon induction of atherosclerosis, including cytokine-cytokine receptor interaction, chemokine signaling, and NF-kappa B signaling pathways (Figure

2.12A). Both cell adhesion molecules (CAMs) and ECM-receptor interaction were also dysregulated in the atherosclerotic aortic arches from *Svep1*$^{SMC\Delta/\Delta}$ (Figure 2.12A, B). Quantitative PCR using cDNA from the aortic arches of the same mice was used to validate the RNA-seq results. Specifically, *Ccl2, Spp1* (secreted phosphoprotein 1, also known as osteopontin), and *Cxcl5* (C-X-C motif chemokine ligand 5) were decreased in *Svep1*$^{SMC\Delta/\Delta}$ mice, as compared to *Svep1*$^{SMC+/+}$ mice (Figure 2.13A). Despite these differences, we did not find a significant alteration in circulating inflammatory mediators in these mice, suggesting SVEP1 influences local tissue inflammation but not systemic inflammation (Figure 2.13B). These data are also consistent with our observations that *Svep1* depletion decreases neointimal macrophage staining in atherosclerotic plaque.

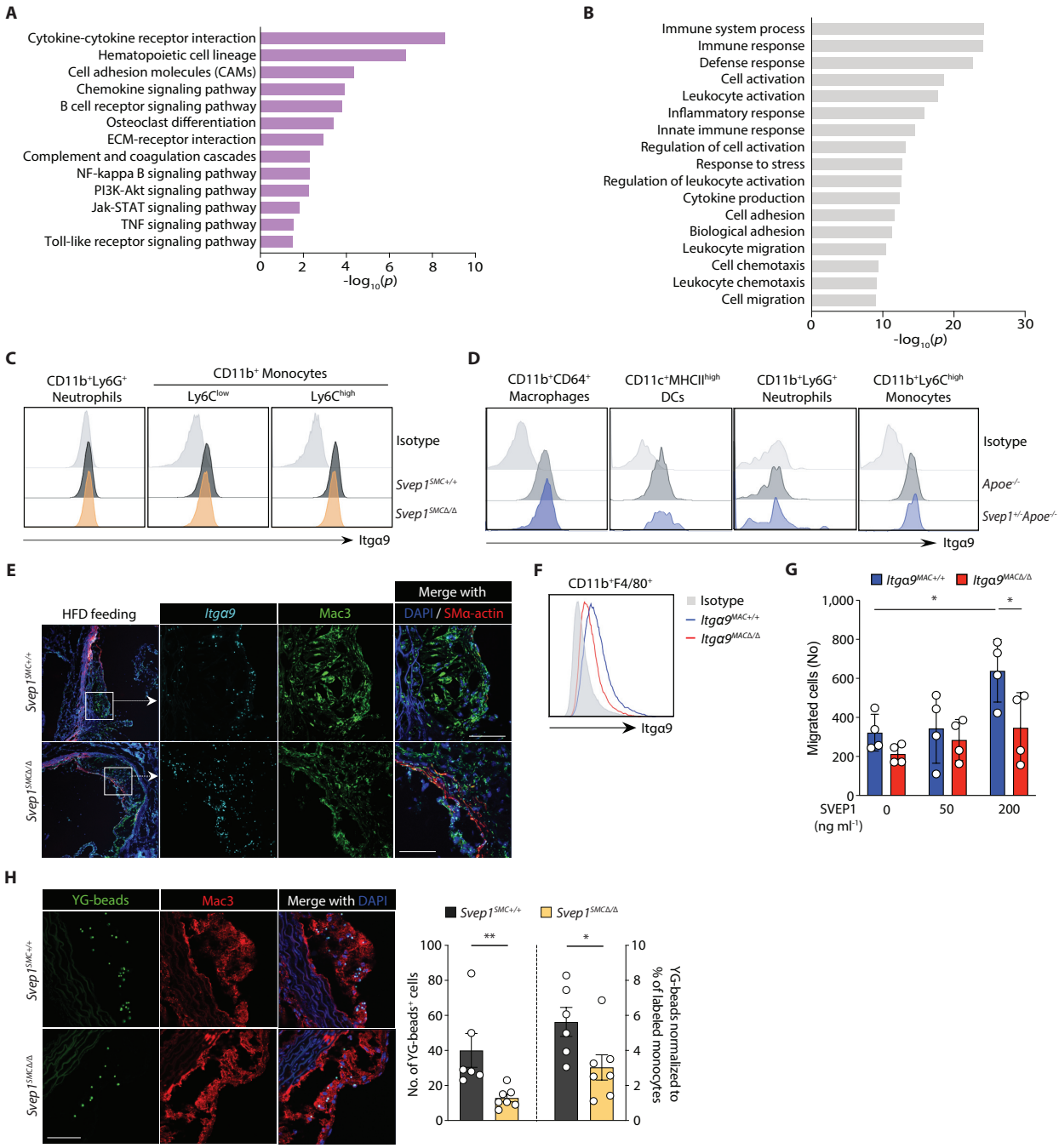


Figure 2.12 SVEP1 promotes inflammation in atherosclerosis.

(A-B) Differential transcriptional profile of atherosclerotic aortic arches from *Svep1*$^{SMC+/+}$ and *Svep1*$^{SMC\Delta/\Delta}$ mice. Dysregulated (A) KEGG pathways, and (B) GO term molecular functions. Top 5 dysregulated categories plus additional, select categories are included. Bars represent -log$_{10}$ of *P* values ($n$ = 3-4/group). (C) Histogram for *Itgα9β1* expression in mouse blood neutrophils (CD11b$^{+}$Ly6G$^{+}$), Ly6C$^{low}$ (CD11b$^{+}$Ly6C$^{low}$), and Ly6C$^{high}$ (CD11b$^{+}$Ly6C$^{high}$) monocytes from *Svep1*$^{SMC+/+}$ and *Svep1*$^{SMC\Delta/\Delta}$ mice after 8 weeks of HFD. (D) Histogram of *Itgα9β1* expression in the subpopulations of aortic leukocytes. Macrophages (CD64$^{+}$CD11b$^{+}$), DCs (CD11c$^{+}$MHCII$^{high}$), neutrophils (CD11b$^{+}$Ly6G$^{+}$), and Ly6C$^{high}$ (CD11b$^{+}$Ly6C$^{high}$) monocytes from *Apoe*$^{-/-}$ and *Svep1*$^{+/-}$*Apoe*$^{-/-}$ mice after 8 weeks of HFD ($n$ = 3-4/group; $N$ = 3). (E)

Expression of *Itgα9* in the aortic roots from *Svep1*$^{SMC+/+}$ and *Svep1*$^{SMCΔ/Δ}$ mice using ISH after 8 weeks of HFD. Tissues were co-stained for Mac3 and SMα-actin. Scale bars, 50 μm. (F) Expression of Integrin alpha-9 in BMDM from *Itgα9*$^{MAC+/+}$ and *Itgα9*$^{MACΔ/Δ}$ mice ($n$ = 3/group; $N$ = 3). (G) Migratory response of thioglycolate-elicited murine macrophages from *Itgα9*$^{MAC+/+}$ and *Itgα9*$^{MACΔ/Δ}$ were determined using a chemotaxis chamber incubated with 0, 50, and 200 ng ml$^{-1}$ of SVEP1 protein. Migrated cells were counted by an automated microscope and expressed as cells per field of view ($n$ = 4/group; $N$ = 2). (H) In vivo monocyte recruitment assay. YG-bead uptake within plaque lesion in the aortic root regions from *Svep1*$^{SMC+/+}$ and *Svep1*$^{SMCΔ/Δ}$ mice. Quantification of YG-bead uptake showing the total number of YG-beads per section (left Y axis), and the number of YG-beads normalized to the percentage of labeled Ly6C$^{low}$ monocytes (right Y axis) ($n$ = 6-7/group). Scale bar, 50 μm. Data were analyzed using two-tailed t-test (G) or unpaired nonparametric Mann-Whitney test (H). The bar graphs depict the mean ± SEM. *$P$ < 0.05; **$P$ < 0.01.

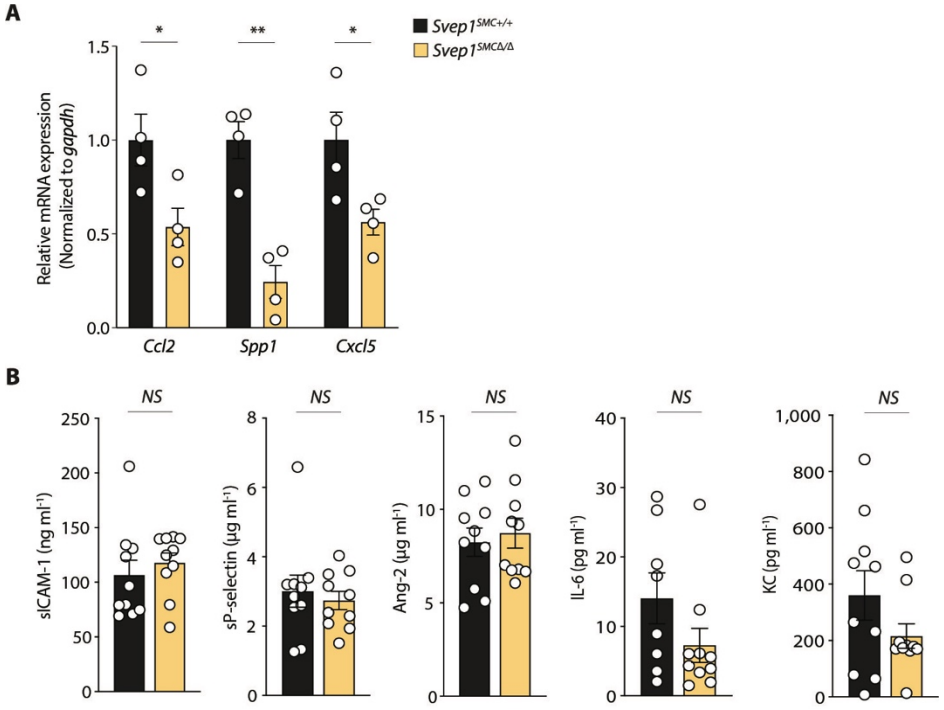


Figure 2.13 SVEP1 promotes local inflammation in atherosclerosis.
(A) qPCR validation of *Ccl2*, *Spp1*, and *Cxcl5* expression differences in aortic arches of mice. Each gene was normalized to *gapdh. (n* = 4/group) *(*B) Analysis of cytokine and chemokine biomarkers from 8 weeks HFD-fed *Svep1*$^{SMC+/+}$ and *Svep1*$^{SMCΔ/Δ}$ mice. sICAM-1, soluble intercellular adhesion molecule-1; sP-selectin, soluble P-selectin; Ang-2, angiotensin-2; IL-6, interleukin-6; KC, C-X-C motif ligand1 (CXCL1). $n$ = 8-10/group. A two-tailed t-test was used to calculate statistical significance The bar graphs depict the mean ± SEM. *$P$ < 0.05; **$P$ < 0.01; *NS*, not significant.

Integrins play a critical role in the immune response, we therefore asked whether immune cells may also express integrin α9β1 and interact with SVEP1 in atherosclerosis. In human peripheral

blood cells, moderate integrin α9β1 expression was detected by neutrophils and low expression was detected by $CD14^{low}CD16^{+}$ non-classical, $CD14^{high}CD16^{+}$ intermediate, and $CD14^{+}CD16^{-}$ classical monocytes (Figure 2.14A) as previously reported (109). Given that monocytes alter their expression profiles upon tissue entry and differentiation into macrophages (110), we sought to test if macrophages in atherosclerotic plaque express *ITGA9*. Indeed, *ITGA9* expression was detected in $CD68^{+}$ macrophages within human atherosclerotic plaque by in situ hybridization (Figure 2.14B).

We then sought to further assess the expression of integrin α9β1 expression in circulating murine leukocyte subsets. High expression of integrin α9β1 was detected in both $Ly6C^{hi}$ and $Ly6C^{low}$ monocytes and we could detect low expression in neutrophils (Figure 2.12C). These expression patterns were unaltered in heterozygous *Svep1* deficiency (Figure 2.14C) and we did not observe an induction of integrin α9β1 expression upon oxLDL treatment in any cell type tested (Figure 2.14D, E). Considering that integrin α9β1 is expressed by monocyte subsets in peripheral mouse blood, we further analyzed its expression in myeloid cells from the aortas of $Apoe^{-/-}$ and $Svep1^{+/-}$ $Apoe^{-/-}$ mice following 8 weeks of HFD feeding. We discovered that integrin α9β1 was expressed in both macrophages and $Ly6C^{hi}$ monocytes of these mice (Figure 2.12D), consistent with human expression data. We similarly detected robust expression of *Itgα9* by neointimal macrophages using in situ hybridization (Figure 2.12E).

Since integrin α9β1 is expressed on monocytes/macrophages, we sought to better understand whether SVEP1 could be directly interacting with integrin α9β1 on these cells. To test this, we generated mice with myeloid cell lineage-specific knockout of *Itgα9* using *LysM-Cre* (*Itgα9*$^{flox/flox}$*LysM-Cre*, hereafter referred to as *Itga9*$^{MAC\Delta/\Delta}$). *Itga9*$^{+/+}$*LysM-Cre* mice (referred to as *Itga9*$^{MAC+/+}$) served as controls. First, we confirmed that bone marrow-derived macrophages

from *Itga9*$^{MAC\Delta/\Delta}$ animals had a reduction in the amount of integrin α9β1 that was present on the cell surface (Figure 2.12F). We then tested the ability of peritoneal macrophages from these animals to migrate in response to SVEP1 using a trans-well migration assay. SVEP1 exposure induced a dose-dependent trans-well migration of macrophages from *Itga9*$^{MAC+/+}$ control animals but not from *Itga9*$^{MAC\Delta/\Delta}$ mice (Figure 2.12G). This suggests that SVEP1 and integrin α9β1 may directly interact to augment myeloid cell homing or migration. Consistent with this, THP-1 cells, a human monocytic cell line, adhered to SVEP1 in a dose-dependent manner (Figure 2.14F). Integrin signaling was also activated in THP-1 cells upon exposure to SVEP1 or SVEP1$^{CADrv}$ and no differences were observed between the variants (Figure 2.14G).

To test if SVEP1 had similar effects on leukocytes in vivo, we performed an in vivo monocyte recruitment assay in *Svep1*$^{SMC+/+}$ and *Svep1*$^{SMC\Delta/\Delta}$ mice. After 8 weeks of HFD feeding, we injected yellow-green (YG) latex beads intravenously to label circulating Ly6C$^{low}$ monocytes. Flow cytometry was performed three days after intravenous bead injection (to confirm labeling) and the aortic tissues were isolated for histology on the fourth day following bead injection (to assess recruitment). We confirmed that YG beads were preferentially labeled on Ly6C$^{low}$ monocytes and not on Ly6C$^{high}$ monocytes, indicating efficient bead labeling of circulating monocytes (Figure 2.14H). We did not observe a difference between groups in the efficiency of bead labeling for monocyte subsets (Figure 2.14I). Next, we quantified the number of labeled monocytes recruited into atherosclerotic plaques of aortic roots using fluorescent microscopy. *Svep1*$^{SMC\Delta/\Delta}$ mice had fewer YG beads per atheroma, with or without normalization to the percentage of labeled monocytes, relative to *Svep1*$^{SMC+/+}$ mice (Figure 2.12H). Taken together, these data support SVEP1's role in promoting inflammation in atherosclerosis, either indirectly

by promoting an inflammatory VSMC phenotype, directly by interacting with integrin α9β1 on circulating or tissue leukocytes, or a combination of these processes.

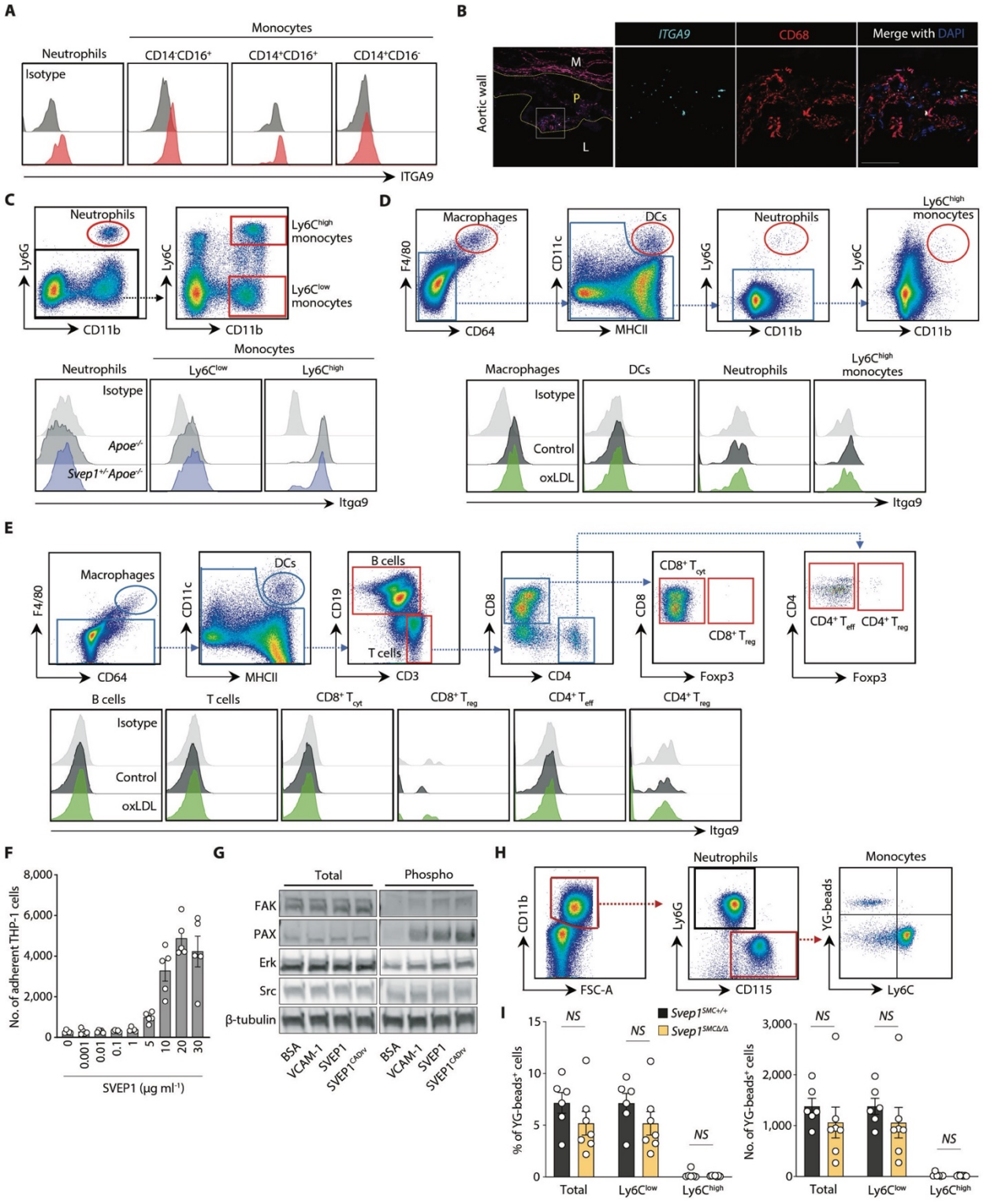


Figure 2.14 SVEP1 promotes local inflammation in atherosclerosis, continued.

(A) ITGA9 expression in neutrophils and monocyte subsets ($CD14^{low}CD16^{+}$ non-classical, $CD14^{high}CD16^{+}$ intermediate, and $CD14^{+}CD16^{-}$ classical monocytes) in human blood ($n$ = 3). (B) *ITGA9* expression in human aortic wall and LIMA cross-sections from patients using ISH. Tissues were co-stained for CD68. Atherosclerotic neointima is outlined in yellow. The portion of the image magnified in the right-most panels is outlined in white. M, media; P, plaque; L, lumen. (C) Gating strategy and histogram for Itgα9β1 expression in mouse blood neutrophils ($CD11b^{+}Ly6G^{+}$), $Ly6C^{low}$ ($CD11b^{+}Ly6C^{low}$), and $Ly6C^{high}$ ($CD11b^{+}Ly6C^{high}$) monocytes ($n$ = 3-4/group). (D) Gating strategy and histogram of Itgα9β1 expression in the subpopulations. Splenocytes isolated from *Apoe*$^{-/-}$ mice were incubated with 400 U $ml^{-1}$ collagenase D for 30 min at 37°C followed by incubation with 25 μg $ml^{-1}$ oxLDL or vehicle control (PBS) for 48 hr. Gating strategy for detection of macrophages, DCs, neutrophils, and $Ly6C^{high}$ monocytes. Briefly, $CD45^{+}$ cells were detected after removal of auto-fluorescence with unused fluorescence, for further analysis of $CD64^{+}F4/80^{+}$ macrophages. Among $CD64^{-}F4/80^{-}$ cells, $MHCII^{high}CD11c^{+}$ DCs were detected following detection of $CD11b^{+}Ly6G^{+}$ neutrophils and $CD11b^{+}Ly6C^{high}$ monocytes from $CD11b^{+}$ cells with Ly6G and Ly6C expression. Macrophages ($CD64^{+}CD11b^{+}$), DCs ($MHCII^{high}CD11c^{+}$), neutrophils ($CD11b^{+}Ly6G^{+}$), and $Ly6C^{high}$ ($CD11b^{+}Ly6C^{high}$) monocytes from mice group. (E) Gating strategy for detection of B lymphocytes and T lymphocytes including cytotoxic $CD8^{+}$ ($CD8^{+}$ $T_{cyt}$), regulatory $CD8^{+}$ ($CD8^{+}$ $T_{reg}$), effector $CD4^{+}$ ($CD4^{+}$ $T_{eff}$), and regulatory $CD4^{+}$ T cells ($CD4^{+}$ $T_{reg}$). Histograms of Itgα9β1 expression in B and T lymphocytes from mice. $n$ = 3 (D-E). (F) Adhesion of THP-1 cells to increasing concentrations of SVEP1. Data are normalized to BSA control. Nonadherent cells were removed by centrifugation. $n$ = 5/concentration; $N$ = 3. (G) THP-1 cells were seeded on wells containing the indicated protein. Cells were lysed and protein lysates were subject to immunoblotting with the indicated antibody. BSA served as a negative control and VCAM-1 served as positive control. β-tubulin was used as loading control. $N$ = 3. (H) In vivo monocyte recruitment assay. YG-beads were administered to mice retro-orbitally after 8 weeks of HFD feeding. Labeling efficiency of $Ly6C^{low}$ monocytes was verified and then YG-beads in the aortic root plaque were subsequently analyzed. Gating strategy for detection of YG-bead labeling by $Ly6C^{low}$ monocytes. Among $CD11b^{+}$ cells, Ly6G positive neutrophils ($CD11b^{+}CD115^{-}Ly6G^{+}$) were gated out, following further analysis of $CD115^{+}$ cells (total monocytes) with Ly6C expression. YG-beads were only detected in $Ly6C^{low}$ not $Ly6C^{high}$ monocytes. (I) Labeling efficiency as the percentage and total number of YG-bead positive murine $CD115^{+}$, $Ly6C^{low}$, and $Ly6C^{high}$ monocytes. $n$ = 6-7/group. Data were analyzed with unpaired nonparametric Mann-Whitney test and shown as the mean ± SEM. *NS*, not significant.

## 2.4 Discussion

Human genomic studies hold great promise in identifying therapeutic targets for disease (111), but a substantial limitation in translating their findings is the identification of specific causal genes that underlie the observed statistical associations. In a previous study, we identified a low-frequency polymorphism in *SVEP1* that robustly associated with coronary artery disease risk in

humans (6), but it was not clear if *SVEP1* was the causal gene in the locus. Here, we present evidence that SVEP1 is causal in coronary artery disease using experimental mouse models and Mendelian randomization.

Atherosclerosis is a complex, multifactorial disease process with numerous cell types playing a role in its pathogenesis. This presents an arduous challenge when validating genomic risk loci and testing their mechanisms. The SVEP1$^{CADrv}$ does not associate with changes in plasma lipid concentrations (6), prompting us to explore how SVEP1 might influence other aspects of disease pathogenesis. We used human and mouse expression data at the cell and tissue level to develop mechanistic hypotheses, which we then tested using in vivo and in vitro approaches. Specifically, high basal arterial expression of both *SVEP1* and *ITGA9*, and increased *SVEP1* expression under pathological conditions, led us to hypothesize that these proteins may influence local disease processes. Upon exposure to various pathologic stimuli, VSMCs can undergo a "phenotype shift", in which they lose their quiescent, contractile properties and become migratory, proliferative, inflammatory, and synthetic (84, 112). VSMCs gain properties of matrix-synthesizing fibroblasts during atherosclerosis (113), making VSMCs our primary candidates for the source of SVEP1 within atherosclerotic plaque. In fact, consistent with prior reports which concluded that SVEP1 is not produced by endothelial or immune cells (26) ,we observed negligible *Svep1* expression in the plaques of *Svep1*$^{SMC\Delta/\Delta}$ animals. Thus, our results provide strong evidence that atherogenic SVEP1 is indeed synthesized by VSMC-derived cells within the atherosclerotic plaque.

Using two independent mouse models in which *Svep1* was depleted either partially in all cells (*Svep1*$^{SMC+/-}$) or fully in only VSMCs (*Svep1*$^{SMC\Delta/\Delta}$), we demonstrated that depleting SVEP1 resulted in a significant reduction in the development of atherosclerotic plaque with a magnitude

of effect similar to murine models of other CAD risk loci (113, 114). We then used expression of *ITGA9* to identify disease-relevant cell types that may respond to SVEP1. This led to the hypothesis that SVEP1 may be interacting with VSMCs by an autocrine mechanism or monocytes by a paracrine mechanism to promote atherosclerosis. VSMCs play a particularly complex and intriguing role in atherosclerosis and warrant further discussion. Recent lineage tracing studies have challenged the notion that VSMCs play a protective role in atherosclerosis (84) by demonstrating that a large, heterogenous population of cells within plaque are derived from VSMCs (84, 112, 115). Furthermore, numerous CAD risk loci have now been linked to VSMCs (116). This study demonstrates that SVEP1 influences the behavior of VSMCs by regulating pathways with vital roles in VSMC biology. These pathways include integrin, Notch, and FGFR signaling, each of which has been shown to contribute to atherosclerosis (89, 108, 117, 118). Recent studies have provided novel insights into the regulation of VSMC phenotype in atherosclerosis by various transcription factors (113, 115, 119). The ECM also plays a fundamental role in regulating VSMC phenotype and is amenable to pharmacologic intervention. Current strategies for the treatment and prevention of CAD consist of lowering risk factors, such as plasma lipids, yet substantial residual risk remains despite effective treatment. Intervening on VSMCs may be a powerful complimentary approach to these traditional therapies.

In addition to its association with CAD, our Mendelian randomization results suggest that circulating SVEP1 causally underlies risk of hypertension and type 2 diabetes. Although the source of SVEP1 in human plasma is unknown, other ECM proteins have been detected in the circulation of patients with atherosclerosis, suggesting that plasma concentrations of these proteins may reflect tissue concentrations and atherosclerotic remodeling (120, 121). The mechanisms by which the genetic variants used in the Mendelian randomization affect plasma

SVEP1 are unclear. Two reasonable hypotheses include modification of protein secretion or degradation. Alternatively, it is possible that protein-modifying polymorphisms could alter the affinity of aptamer binding (and thus impact the estimated plasma protein concentrations). It is unlikely that altered aptamer binding is a major contributor, however, because differential plasma SVEP1 concentrations were observed using two independent aptamers and because the majority of genetic variants linked to altered plasma concentrations were not located in protein-coding DNA segments. Further studies will be required to determine the precise mechanisms by which these variants affect plasma protein concentrations. Regardless, the power of the two sample Mendelian randomization framework is that these alleles are allocated randomly at birth and are associated with plasma SVEP1 concentrations in the absence of disease, suggesting that the presence of disease is not driving altered SVEP1 concentrations, but rather that altered SVEP1 expression is causally related to disease. This further suggests that circulating SVEP1 may be useful as a predictive biomarker.

Additional human genetic data support a broader role of SVEP1 in cardiometabolic disease. The alpha subunit of integrin α9β1, which binds to SVEP1 (76) with an affinity that far exceeds its other known ligands (122-125), is also associated with blood pressure in multiple studies (77, 78). Overexpression of disintegrin and metalloproteinase with thrombospondin motifs-7 (ADAMTS-7), another CAD risk locus, in primary rat VSMCs alters the molecular mass of SVEP1 (126). The overlapping disease associations and molecular interactions between these three risk loci converge on SVEP1 and point to a regulatory circuit with a prominent, yet unexplored role in cardiometabolic disease. Further studies will be required to validate their interactions and mechanisms in vivo, and to explore the potential of targeting this pathway for the treatment of cardiometabolic disease.

Our in vivo data were limited to the *Apoe*$^{-/-}$ mouse model and our functional studies were limited to VSMCs and myeloid cells. Additional confirmatory studies in other model systems and cell types are needed to further evaluate the therapeutic potential of targeting SVEP1. In addition, as SVEP1 is critical for development, we chose to deplete SVEP1 in our VSMC-specific model starting at 6 weeks of age and we do not know how long the protein is retained in the ECM. Finally, although VSMC-specific depletion of SVEP1 did not result in any obvious deleterious impact, we did not rigorously evaluate those animals for more subtle adverse effects.

Our complementary mouse models demonstrate that *Svep1* haploinsufficiency and VSMC-specific *Svep1* deficiency significantly abrogate the development of atherosclerosis. Each intervention appeared to be well tolerated by mice, as we did not observe any adverse response to SVEP1 depletion. Similarly, our Mendelian randomization analyses suggest there may be a therapeutic window to safely target SVEP1. These findings suggest that targeting SVEP1 or selectively modulating its interactions may be a viable strategy for the treatment and prevention of coronary artery disease.

## 2.5 Materials and Methods

### 2.5.1 Study design

We designed this study to experimentally determine if SVEP1 causally contributes to risk for atherosclerosis. We used primary tissues harvested from humans and mice to determine if SVEP1 was produced in tissues and cell types of relevance to atherosclerosis. We utilized Mendelian randomization to determine if SVEP1 is causally related to cardiovascular disease in humans. To study the mechanism by which SVEP1 may promote atherosclerosis, we performed animal studies in HFD fed *Apoe*$^{-/-}$ mice. The number of animals used in each study group are specified in the figure legends. The in vitro experimental data included in this manuscript are representative of multiple experimental outcomes. Experiments were not performed in a blinded fashion. All animal studies were performed according to procedures and protocols approved by the Animal Studies and Institutional Animal Care and Use Committees of the Washington University School of Medicine. All human research participants provided written informed consent for the studies described below which were conducted according to procedures and protocols approved by the Human Research Protection Office and Institutional Review Board of the Washington University School of Medicine.

### 2.5.2 Mice

*Svep1*$^{+/-}$ mice were made by KOMP (knockout mouse project), and these mice were then crossed with mice expressing the flippase FLP recombinase under the control of the promoter of the human actin beta gene (hATCB) to generate *Svep1*$^{flox/flox}$ (*Svep1*$^{\Delta/\Delta}$) mice. CRISPR/Cas9 genome editing technology was used in collaboration with the Washington University School of Medicine Genome Engineering and Transgenic Micro-Injection Cores to generate *Svep1*$^{G/G}$ mice

on a C57BL/6 background harboring the *SVEP1* mutation at the homologous murine position (p.D2699G). *Svep1*$^{+/-}$ and *Svep1*$^{G/G}$ mice were crossed with *Apoe*$^{-/-}$ mice (#002052, Jackson Laboratory) to get *Svep1*$^{+/-}$*Apoe*$^{-/-}$ and *Svep1*$^{G/+}$*Apoe*$^{-/-}$ mice, which we maintained as breeders to generate experimental and control mice. We crossed *Svep1*$^{\Delta/\Delta}$ mice with *Myh11-CreER*$^{T2}$ (#019079, Jackson Laboratory) mice to generate *Svep1*$^{\Delta/+}$*Myh11-CreER*$^{T2}$ mice. *Svep1*$^{\Delta/+}$*Myh11-CreER*$^{T2}$ males were then crossed with *Svep1*$^{\Delta/+}$ females to generate experimental *Svep1*$^{\Delta/\Delta}$*Myh11-CreER*$^{T2}$ and control *Svep1*$^{+/+}$*Myh11-CreER*$^{T2}$ male littermate mice. Finally, *Svep1*$^{\Delta/\Delta}$*Myh11-CreER*$^{T2}$ males were crossed with *Apoe*$^{-/-}$ females. We maintained *Svep1*$^{\Delta/+}$*Myh11-CreER*$^{T2}$*Apoe*$^{-/-}$ males and *Svep1*$^{\Delta/+}$*Apoe*$^{-/-}$ females as breeders to generate experimental *Svep1*$^{\Delta/\Delta}$*Myh11-CreER*$^{T2}$*Apoe*$^{-/-}$ (*Svep1*$^{SMC\Delta/\Delta}$) and control *Myh11-CreER*$^{T2}$*Apoe*$^{-/-}$ (*Svep1*$^{SMC+/+}$) mice. To activate Cre-recombinase, mice were injected intraperitoneally with 1 mg of tamoxifen (#T5648, Sigma-Aldrich) in 0.1 mL peanut oil (#P2144, Sigma-Aldrich) for 10 consecutive days starting at 6 weeks of age. Tamoxifen treatment was performed with all experimental and control mice in an identical manner. *Itgα9*$^{flox/flox}$ (*Itgα9*$^{\Delta/\Delta}$) mice were gifts from Drs. Dean Sheppard and Livingston Van De Water (Albany Medical College, New York), and *LysM-Cre* mice were provided from Dr. Babak Razani (Washington University School of Medicine, Saint Louis). We crossed *Itgα9*$^{fl/fl}$ mice with *LysM-Cre* mice, and maintained *Itgα9*$^{fl/+}$*LysM-Cre* mice as breeders to generate *Itgα9*$^{fl/fl}$*LysM-Cre* (*Itgα9*$^{MAC\Delta/\Delta}$) and control *Itgα9*$^{+/+}$*LysM-Cre* (*Itgα9*$^{MAC+/+}$) mice. All mice were housed in a pathogen-free environment at the Washington University School of Medicine animal facility and maintained on a 12 hr light/12 hr dark cycle with a room temperature of 22 ± 1°C.

### 2.5.3 Statistical analysis

For animal model data, a two-group independent t-test, one-way analysis of variance (ANOVA), or two-way ANOVA were used, provided the data satisfied the Shapiro-Wilk normality test. Otherwise, the Mann-Whitney U test, Kruskal-Wallis one-way ANOVA test, and Friedman two-way ANOVA test were used. Bonferroni correction was used for post-hoc multiple comparison in ANOVA. Unless otherwise stated, cellular assays were analyzed by an unpaired, two-tailed, heteroscedastic t-test. Statistical analyses were performed with GraphPad Prism. Individual data points are reported in data file S1.

### 2.5.4 Human tissue collection

Prior to coronary artery bypass grafting surgery (CABG) for the treatment of symptomatic coronary artery disease, we consented five patients for tissue and peripheral blood collection at the time of their planned CABG to be performed at Barnes Jewish Hospital. The surgical plan for all patients included using the left internal mammary artery (LIMA) as an arterial graft to the left anterior descending (LAD) coronary artery and at least one venous graft to a different coronary artery. During the CABG, we collected the distal end of the LIMA which was trimmed in order to accommodate the length needed to reach the LAD. We also collected the aortic wall punch biopsy that was used to provide a proximal anastomotic site for the venous conduit. Tissues were immediately placed in phosphate buffered saline (PBS) on ice and brought to the laboratory where they were frozen at -80°C prior to in situ hybridization described below. During the CABG, we also collected 5-7 ml of peripheral blood in a tube containing the anticoagulant $K_3$ ethylenediaminetetraacetic acid (EDTA) (#6457, BD Biosciences) which was used for flow cytometry as described below.

*Diet and assessment of atherosclerosis*

### 2.5.5 Diet and assessment of atherosclerosis

All experimental mice were fed a diet containing 21% fat by weight (42% kcal from fat) and 0.2% cholesterol (#TD.88137, Envigo Teklad) for 8 and 16 weeks starting at 8 weeks of age. After HFD feeding, blood was collected from the retro-orbital plexus after 12 hr of fasting. Mice were euthanized by carbon dioxide inhalation. Plasma samples were prepared from the collected blood by centrifugation at 13,000 rpm for 10 min at 4°C. Total cholesterol (#STA-384), triglycerides (#STA-397), and glucose (#STA-681) in mouse plasma were determined using the appropriate kit (all purchased from Cell Biolabs, Inc). Hearts and whole aortas (from the aortic arch to the iliac artery) were harvested after perfusion with PBS. For en face analysis, isolated aortas were cleaned by removing perivascular fat tissues, opened longitudinally, and pinned onto black wax plates. After fixation with 4% paraformaldehyde overnight at 4°C, aortas were washed with PBS for 1 hr, and stained with 0.5% Oil Red O in propylene glycol (#O1516, Sigma-Aldrich) for 3 hr at room temperature. After staining, aortas were de-stained with 85% propylene glycol in distilled water for 5 min to reduce background staining and washed with distilled water for 15 min. For analysis of plaque in the aortic root, hearts were fixed overnight with 4% paraformaldehyde at 4°C, washed with PBS for 1 hr, and embedded into optimal cutting temperature (OCT) compound (#4583, Sakura Finetek). 5-µm-thick cryosections were stained overnight with 0.5% Oil Red O in propylene glycol, de-stained with 85% propylene glycol in distilled water for 5 min, and washed with distilled water for 15 min. Measurement of plaque was performed using 6-8 sections per artery to get the average value of size. The atherosclerotic plaque area was digitized and calculated using AxioVison (Carl Zeiss).

### 2.5.6 Antibodies and reagents

To produce murine SVEP1 protein, total RNA was purified from lung tissue of 8 week-old-mice by RNeasy kit (Life Technology). SuperScript IV First-Strand Synthesis System (Life

Technology) with oligo $d(T)_{20}$ primer used to obtain full-length reverse transcripts. Following double stranded DNA synthesis by PCR using PrimeSTAR GXL DNA Polymerase (Takara Bio) using forward 5'-ATGTGGTCGCGCCTGGCCTTTTGTTG and reverse 5'-AAGCCCGGCTCTCCTTTTCCTGGAACAATCAT primers, the resulting amplicon was subcloned into pCMV6 plasmid (Origene Technology) in frame with Myc and Flag tag by In-Fusion HD EcoDry Cloning Plus System (Takara Bio). In order to insert a poly histidine tag for protein expression and purification, the Flag tag was replaced by a 10-histidine tag. Oligonucleotides 5'-CACCACCACCACCACCACCACCACCACTGAACGGCCGG and 5'-CCGTTCAGTGGTGGTGGTGGTGGTGGTGGTGGTG coding for poly-histidine, stop codon and FseI compatible sticky end were synthetized, annealed and ligated to the vector, which was digested by EcoRV and FseI downstream of the myc tag and the stop codon respectively. The sequence of the full Svep1-myc-$His_{10}$ construct was verified by Sanger sequencing. The protein was expressed in FreeStyle 293F cells (Invitrogen) grown in FreeStyle expression media. Transient transfection of the 3 $\mu g\ ml^{-1}$ of vector DNA plus 9 $\mu g\ ml^{-1}$ Polyethylenimine (PEI) (25 kDa linear PEI, Polysciences, Inc.) was used to express the protein in $2.5 \times 10^6$ cells $ml^{-1}$. After overnight incubation, the same volume of fresh media plus 1 mM (final concentration) valproic acid was added. The transfected cells were incubated in flasks in orbital shaker at 100 rpm in 37°C with 8% $CO_2$ incubator for 48 hr, the conditioned media was collected by centrifugation at 300 rpm for 15 min. Cells were resuspended in fresh expression media and incubated for 48 hr. The conditioned media was collected, and this procedure was repeated one more time. Cell viability at the end of the experiment was >70%. The protein was purified in an NGC chromatographic system (BioRad Lab) in two steps: i) conditioned media was added to 1/10 of its volume of 10X PBS, and the pH check and fixed to 7.1. The protein was

pulled down by a disposable column loaded with 5 ml Nuvia IMAC resin (BioRad Lab) at 1 ml $min^{-1}$, washed with 50 ml PBS and the protein eluted in PBS plus 250 mM Imidazole, and ii) the eluted protein solution was concentrated 10 times in a Vivaspin concentrator 30 kDa cut off and loaded in a Superose 6 increase 10/300 (GE Life Sciences) with PBS as a carrier buffer. The fractions were evaluated by western blot probed with Myc tag antibody, and the purity of the protein was evaluated in PAGE-SDS 4-15% stained with Coomassie brilliant blue. More of the 95% of the protein in the gel corresponded to a single band. Further analysis by Mass Spectroscopy confirmed that more than 95% of the peptides detected corresponded to SVEP1. For immunofluorescent staining, anti-β-galactosidase (#ab9361, abcam, 1:1000), anti-Mac3 (#550292, clone M3/84, BD Biosciences, 1:100), anti-SMα-actin-cy3 (#C6198, clone 1A4, Sigma-Aldrich, 1:1000), anti-MCM-2 (#4007, Cell Signaling, 1:100) were used, and then visualized with anti-chicken-Alexa488 (#A11039), anti-rat-Alexa488 (#A21470), anti-rat-Alexa594 (#A21471, all purchased from Invitrogen, 1:400), and ProLong Gold antifade reagent with DAPI (#P36935, Invitrogen) were used. In case of detection of MCM-2 staining, samples were visualized with anti-rabbit-HRP (#7074S, Cell Signaling, 1:1000) followed by TSA Plus Cyanine 5 (#NEL745E001KT, PerkinElmer). For immunohistochemistry studies, hematoxylin solution (#HHS80), eosin solution (#HT110180), Masson's trichrome staining kit (#HT15-1KT, all purchased from Sigma-Aldrich), and Permount solution (#SP15-500, Fisher Chemicals) were used. For flow cytometry, the following anti-mouse antibodies were used; anti-CD16/32 FcR blocker (#14-0161, eBioscience), PerCP-labeled anti-CD45 (#103129, clone 30-F11), BV510-labeled anti-CD11b (#101263, clone M1/70), BV421-labeled anti-CD64 (#139309, clone X54-5/7.1), PE/cy7-labeled anti-CD11c (#117317, clone N418), APC/cy7-labeled anti-MHCII (#107627, clone M5/114.15.2), FITC-labeled anti-F4/80 (#123108, clone BM8), BV605-labeled

anti-CD19 (#115540, clone 6D5), APC-labeled anti-CD115 (#135510, clone AFS98), Alexa700-labeled anti-Ly6C (#128023, clone HK1.4), PE/Cy7-labeled anti-Ly6G (#127618, clone 1A8, all purchased from Biolegend), PE/cy5.5-labeled anti-CD4 (#35-0042-82, clone RM4-5, eBioscience), Alexa700-labeled anti-CD8a (#56-0081-80, clone 53-6.7, eBioscience), and PE-labeled anti-Itgα9β1 (#FAB3827P, R&D systems). Following anti-human antibodies were used. FcR blocker (#564219, BD biosciences), PerCP/cy5.5-labeled anti-CD45 (#368504, clone 2D1), Alexa700-labeled anti-CD3 (#300323, clone HIT3a), anti-CD19 (#115527, clone 6D5), anti-CD56 (#392417, clone QA17A16), FITC-labeled anti-CD15 (#301904, clone HI98), BV421-labeled CD66b (#305111, clone G10F5), APC/cy7-labeled anti-CD14 (#325619, clone HCD14), BV605-labeled anti-CD16 (#360727, clone B73.1), and PE-labeled anti-ITGα9β1 (#351606, clone Y9A2, all purchased from Biolegend). RBC lysis buffer (#423101, Biolegend), FoxP3 transcription factor staining buffer set (#00-5523, eBioscience), Leuko spin medium (#60-00091, Pluriselect) were used in flow cytometry experiments. Antibodies for western blotting include: Src (#2109), P-Src (#6943) FAK (#3285), P-FAK (#8556), Paxillin (#2542), P-Paxillin (#2541), Erk (#4695), P-Erk (#4370), p38 (#8690), P-p38 (#9211, all purchased from Cell Signaling Technologies).

### 2.5.7 Immunohistochemistry and immunofluorescent staining

For all immunohistochemistry and immunofluorescent studies, we used 4% paraformaldehyde-fixed frozen sections with 5-μm-thickness. For immunofluorescent staining, slides were air-dried for 1 hr at room temperature and hydrated with PBS for 10 min. After permeabilization with 0.5% tritonX-100 for 10 min, sections were blocked with PBS containing 5% chicken serum (#S-3000, Vector Laboratories) with 0.5% tritonX-100 for 1 hr at room temperature. Slides were then incubated with the indicated antibodies. For hematoxylin and eosin (H&E) staining, air-dried

slides were hydrated in PBS for 10 min, placed in hematoxylin for 10 min, and then rinsed in running tap water. After de-staining in 1% acetic acid for 5 min, slides were rinsed in tap water, and placed in 90% ethanol for 5 min. Slides were stained with eosin for 8 min, gradually dehydrated in ethanol solutions (from 80% to 100%), and then incubated with xylene for 10 min followed by mounting with Permount solution. For Masson's trichrome staining, air-dried slides were hydrated in distilled water for 10 min, placed in Mordant in Bousin's solution for 1 hr at 56°C, and rinsed in running tap water for 5 min. After staining in hematoxylin for 10 min, slides were washed in running tap water for 10 min, rinsed in distilled water, placed in Biebrich scarlet-acid fuchsin solution for 15 min, and stained in aniline blue solution for 10 min. After rinsing in distilled water, slides were differentiated in 1% acetic acid for 3 min, gradually dehydrated in ethanol solutions (from 80% to 100%), incubated with xylene for 10 min followed by mounting with Permount solution.

### 2.5.8 RNAscope and in situ hybridization (ISH)

To detect RNA transcripts for *SVEP1* and *ITGA9* in both human and mouse vascular tissues, a commercially available kit (#323100, RNAscope Multiplex Fluorescent Reagent Kit v2, Advanced Cell Diagnostics) was used according to the manufacturer's instructions. Briefly, 5-μm-thick 4% paraformaldehyde-fixed mouse aortic root, human aortic wall, and human LIMA frozen sections were air-dried for 1 hr at room temperature, and treated with hydrogen peroxide for 10 min to block endogenous peroxidase activity. After antigen retrieval by boiling in target antigen retrieval solution for 5 min at 95-100°C, slides were treated with protease III for 30 min at 40°C. Target probes (#406441, mouse *Svep1*; #540721, mouse *Itgα9*; #811671, human *SVEP1*; #811681, human *ITGA9*) were hybridized for 2 hr at 40°C, followed by a series of signal amplification and washing steps. Hybridization signals were detected by TSA Plus Cyanine 5,

and co-stained with the indicated antibodies. Slides were counterstained with DAPI by using ProLong Gold antifade reagent.

### 2.5.9 Flow cytometry

For labeling mouse blood cells, blood was collected from the retro-orbital plexus, and red blood cells were removed using RBC lysis buffer (#00-4300-54, eBioscience). For labeling human blood cells, Leuko spin medium (Pluriselect) was used to isolate leukocytes from peripheral blood and buffy coat. In experiments using mouse spleens, spleen cells were recovered from mice by cutting the spleen into small fragments and incubating with 400 U collagenase D (#11-088-858, Roche applied science) for 30 min at 37°C. For labeling aortic single cell suspensions, isolated aortas were perfused with DPBS, and opened longitudinally. The whole artery was cut into 2–5 mm pieces, and incubated in a Hanks' Balanced Salt Solution (HBSS) solution with calcium and magnesium containing 90 U $ml^{-1}$ DNase I (#DN25), 675 U $ml^{-1}$ collagenase I (#C0130), 187.5 U $ml^{-1}$ collagenase XI (#C7657), and 90 U $ml^{-1}$ hyaluronidase (#H1115000, all purchased from Sigma-Aldrich) for 70 min at 37°C with gentle shaking. Non-specific binding to Fc receptors was blocked, and cells were incubated with the indicated antibodies for 30 min at 4°C. For intracellular staining, cells were fixed/permeabilized with the FoxP3 transcription factor staining buffer set. Flow cytometric analyses were performed using LSRFortessa instrument (BD Biosciences) and FlowJo software (Tree Star Inc).

### 2.5.10 Bead labeling of Ly6C$^{low}$ monocytes recruited into atherosclerotic plaque

After 8 weeks of HFD feeding, 200 µL of 1 µm Fluoresbrite yellow-green (YG) microspheres beads (#17154-10, Polysciences, Inc) diluted 1:4 in sterile Dulbecco's phosphate-buffered saline (DPBS) were administered to mice retro-orbitally. Labeling efficiency of blood monocytes was verified by flow cytometry 3 days after YG bead injection. Recruitment of YG-beads positive

monocytes into plaque in aortic root was analyzed 1 day after checking labeling efficiency of YG beads. 5-μm-thick frozen sections of aortic root were stained with anti-Mac3, followed by anti-rat-Alexa594 antibody. And slides were mounted with ProLong Gold Antifade Mountant with DAPI. The number of YG-beads colocalized with Mac3 positive area was counted, or normalized with the percentages of labeled Ly6C$^{low}$ monocytes.

### 2.5.11 Primary cell isolation and culture

Mouse aortic VSMCs were isolated from 8-week-old *Apoe*$^{-/-}$ and *Svep1*$^{+/-}$*Apoe*$^{-/-}$, or same age of *Svep1*$^{SMC+/+}$and *Svep1*$^{SMC\Delta/\Delta}$ mice after tamoxifen injection for 10 consecutive days starting at 6 weeks of age. Briefly, thoracic aortas were harvested (3 mice per group were used), perivascular fat was removed, and then aortas were digested in 1 mg ml$^{-1}$ collagenase II (#LS004174), 0.744 units ml$^{-1}$ elastase (#LS002279), 1 mg ml$^{-1}$ soybean trypsin inhibitor (#LS003570, all purchased from Worthington Biochemical Corporation), and 1% penicillin/streptomycin in HBSS for 10 min at 37°C with gentle shaking. After a pre-digestion with enzyme mixture, the adventitial layer was removed under the dissection microscope, and the intimal layer was removed by scrapping with forceps. Aortas were cut into small pieces, and completely digested in enzyme mixture at 37°C for 1 hr with gentle shaking. VSMCs were grown in 20% fetal bovine serum (FBS, Hyclone) containing Dulbecco modified Eagle medium/F12 (DMEM/F12) media (Gibco) with 100 U ml$^{-1}$ penicillin/streptomycin at 37°C, 5% $CO_2$ incubator. After 2 passages, VSMCs were changed to 10% serum. To stimulate VSMCs, 50 μg ml$^{-1}$ human medium oxidized low density lipoprotein (oxLDL, #770202-7, Kalen biomedical) was used.

Human primary coronary artery smooth muscle cells (CASMCs) were obtained in their third passage from Invitrogen (#C-017-5C). Cells were grown in Medium 231 with Smooth Muscle

Growth Supplement (Gibco) and passaged according to the manufacturer's instructions. Medium lacking growth supplement was used in cell assays.

### 2.5.12 Quantitative real time PCR

Gene expression was quantified by quantitative real time PCR. RNA was isolated using RNeasy Mini Kit (#74106, Qiagen) according to manufacturer's protocol, and QIAshredder homogenizer (#79656, Qiagen) to increase yield of quantification of RNA. cDNA was synthesized with High Capacity cDNA Reverse Transcript Kit (#4368814). Real time PCR was performed using Taqman (#4444557) or SYBR™ Green (#A25742, all purchased from Applied Biosystems) assays. Ct values were normalized to *β-actin* (for Taqman) and *gapdh* (for SYBR Green), and showed as expression relative to control.

### 2.5.13 In vitro migration assay using peritoneal macrophages

*Itga9*$^{MAC+/+}$ and *Itga9*$^{MAC\Delta/\Delta}$ mice were injected intraperitoneally with 1 ml 4% thioglycolate. After 5 days, the peritoneal cells were collected by lavage and placed in Roswell Park Memorial Institute (RPMI) media containing 10% FBS for 60 min at 37°C. Non-adherent cells were removed after washing with PBS for 3 times, and adherent cells (more than 90% were peritoneal macrophages confirmed by flow cytometry) were placed in Trans-well inserts with a 5-µm porous membrane in a modified Boyden chamber. RPMI media containing 10% FBS with 50 or 200 ng ml$^{-1}$ SVEP1 protein was placed in the lower chamber. After allowing cell migration of 16 hr, inserts were removed from upper sider of the chamber, and nuclei of migrated cells to the lower side of the membrane were stained with DAPI. The number of migrated cells was determined by In Cell Analyzer 2000 (GE healthcare).

### 2.5.14 Proliferation and adhesion assays

Wells of a 96 well plate were pre-coated with 30 μg $ml^{-1}$ recombinant SVEP1 protein or bovine serum albumin (BSA, as an inert protein control). Wells were subsequently blocked with 10 mg $ml^{-1}$ BSA and washed twice with DPBS. Plates were ultraviolet (UV) sterilized before adding cells. For proliferation assays, primary VSMCs were collected and suspended in Dulbecco's Modified Eagle Medium/F12 media (DMEM/F12) containing 10% FBS. 2,000 cells were added to each well and incubated for 8 hr to assure complete cell adhesion. Media was then replaced with DMEM/F12 media containing 0.2% BSA and incubated for 12 hr to reduce basal proliferation rates. Cells were then incubated in BrdU dissolved in DMEM/F12 media containing 0.2% BSA for 30 hr. Predesigned Silencer Select siRNA constructs targeting *Itgα9* and negative control siRNA were obtained from ThermoFisher. Primary VSMCs were transfected using RNAiMAX transfection reagents according to the manufacturer's protocol. Efficient *Itgα9* knockdown was confirmed by qPCR. Cells were trypsinized 24 hr after transfection and used for the proliferation assay. DAPT or DMSO (carrier) were added to cells throughout the indicated experiment at a concentration of 25 μM. A similar protocol was adapted to test proliferation of human CASMCs, with a 24 hr incubation in BrdU-containing media. For using peritoneal macrophages, 4% thioglycolate-elicited peritoneal macrophages from $Itg\alpha9^{MAC+/+}$ and $Itg\alpha9^{MAC\Delta/\Delta}$ mice were suspended in BrdU-containing RPMI 1640 media that also contained 10% FBS. 25,000 cells were added to each well since peritoneal macrophages have lower proliferation rates than VSMCs in culture. 50 μg $ml^{-1}$ oxLDL was added to the indicated cells at the beginning of this incubation. An enzyme-linked immunoassay (ELISA) for incorporated BrdU was then performed using kit instructions (#6813, Cell Signaling Technologies) after incubation for 36 hr. Adhesion assays were performed in precoated 96-well plates blocked with 100 mg $ml^{-1}$ BSA. Blocking conditions were empirically derived to minimize non-specific cell

adhesion. After a 5 (for THP-1 cells) or 15 (for VSMCs) min incubation, non-adhered cells were removed by gently centrifuging the plates upside down. VSMCs were counted manually and THP-1 cells were counted by automated microscopy after staining cells with DAPI.

### 2.5.15 Western blot assay

Cells were resuspended in serum free media (SFM), and incubated with gentle agitation to prevent cell attachment and reduce basal signaling. Cells were washed with SFM then seeded on BSA-blocked plates coated with either BSA, VCAM-1, SVEP1, or SVEP1$^{CADrv}$. Concentrations of VCAM-1 and SVEP1 were derived empirically to prevent signal saturation. BSA concentrations always matched the SVEP1 concentration. It is only appropriate, therefore, to compare between BSA, SVEP1, and SVEP1$^{CADrv}$ groups. Cells were briefly centrifuged to the bottom of the wells and incubated for 8 min (for VSMCs) or 15 min (for THP-1 cells) before lysis with cell lysis buffer (#9803, Cell Signaling Technologies) containing a cocktail of protease and phosphatase inhibitors. Western blots were performed by standard techniques, as briefly follows. Protein content was determined using a bicinchoninic acid assay with BSA standards (#23225, Pierce BCA Protein Assay Kit). Cell lysates were then reduced with dithiothreitol (DTT) in lithium dodecyl sulfate sample buffer (#NP0007, Invitrogen). Equal protein amounts were added to polyacrylamide gels (#4561086, BioRad) and electrophoresed prior to transferring to a nitrocellulose or polyvinylidene fluoride membrane (#1620260, BioRad). Membranes were blocked in 5% BSA/Tris-Buffered Saline with tween 20 for 30 min. The indicated primary antibodies were incubated with the pre-blocked membranes overnight at 4°C. Membranes were washed with Tris-Buffered Saline with tween 20, probed with fluorescent secondary antibodies, and imaged. β-actin or β-tubulin served as a loading control.

### 2.5.16 Bulk RNA sequencing and analysis

Primary VSMCs were plated on wells precoated with 30 μg $ml^{-1}$ recombinant SVEP1, $SVEP1^{CADrv}$ protein or BSA (as an inert protein control). Wells were subsequently blocked with 10 mg $ml^{-1}$ BSA and washed twice with DPBS. Plates were UV sterilized before adding cells. Primary VSMCs were collected, resuspended in DMEM/F12 media containing 10% FBS, plated on precoated, blocked wells, and incubated for 8 hr to ensure complete cell adhesion. Media was replaced with fresh DMEM/F12 containing 1% FBS and incubated for 12 hr before collection. RNA was collected using RNeasy Mini Kit (#74106, Qiagen). Atherosclerotic aortic arches (including the aortic root, arch, and the proximal regions of its branching vessels) from mice were used as the source of RNA for the later RNAseq experiment. These tissues were isolated and separated from the perivascular adipose and stored in RNAlater (#AM7021, Thermofisher) prior to total RNA extraction using nucleoZOL (Macherey-Nagel). cDNA for validation was synthesized with High Capacity cDNA Reverse Transcript Kit (#4368814, Applied Biosystems), following standard protocols.

Samples were prepared according to library kit manufacturer's protocol, indexed, pooled, and sequenced on an Illumina HiSeq. Basecalls and demultiplexing were performed with Illumina's bcl2fastq software and a custom python demultiplexing program with a maximum of one mismatch in the indexing read. RNA-seq reads were then aligned to the Ensembl release 76 primary assembly with STAR version 2.5.1a (*68*). Gene counts were derived from the number of uniquely aligned unambiguous reads by Subread:featureCount version 1.4.6-p5 (*69*). Isoform expression of known Ensembl transcripts were estimated with Salmon version 0.8.2 (*70*). Sequencing performance was assessed for the total number of aligned reads, total number of uniquely aligned reads, and features detected. The ribosomal fraction, known junction saturation, and read distribution over known gene models were quantified with RSeQC version 2.6.2 (*71*).

All gene counts were then imported into the R/Bioconductor package EdgeR (*72*) and TMM normalization size factors were calculated to adjust for samples for differences in library size. Ribosomal genes and genes not expressed in the smallest group size minus one sample greater than one count-per-million were excluded from further analysis. The TMM size factors and the matrix of counts were then imported into the R/Bioconductor package Limma (*73*). Weighted likelihoods based on the observed mean-variance relationship of every gene and sample were then calculated for all samples with the voomWithQualityWeights (*74*). The performance of all genes was assessed with plots of the residual standard deviation of every gene to their average log-count with a robustly fitted trend line of the residuals. Differential expression analysis was then performed to analyze for differences between conditions and the results were filtered for only those genes with Benjamini-Hochberg false-discovery rate adjusted *P*-values less than or equal to 0.05. One sample in the aortic arch experiment was independently identified as an outlier by standard quality control methods. This group was excluded from downstream analyses. For each contrast extracted with Limma, global perturbations in known Gene Ontology (GO) terms, KEGG pathways, and InterPro domains were detected using the Database for Annotation, Visualization and Integrated Discovery (DAVID) (*75*) on significantly dysregulated transcripts or using the R/Bioconductor package GAGE (*76*) to test for changes in expression of the reported log 2 fold-changes reported by Limma in each term versus the background log 2 fold-changes of all genes found outside the respective term. The R/Bioconductor package heatmap3 (*77*) was used to display heatmaps across groups of samples for each GO or MSigDb term with a Benjamini-Hochberg false-discovery rate adjusted p-value less than or equal to 0.05. Perturbed KEGG pathways where the observed log 2 fold-changes of genes within the term were significantly perturbed in any direction compared to other genes within a given term with *P*-

values less than or equal to 0.05 were rendered as annotated KEGG graphs with the R/Bioconductor package Pathview (*78*).

### 2.5.17 Notch signaling assays

Cells were collected, resuspended in SFM, and incubated for 1 hr with gentle agitation before seeding on tissue culture wells that were precoated and blocked, as described in previous sections. Cells were collected for analysis after 4 hr of growth on the indicated substrate. *Svep1*$^{SMC+/+}$and *Svep1*$^{SMC\Delta/\Delta}$ VSMCs were collected for analysis after 72 hr of incubation in SFM to obtain basal Notch signaling.

### 2.5.18 Analysis of cytokine and chemokine biomarkers

MILLIPLEX MAP Mouse Cytokine/Chemokine Magnetic Bead Panel-Immunology Multiplex Assay (#MCYTOMAG-70K), MILLIPLEX MAP Mouse Angiogenesis/Growth Factor Magnetic Bead Panel-Cancer Multiplex Assay (#MAGPMAG-24K), and MILLIPLEX MAP Mouse Cardiovascular Disease (CVD) Magnetic Bead Panel 1-Cardiovascular Disease Multiplex Assay (#MCVD1MAG-77K-02, all from Millipore Sigma) were used to analyze cytokines and chemokines from mouse plasma. All kits were used according to manufacturer recommended protocols. Briefly, the Luminex FLEXMAP 3D (Luminex Corporation) instrument was used to sort the magnetic polystyrene beads and measure the phycoerythrin (PE) tagged detection antibody signal. Fifty beads from each analyte were measured. The median fluorescent intensity (MFI) was compared against the standard curve to calculate the pg $ml^{-1}$ or ng $ml^{-1}$ using Milliplex Analyst 5.1 software (VigeneTech.com) and a 5-parameter logistic curve fit algorithm.

### 2.5.19 BMDM isolation and culture

6- to 8-week-old *Itgα9*$^{MAC+/+}$ and *Itgα9*$^{MACΔ/Δ}$ mice were euthanized by carbon dioxide inhalation, and soaked in 75% ethanol. Then, femurs and tibias were harvested and bone-marrow cells were obtained by flushing bones and differentiated for 7 days in DMEM media supplemented with 50 ng ml$^{-1}$ recombinant macrophage-colony stimulating factor (M-CSF, R&D systems), 20% heat-inactivated FBS, and antibiotics.

### 2.5.20 Mendelian Randomization

Genome-wide summary statistics for risk of CAD were obtained from a meta-analysis of CAD using data from CARDIoGRAMPlusC4D and the UK Biobank as previously described (*10*). Genome-wide summary statistics for hypertension and type 2 diabetes (T2D) were obtained from the Integrative Epidemiology Unit (IEU) GWAS database (*79*) using association results from the UK Biobank. Summary statistics for primary hypertension (ICD 10 code I10) as a secondary diagnosis (IEU GWAS ID “ukb-b-12493") were used for hypertension while summary statistics for diabetes diagnosed by a doctor (IEU GWAS ID “ukb-b-10753") were used for T2D.

A genome-wide association study to identify protein quantitative trait loci (pQTL) using a SomaLogic aptamer-based protein assay has previously been described (*26*). Two aptamers (SVEP1.11109.56.3 and SVEP1.11178.21.3) were used to estimate SVEP1 protein concentration. We obtained genome-wide summary statistics for both aptamers which produced highly similar results; for simplicity, results from the analysis using the SVEP1.11178.21.3 aptamer were reported. As trans-pQTLs might affect protein levels in a variety of manners, we focused our analysis on cis-pQTLs by only including variants in a 1Mb window surrounding SVEP1 which associated with plasma SVEP1 concentration at a level exceeding genome-wide significance (*P*-value for SVEP1 concentration $< 5 \times 10^{-8}$). We filtered these SNPs using pair-wise linkage disequilibrium estimated from the 1000 Genomes Project European samples in

order to obtain an independent ($r^2 < 0.3$) set of SNPs for the causal analysis. Causal estimates were calculated using the inverse-variant weighted method implemented in the R package TwoSampleMR (*79, 80*).

## 2.6 Chapter acknowledgements

We thank all the members of the Stitziel Lab for helpful discussion and Upasana Pudupakkam for technical assistance. We thank the Genome Technology Access Center in the Department of Genetics at Washington University School of Medicine for help with genomic analysis.
The Center is partially supported by NCI Cancer Center Support Grant #P30 CA91842 to the Siteman Cancer Center and by ICTS/CTSA Grant# UL1TR002345 from the National Center for Research Resources (NCRR), a component of the National Institutes of Health, and NIH Roadmap for Medical Research. We thank the Bursky Center for Human Immunology and Immunotherapy Programs at Washington University, Immunomonitoring Laboratory for help with analysis of mouse plasma. This publication is solely the responsibility of the authors and does not necessarily represent the official view of NCRR or NIH. The *Svep1* mouse strain used for this research was created from ES cell clone HEPD0747_6_B06, generated by the European Conditional Mouse Mutagenesis Program which was then made into mice and provided to the KOMP Repository (www.komp.org) by the Jackson Laboratory as part of the KOMP2 Project. The Genotype-Tissue Expression (GTEx) Project was supported by the Common Fund of the Office of the Director of the National Institutes of Health, and by NCI, NHGRI, NHLBI, NIDA, NIMH, and NINDS. Data used for the analyses described in this manuscript were obtained from the GTEx Portal on 04/30/2020. **Funding:** This work was supported in part by grants from the National Institutes of Health (NIH) T32GM007200 and T32HL134635 to JSE, NIH T32HL007081 to EPY, NIH R01HL53325 to RPM, along with NIH grants R01HL131961,

UM1HG008853, UL1TR002345, an investigator-initiated research grant from Regeneron Pharmaceuticals, a career award from the National Lipid Association, and by the Foundation for Barnes-Jewish Hospital to NOS.

# Chapter 3

# The developmental switch hypothesis

## 3.1 Introduction

*Svep1* is produced by cells that express SMα-actin within atherosclerotic plaque (3). These cells comprise the cap of the atheroma and contain the greatest fraction of proliferating VSMC-derived cells within plaque at various timepoints (89). Many cells derived from mature VSMCs invest into the plaque core and lose their VSMC markers in a process known as phenotype shifting (84, 115). Studies of VSMCs in vitro contrast the finding that differentiated VSMCs (those cells that express canonical VSMC markers) are the most proliferative subpopulation of VSMC-derived cells within plaque. Rather, cultured VSMC proliferation is generally associated with the extent of phenotype shifting (127). The discrepancy between VSMC behavior in plaque compared to in vitro is poorly understood.

VSMC expansion within plaque is also recognized as a mono or oligo-clonal process (89, 128). A single (or a few) VSMC migrates to the luminal side of a developing atheroma, undergoes extensive proliferation, and eventually constitutes a large portion of the total plaque volume and cell count (89, 112). The VSMCs derived from the initial clone demonstrate remarkable plasticity and have been described to exist as mesenchymal-like VSMCs, contractile VSMCs, myofibroblast-like VSMCs, synthetic VSMCs, endothelial-like cells, osteochondrogenic VSMCs, adipocyte-like cells, foam cells, and macrophage-like cells (129). The process of clonal VSMC expansion and differentiation, followed by loss of proliferative capacity, is analogous to mechanisms of stem cell biology. This suggests a developmental switch may protect a

multipotent VSMC from differentiation while driving continued proliferation in a process known as self-renewal (130). Conversely, daughter cells lose their ability to self-renew and differentiate into a specialized cell-type. A delicate balance of these two processes enables a clonal expansion of cells exhibiting numerous different phenotypes, as observed in atherosclerosis. The ECM is thought to play an important role in regulating the VSMC behaviors observed in atherogenesis (89, 112, 129). We therefore sought to test the hypothesis that SVEP1 may regulate VSMC behavior through a developmental switch paradigm.

# 3.2 Results

## 3.2.1 Proteomic analysis of recombinant and plasma SVEP1

We first sought to characterize the recombinant, purified SVEP1 used in chapter 2. This was necessary because the protein is known to be cleaved during its secretion (2), and the poly-His tag used for purification is only present on the C-terminus of the protein (3). We therefore performed mass spectrometry analysis of the purified protein. Consistent with published findings (2), we detected peptides spanning the entire length of the protein, suggesting we were retaining both termini in the purification process (Figure 3.1). We also performed mass spectrometry on the recombinant, poly-His tagged N-terminus of the protein. As expected, we were able to detect SVEP1 peptides that mapped almost exclusively to the N-terminus of SVEP1 (Figure 3.2).

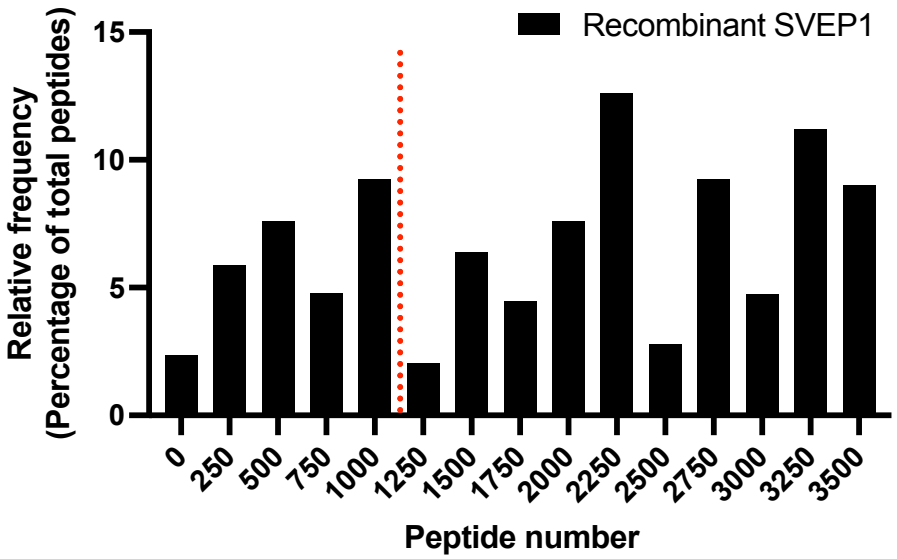


Figure 3.1 Histogram of peptides detected from full-length, purified recombinant SVEP1. Recombinant, full length SVEP1 was produced and purified as described previously (3). The peptides were generated and subjected to ultra-performance liquid chromatography-trapped ion mobility spectrometry time of flight mass spectrometry (UPLC-timTOF MS), as described in chapter 5. The red dashed line designates the canonical cleavage site (2).

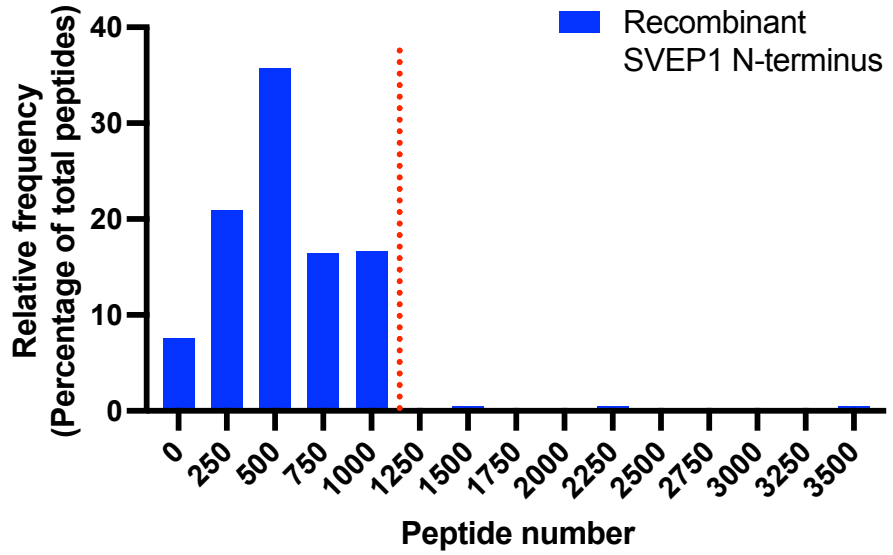


Figure 3.2 Histogram of peptides detected from the purified recombinant SVEP1 N-terminus. Recombinant, SVEP1 N-terminus was produced and purified similar to methods described previously (3). The peptides were generated and subjected to UPLC-timTOF MS, as described in chapter 5. The red dashed line designates the canonical cleavage site (2).

Given the evidence that SVEP1 is cleaved during secretion, we sought to test which regions of the protein within tissue were detected by mass spectrometry. To assess this, we utilized a human

plasma database from the Peptide Atlas (131), since SVEP1 circulates in plasma. Like the full-length recombinant SVEP1, peptides were detected throughout the entire length of SVEP1 obtained from plasma, suggesting both termini are present (Figure 3.3). Similar results were obtained from other tissue sources of SVEP1 (not shown). Based on these data, we tested the response of VSMCs to the full-length, purified SVEP1.

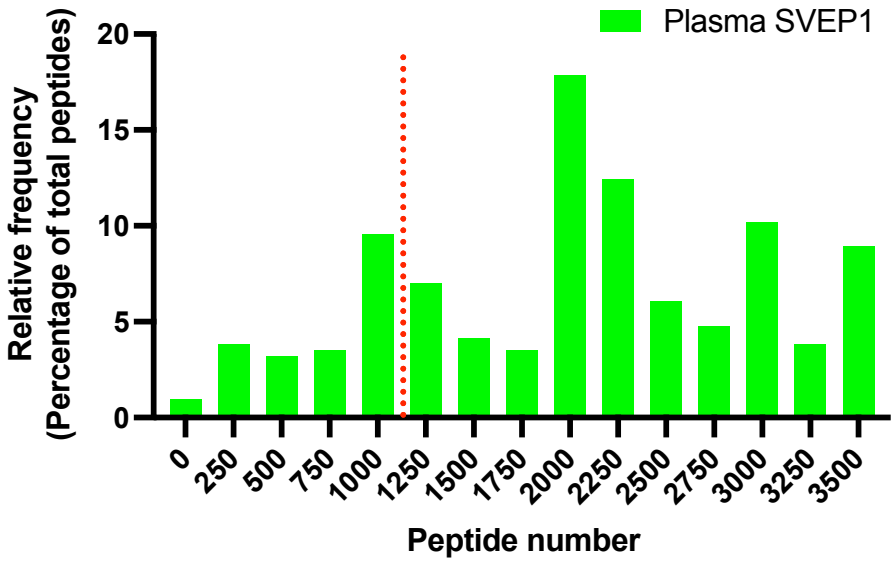


Figure 3.3 Histogram of SVEP1 peptides detected in human plasma.
Data were obtained from the Peptide Atlas Build Human Plasma 2012-08 (131).

### 3.2.2 VSMCs grown on SVEP1 have altered morphology

VSMC phenotype shifting is often accompanied by a change in cell morphology. Mature, contractile VSMCs have a characteristic spindle-like morphology, whereas phenotype-shifted, synthetic VSMCs often have a epithelioid or cobblestone morphology (132). To test the effects of SVEP1 on VSMC morphology, we seeded murine VSMCs on slides precoated with BSA (negative control) or SVEP1. After attachment, the cells were treated with serum-free media overnight. The cells were then stained with DAPI, Ki67 (a proliferation marker (133)), and phalloidin (a toxin that binds to filamentous actin (134)) and imaged using confocal microscopy. Compared to cells grown on BSA, cells grown on SVEP1 had a more epithelioid morphology

with numerous apparent adhesion sites (Figure 3.4). Consistent the induction of cell proliferation in response to SVEP1 (3), more cells grown on SVEP1 stained with Ki67. These observations are consistent with SVEP1-induced cell proliferation and suggest SVEP1 may induce phenotype shifting of VSMCs.

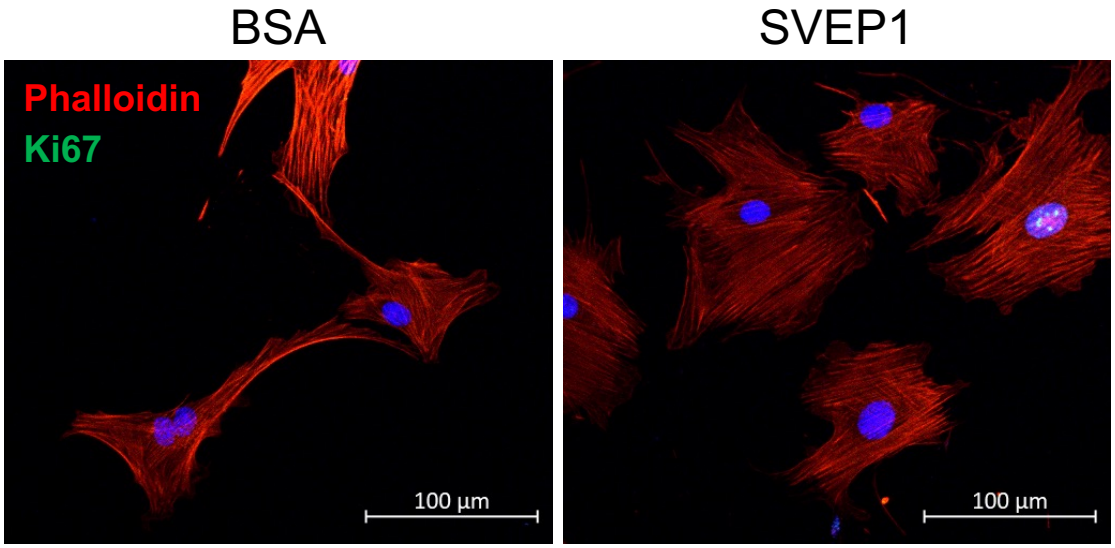


Figure 3.4 Confocal images of VSMCs grown on BSA or SVEP1.
Murine VSMCs were seeded on slides precoated with BSA or SVEP1. Cells were stained and imaged after serum starvation overnight.

### 3.2.3 VSMC phenotype is influenced by SVEP1

We next tested the transcription of canonical VSMC differentiation and dedifferentiation markers after exposure to SVEP1, relative to cells exposed to BSA. Paradoxically, cells grown on SVEP1 exhibited increased expression of VSMC contractile markers, including *Acta2*, *Cnn1*, *Smtn*, and *Tagln* (Figure 3.5). Reciprocally, cells grown on SVEP1 expressed lower levels of dedifferentiation markers, including *Ly6a*, *Mgp*, and *Spp1* (112, 135).

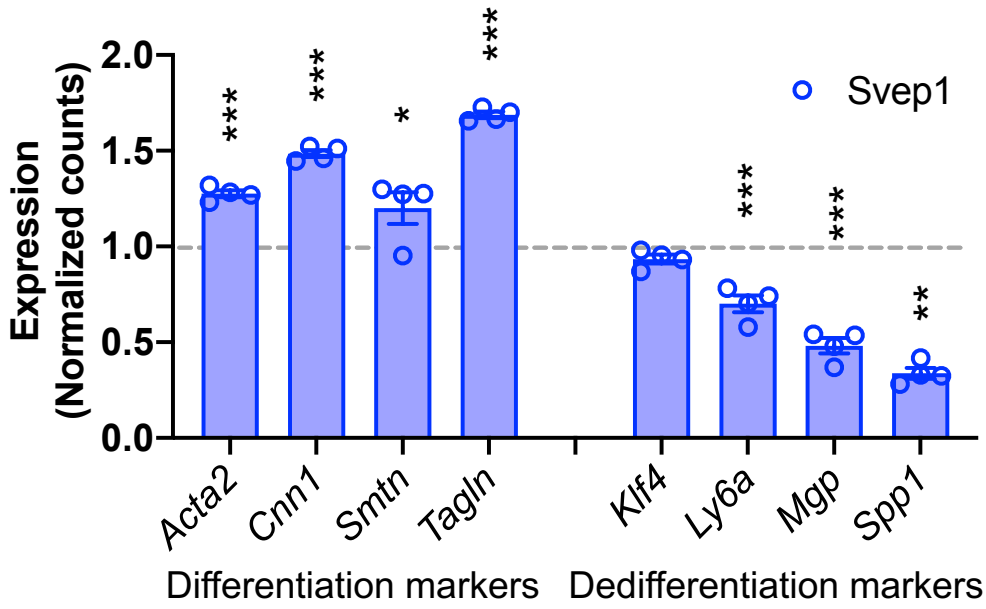


Figure 3.5 Phenotype of cells grown on SVEP1.
Transcription of genes associated with VSMC differentiation of dedifferention after exposure to SVEP1. Transcript levels are normalized to cells grown on BSA.

We next measured transcription of *Krüppel-like factor 4* (*Klf4*) and *Lgals3* in wildtype or *Svep1*$^{-/-}$ VSMCs with and without the treatment of cholesterol. *Klf4* and *Lgals3* are markers of phenotype shifting and increase in response to cholesterol treatment (115, 136). As expected, transcription of both genes increased with exposure to cholesterol (Figure 3.6). Cells lacking *Svep1* also expressed higher levels of both genes. This is directionally consistent with the previous findings and suggests SVEP1 promotes a contractile phenotype, in contrast to the effects of SVEP1 on proliferation and cell morphology.

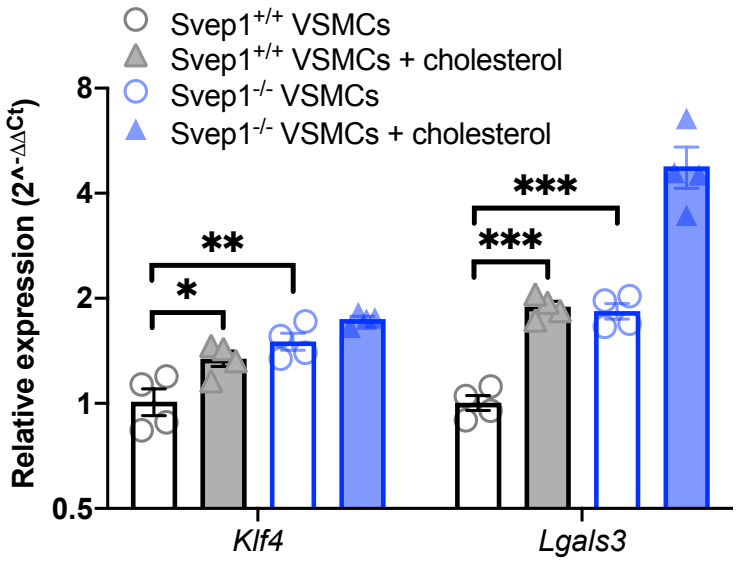


Figure 3.6 Phenotype of VSMCs lacking *Svep1*.
Transcription of markers associated with VSMC phenotype shifting were assessed in wildtype (*Svep1*$^{+/+}$) and *Svep1*$^{-/-}$ VSMCs with or without the treatment of cholesterol.

### 3.2.4 Effects of Notch and integrin α9β1 inhibition on VSMC phenotype

SVEP1 has been shown to promote Notch and integrin signaling (3). We hypothesized that these pathways may be responsible for the effects of SVEP1 on VSMC phenotype. Notch signaling was inhibited with the small molecule DAPT and integrin α9β1 with siRNA against *Itga9*, as previously described (3). Inhibition of Notch signaling decreased contractile VSMC markers and increased *Lgals3* (Figure 3.7). Knockdown of *Itga9* has little effect on the contractile markers but promoted *Lgals3* transcription. These data are consistent with the direction of effect of SVEP1 on VSMC phenotype and suggest that SVEP1 may influence VSMC phenotype by promoting Notch and/or integrin signaling.

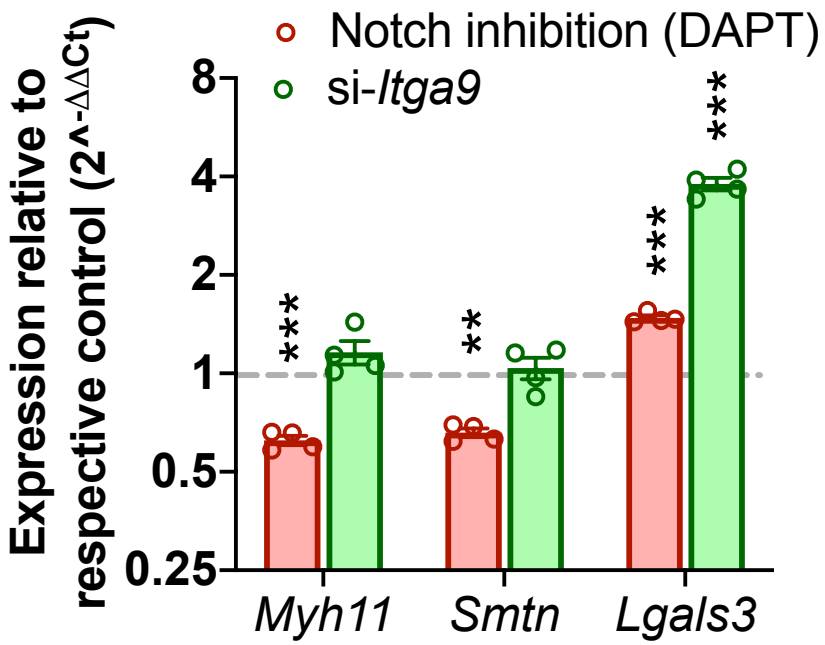


Figure 3.7 Effects of Notch and *Itga9* inhibition on VSMC phenotype. Expression of the listed transcripts were measured by qPCR.

### 3.2.5 The SVEP1 developmental switch hypothesis

The Notch and integrin signaling pathways are powerful regulators of VSMC phenotype (137-139) and are both induced by SVEP1 (3). SVEP1, Notch, and integrin α9β1 promote VSMC proliferation and differentiation to a contractile phenotype. These data present a paradox, however, since SVEP1 and Notch signaling in VSMCs have been experimentally determined to be pro-atherogenic yet maintain VSMC in a differentiated state (138, 140), which is generally regarded as atheroprotective. Adding to this paradox is that Notch reciprocally antagonizes Klf4 signaling (141, 142), which is also pro-atherogenic and necessary for phenotype shifting of VSMCs (115). We also confirmed that *Itga9* is Notch target gene in VSMCs (Figure 3.8), as described in other cell types (143) Strikingly, knockdown of *Itga9* robustly activates Notch signaling and *Klf4* (Figure 3.8).

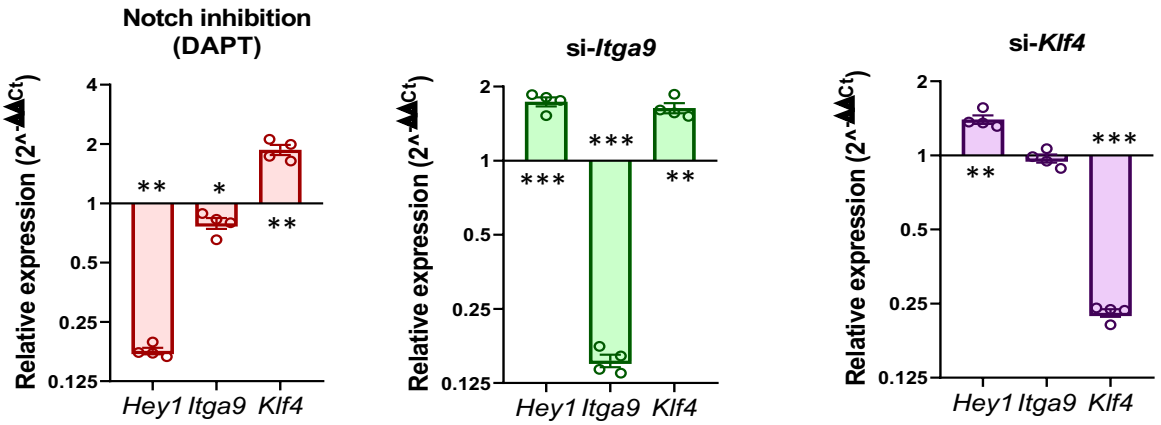


Figure 3.8 Reciprocal interactions between Notch, Itga9, and Klf4.
Transcriptional analysis of *Hey1*, a Notch target gene, *Itga9*, and *Klf4* in VSMCs in response to inhibiting each pathway or gene.

## 3.3 Discussion

The effect of SVEP1, Notch, integrin α9β1, and Klf4 on VSMC phenotype and their reciprocal interactions led to the VSMC developmental shift hypothesis (Figure 3.9). In short, this hypothesis states that SVEP1, Notch, and integrin α9β1 maintain a differentiated, yet proliferative and plastic population of VSMCs in atherosclerosis. These pathways must be in opposition to differentiation pathways, including Klf4 signaling, lest VSMCs lose their proliferative capacity, since Klf4 inhibits VSMC proliferation (144-146). This is consistent with recent lineage studies that have demonstrated that the differentiated cells of the plaque cap (which express Notch receptors, *Svep1*, and *Itga9*) preferentially proliferate relative to the dedifferentiated VSMC-derived cells (which express Klf4) (89). Theoretically, inhibiting either one of these processes would result in a self-limiting disease process by either preventing VSMC dedifferentiation or preventing the proliferation or self-renewal of VSMCs (147).

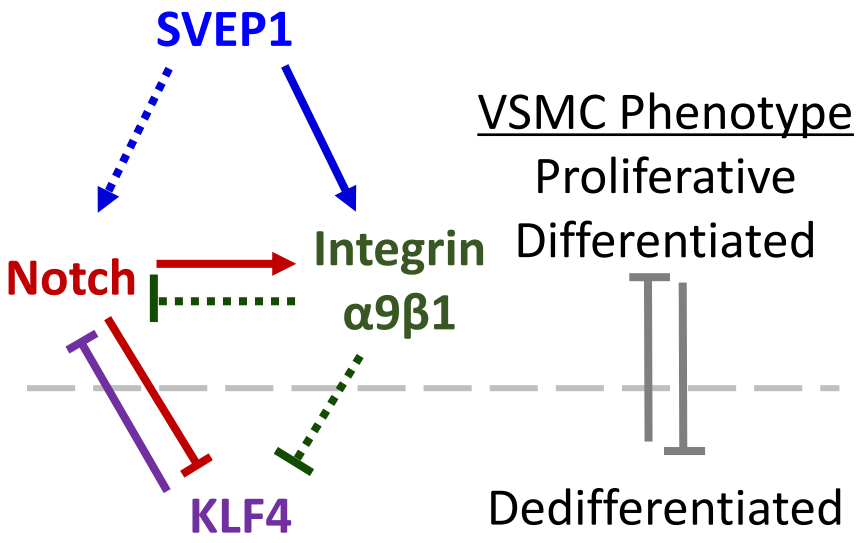


Figure 3.9 The SVEP1 developmental switch hypothesis.
A graphical summary of the developmental switch hypothesis, based on evidence provided within this dissertation (dashed lines), or reported in the scientific literature (solid lines).

## 3.4 Methods

The methods used in this chapter were adapted from the methods listed in Chapter 2 and Chapter 5 of this dissertation.

# Chapter 4

# The cardiometabolic effects of SVEP1 depletion[2]

## 4.1 Introduction

Given the causal association between SVEP1 and T2D in humans (3, 7), we previously sought to characterize the metabolic state of *Svep1*$^{+/-}$ mice. Preliminary data suggested chow-fed *Svep1*$^{+/-}$ mice at 20 weeks of age had a modest improvement in glucose control compared to *Svep1*$^{+/+}$ controls, as determined by an intraperitoneal glucose tolerance test, and a possible altered response to an intraperitoneal insulin challenge (unpublished). A potential role for *Svep1* in regulating adiposity was also revealed during our experimental assessment of atherosclerosis in our VSMC specific deletion model (3). Although this difference was not statistically significant, the experiment was designed to evaluate atherosclerosis after only 8 weeks of HFD, and the apparent difference in body mass seemed to be increasing with age. These preliminary data were compelling but contained several limitations, including a small sample size and non-ideal controls. To properly determine the effects of *Svep1* depletion in metabolism and obesity, we decided to use mice on an *Apoe*$^{+/+}$ background and compare them to true littermate controls

[2] Chapter 4 was modified and later licensed under a Creative Commons Attribution 4.0 International License by Nature Springer

https://creativecommons.org/licenses/by/4.0/

https://www.nature.com/articles/s41467-023-36486-0

Creators include: Jared S. Elenbaas, Upasana Pudupakkam, Katrina J. Ashworth, Chul Joo Kang, Ved Patel, Katherine Santana, In-Hyuk Jung, Paul C. Lee, Kendall H. Burks, Junedh M. Amrute, Robert P. Mecham, Carmen M. Halabi, Arturo Alisio, Jorge Di Paola & Nathan O. Stitziel

(148). Increased age and/or HFD feeding were also used to induce chronic metabolic stress and obesity in the mouse models (149).

## 4.2 Results

### 4.2.1 *SVEP1* is highly expressed by adipocyte precursor cells within adipose.

Human adipose expresses high levels of *SVEP1* (Figure 4.1A). Adipocyte precursors, a $CD34^+$ sub-fraction of the adipose stromal vascular fraction, are the main source of SVEP1 expression within adipose (150) (Figure 4.1B). To investigate *Svep1* expression in mice, we harvested visceral fat from 20-week-old $Svep1^{+/LacZ}$ animals and performed X-gal staining of whole mount adipose tissue. We observed X-gal positive cells in the perivascular region from $Svep1^{+/LacZ}$ animals but not mature adipocytes, consistent with preadipocyte expression of *Svep1* (Figure 4.1C). Immunofluorescent staining for Myh11 on X-gal stained adipose demonstrated a population of cells co-expressing both *Svep1* and Myh11 (not shown). Subsequent qPCR confirmed high expression in the stromal vascular fractions of subcutaneous and visceral adipose from $Svep1^{+/+}$ mice (data not shown).

A failure in preadipocyte maturation (adipogenesis) in response to nutrient excess, such as HFD feeding, results in adipocyte hypertrophy and ectopic fat deposition (151). This is strongly associated with metabolic dysfunction, T2D, and cardiovascular disease (152). *SVEP1* expression in human adipose positively correlates with adipocyte hypertrophy (153), supporting the hypothesis that SVEP1 negatively regulates adipogenesis. Similar mechanisms have been reported for other EGF-containing proteins such as Dlk1 (154) and Notch ligands (155).

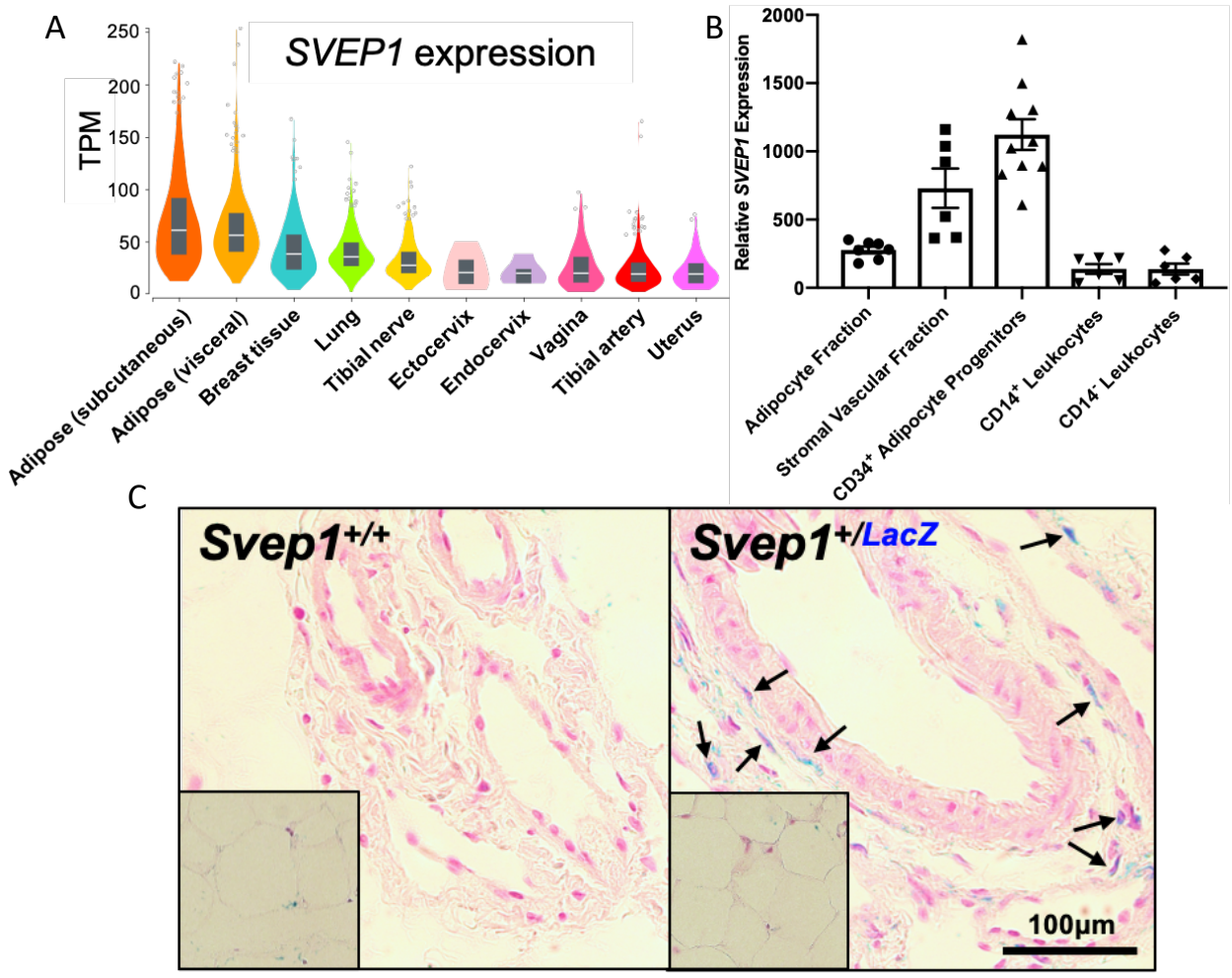


Figure 4.1 *SVEP1* is expressed by preadipocytes within adipose.
(A) Expression of *SVEP1* as determined by RNAseq in the top 10 *SVEP1*-expressing tissues from the Genotype Expression Tissue Project (www.gtexportal.org). Transcripts per million (TPM) reflects SVEP1 expression. (B) Relative SVEP1 expression in various adipose cell populations after fractionation and FACS sorting of explanted adipose. Data obtained from Gene Expression Omnibus (accession GSE80654). Error bars=SEM. (C) X-gal staining of adipose tissue demonstrating lacZ expressing cells indicated by arrows found in the peri-vascular space consistent with pre-adipocytes. Inset shows minimal staining in mature adipocytes.

### 4.2.2 Loss of *Svep1* in post-developmental mice is metabolically well-tolerated.

We sought to characterize the chronic impact of complete SVEP1 depletion metabolic phenotypes in post-developmental mice. Six-week-old *Svep1*$^{flx/flx}$*Rosa26-Cre*$^{ERT2}$ (referred to as *Svep1*$^{-/-}$) and control littermate *Svep1*$^{+/+}$*Rosa26-Cre*$^{ERT2}$ (referred to as *Svep1*$^{+/+}$) mice were

injected intraperitoneally with tamoxifen to delete SVEP1, as done previously (3). Mice were fed a Western high-fat, high-cholesterol diet (HFD) beginning at 8 weeks of age to induce cardiometabolic stress (156-158). Both *Svep1*$^{+/+}$ and *Svep1*$^{-/-}$ mice gained body mass while being maintained on HFD. No appreciable differences were observed in body mass between the two genotypes of mice throughout the duration of HFD feeding (Figure 4.2A). Similarly, compared to littermate controls, *Svep1*$^{-/-}$ mice had no appreciable differences in lean mass, fat mass, and total water, as determined by EchoMRI™ (Figure 4.2B-D). *Svep1*$^{+/+}$ and *Svep1*$^{-/-}$ mice also had similar responses to glucose tolerance tests (GTT, Figure 4.2E) and lacked insulin sensitivity, as determined by insulin tolerance tests (ITT, Figure 4.2F)(156). The metabolic activity of the mice was also tested using indirect calorimetry. Again, no significant differences were observed between *Svep1*$^{+/+}$ and *Svep1*$^{-/-}$ mice in respiratory exchange ratio (Figure 4.2G) or energy consumption (Figure 4.2H). Collectively, these data suggest that whole-body deletion of *Svep1* in post-developmental mice with diet-induced diabetes does not result in an overt impact on body mass, body composition, glucose handling, respiratory exchange ratio, or metabolic rate and suggest that loss of SVEP1 is metabolically well-tolerated in adult mice.

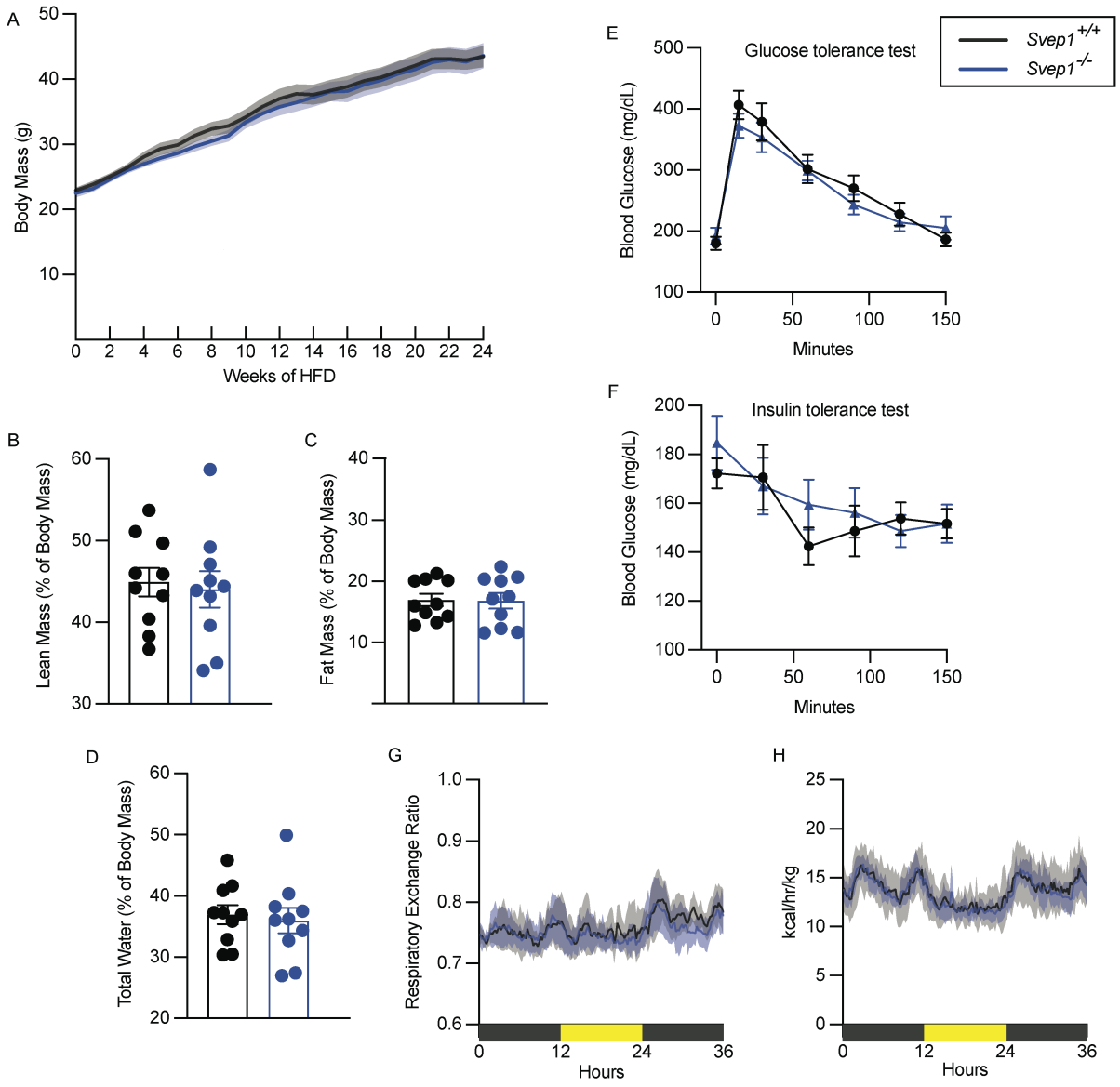


Figure 4.2 The effects of whole-body SVEP1 depletion on metabolism in mice. (A) Weekly body mass measurements of *Svep1*$^{+/+}$ and *Svep1*$^{-/-}$ mice after 6 months of HFD feeding. N = 12-13. Shaded region represents SEM. (B-D) Lean mass (B), fat mass (C), total water (D) of *Svep1*$^{+/+}$ and *Svep1*$^{-/-}$ mice after 6 months of HFD feeding, as determined by EchoMRI™. N = 10. (E) Blood glucose measurements of *Svep1*$^{+/+}$ and *Svep1*$^{-/-}$ mice after intraperitoneal glucose administration at 0 minutes. N = 11-13. (F) Blood glucose measurements of *Svep1*$^{+/+}$ and *Svep1*$^{-/-}$ mice after intraperitoneal insulin administration at 0 minutes. N = 12-13. (G) Respiratory exchange ratio of *Svep1*$^{+/+}$ and *Svep1*$^{-/-}$ mice, as determined by indirect calorimetry. N = 8. Shaded regions represent 95% confidence intervals. (H) Metabolic rate (kcal/hr/kg) of *Svep1*$^{+/+}$ and *Svep1*$^{-/-}$ mice, as determined by indirect calorimetry. N = 8. Shaded regions represent 95% confidence intervals.

### 4.2.3 *Svep1* heterozygosity is metabolically well-tolerated.

We then asked whether *Svep1*$^{-/+}$ mice have a metabolic phenotype, relative to *Svep1*$^{+/+}$ controls. After 16 weeks of HFD feeding, *Svep1*$^{-/+}$ mice had similar weight gain compared to littermate controls (Figure 4.3A-B). *Svep1*$^{-/+}$ mice also had similar glucose and insulin tolerance, relative to controls (Figure 4.4A-D). The mass of tissues dissected from *Svep1*$^{-/+}$ mice were also similar to control mice. This included inguinal adipose, perigonadal adipose, brown adipose, and liver (Figure 4.5A-D). Body composition analysis was also similar between the two genotypes of mice (Figure 4.6). Based on these data, we could not appreciate any metabolic phenotype in *Svep1*$^{-/+}$ mice, suggesting *Svep1* heterozygosity is metabolically well-tolerated in mice.

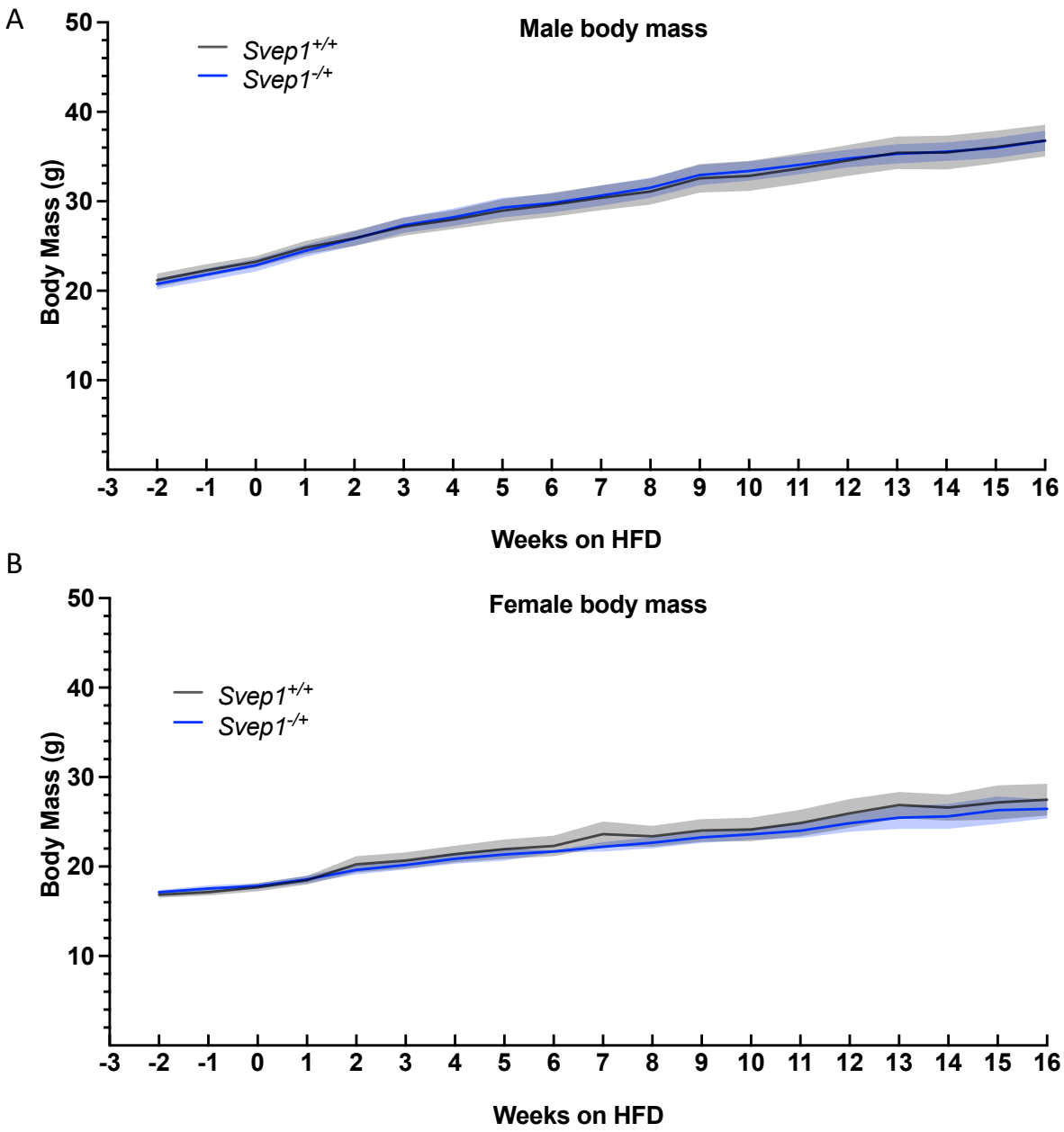


Figure 4.3 *Svep1* haploinsufficiency does not influence weight gain.
(A, B) Weekly body mass measurements of *Svep1*$^{+/+}$ and *Svep1*$^{-/+}$ male (A) and female (B) mice after 16 weeks of HFD feeding. N = 5-8. Shaded region represents SEM.

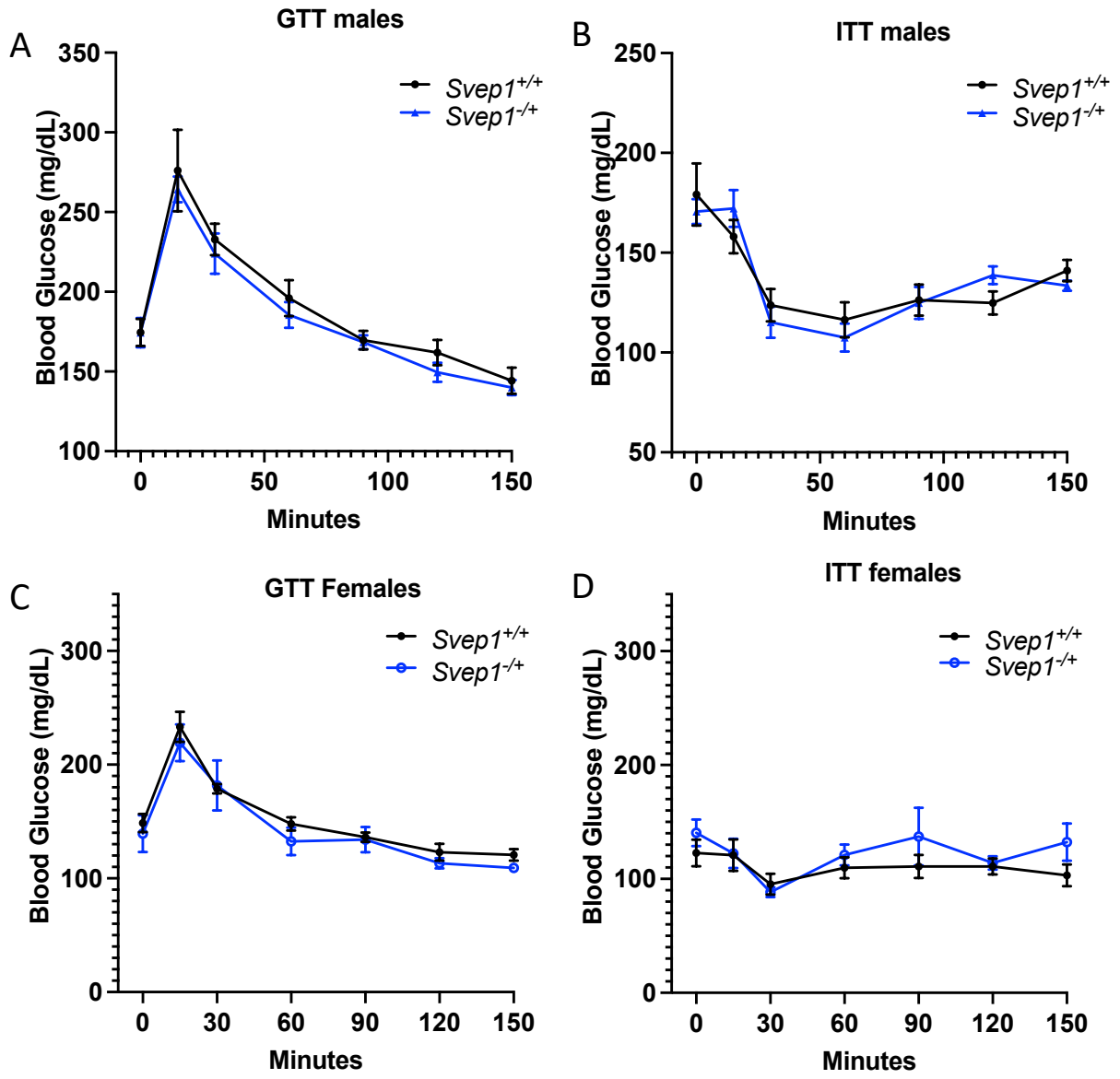


Figure 4.4 *Svep1* haploinsufficiency does not influence systemic response to glucose or insulin. (A-D) Blood glucose measurements of *Svep1*$^{+/+}$ and *Svep1*$^{-/+}$ mice after intraperitoneal glucose (A,C) or insulin (B,D) administration at 0 minutes. N = 5-8. Error bars represent SEM.

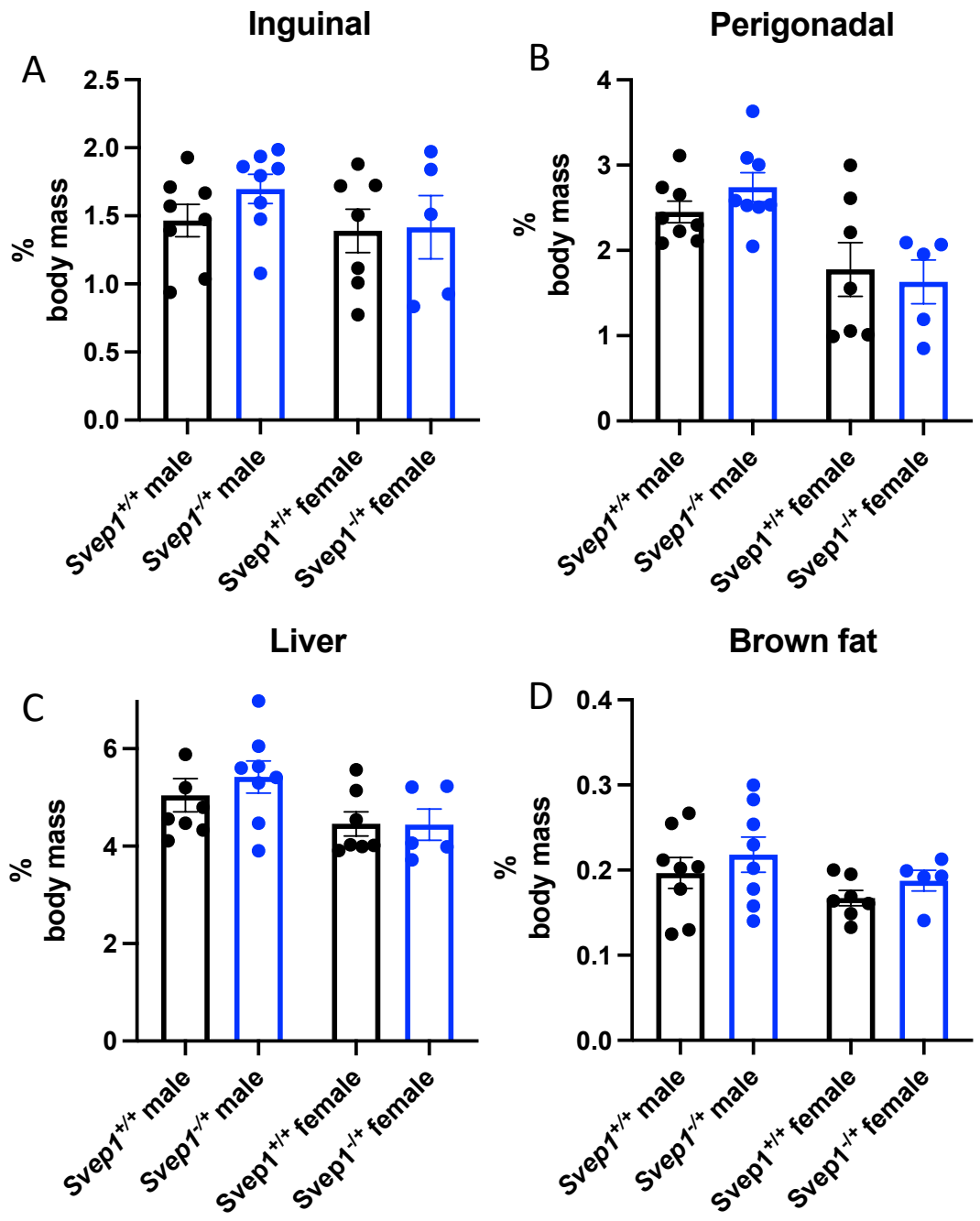


Figure 4.5 *Svep1* haploinsufficiency does not influence tissue lipid deposition.
(A-D) Dissected murine tissue mass measurements of inguinal adipose (A), perigonadal adipose (B), liver (C), and brown adipose (D), as a percentage of total body mass. N = 5-8. Error bars represent SEM.

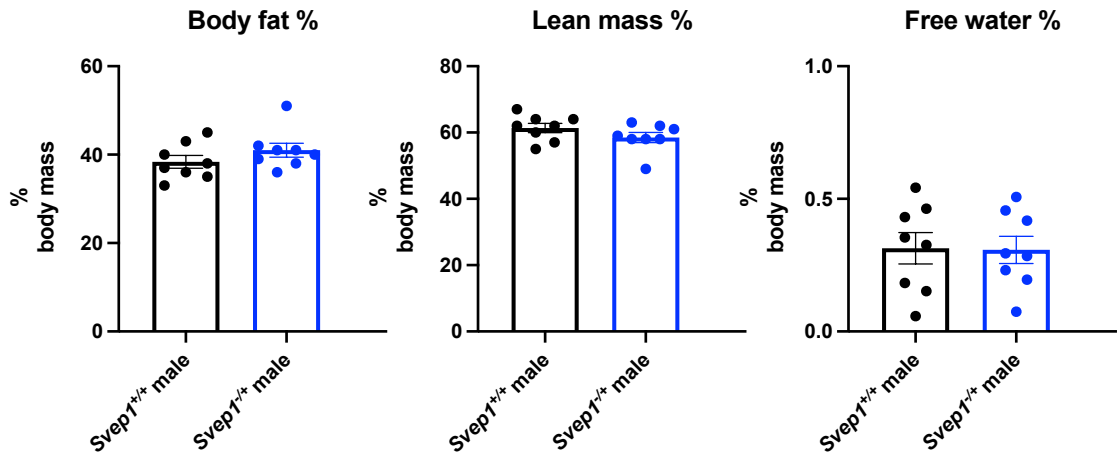


Figure 4.6 *Svep1* haploinsufficiency does not influence body composition.
(A-C) Fat mass (A), Lean mass (B), and free water (D) of *Svep1*$^{+/+}$ and *Svep1*$^{-/+}$ mice after 16 weeks of HFD feeding, as determined by EchoMRI™. N = 8. Error bars represent SEM.

### 4.2.4 Loss of *Svep1* in VSMCs is metabolically well-tolerated.

Given the observation that *Apoe*$^{-/-}$*;Myh11-CreER*$^{T2}$*;Svep1*$^{-/-}$ appeared to gain less weight than *Apoe*$^{-/-}$*;Myh11-CreER*$^{T2}$*;Svep1*$^{+/+}$ controls, we decided to test whether this was also observed in *Myh11-CreER*$^{T2}$*;Svep1*$^{-/-}$ mice, relative to littermate *Myh11-CreER*$^{T2}$*;Svep1*$^{+/+}$ controls. After 16 weeks of HFD feeding, we did not observe a significant difference in weight gain between the two genotypes of mice (Figure 4.7). We also did not appreciate a significant difference in the response of these mice to glucose or insulin, relative to controls (Figure 4.8).

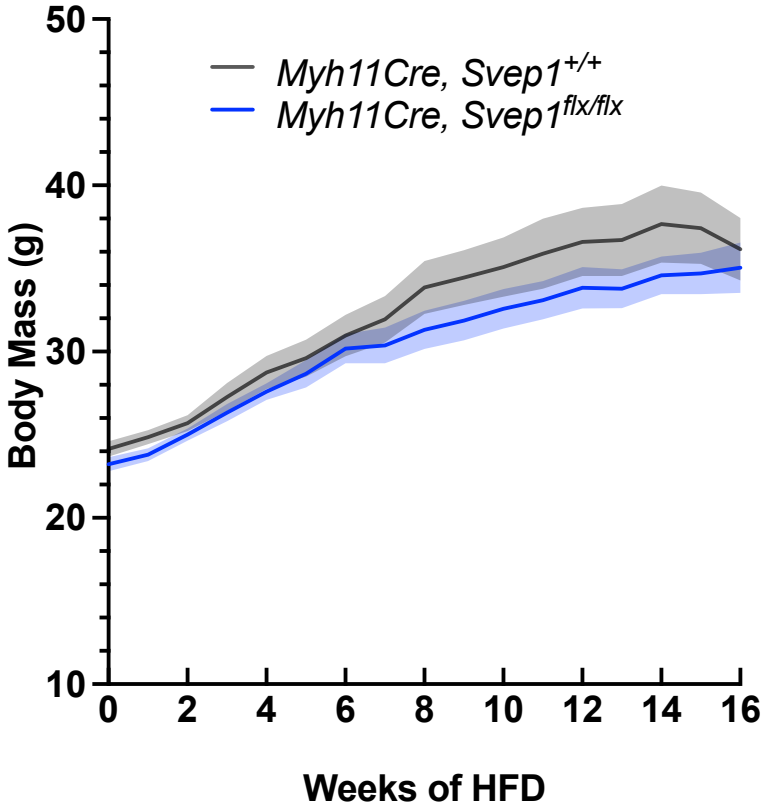


Figure 4.7 *Svep1* deficiency in VSMCs does not influence weight gain.
Weekly body mass measurements of *Myh11-CreER$^{T2}$;Svep1$^{+/+}$* and *Myh11-CreER$^{T2}$;Svep1$^{-/-}$* mice after 16 weeks of HFD feeding. N = 10-11. Shaded region represents SEM.

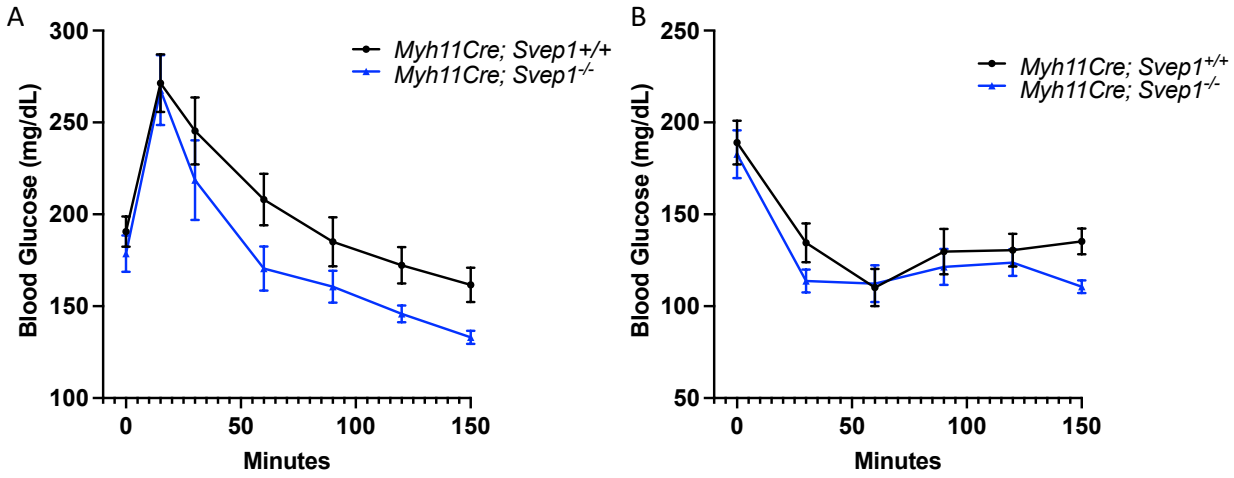


Figure 4.8 *Svep1* deficiency in VSMCs does not significantly influence glucose or insulin tolerance.
(A-B) Blood glucose measurements of *Myh11-CreER$^{T2}$;Svep1$^{+/+}$* and *Myh11-CreER$^{T2}$;Svep1$^{-/-}$* mice after intraperitoneal glucose (A) or insulin (B) administration at 0 minutes. N = 7-9. Error bars represent SEM.

.

### 4.2.5 Loss of *Itga9* in VSMCs is metabolically well-tolerated.

At the time of these studies, integrin α9β1 was the only protein known to interact with SVEP1. Based on this and the preliminary metabolic data regarding SVEP1-deficient mice, we sought to test the metabolic impact of depleting Itga9 in VSMCs. As with the SVEP1 depletion models, we did not appreciate significant differences after Itga9 depletion in VSMCs in weight gain after HFD feeding (Figure 4.9), response to glucose or insulin (Figure 4.10), or dissected tissue mass (Figure 4.11).

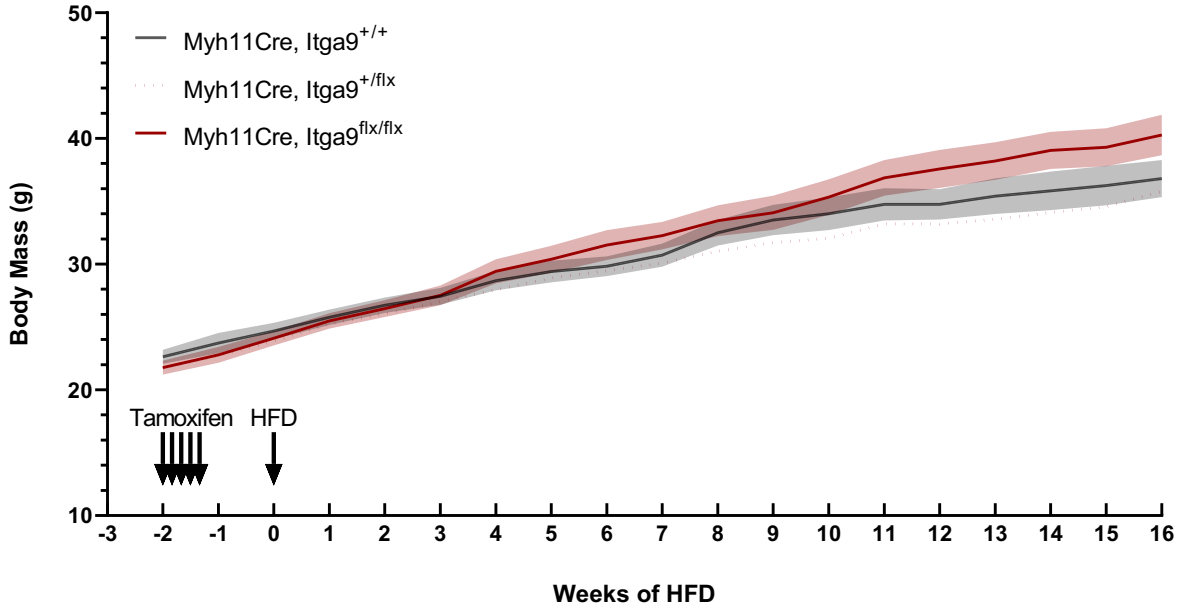


Figure 4.9 *Itga9* deficiency in VSMCs does not significantly influence weight gain. Weekly body mass measurements of *Myh11-CreER$^{T2}$;Itga9$^{+/+}$*, *Myh11-CreER$^{T2}$;Itga9$^{-/+}$* and *Myh11-CreER$^{T2}$;Itga9$^{-/-}$* mice after 16 weeks of HFD feeding. N = 12-14. Shaded region represents SEM.

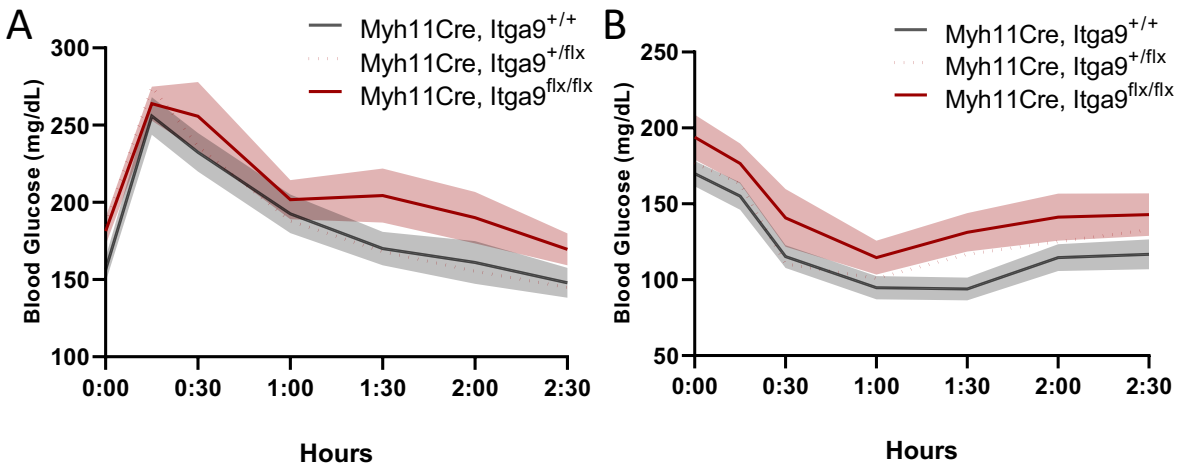


Figure 4.10 *Svep1* deficiency in VSMCs does not significantly influence glucose or insulin tolerance.
(A-B) Blood glucose measurements of *Myh11-CreER$^{T2}$;Itga9$^{+/+}$*, *Myh11-CreER$^{T2}$;Itga9$^{-/+}$* and *Myh11-CreER$^{T2}$;Itga9$^{-/-}$* mice after intraperitoneal glucose (A) or insulin (B) administration at 0 minutes. N = 12. Error bars represent SEM.

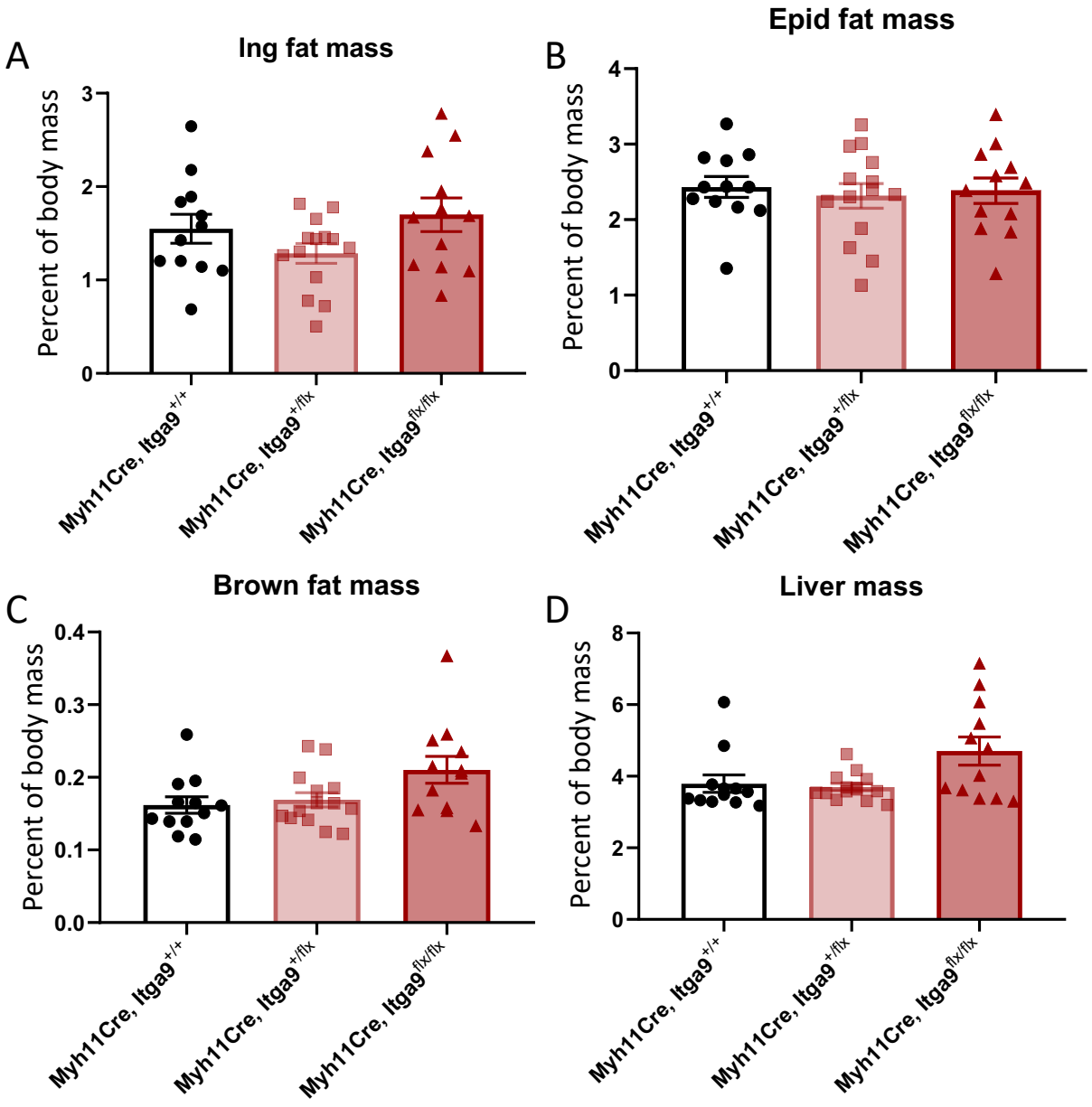


Figure 4.11 *Svep1* deficiency in VSMCs does not significantly influence tissue lipid distribution. (A-D) Dissected murine tissue mass measurements of inguinal adipose (A), perigonadal adipose (B), brown adipose (C), and liver (D), as a percentage of total body mass. N = 12-14. Error bars represent SEM.

### 4.2.6 Loss of *Svep1* in post-developmental mice is well-tolerated by the vasculature.

Given the association of SVEP1 with hypertension, we also tested the cardiovascular manifestations of *Svep1* deletion using the same mouse cohort described in section 4.2.2. Arterial catheterization was used to measure central blood pressure and heart rate in anesthetized mice. We did not appreciate significant differences between *Svep1*$^{+/+}$ and *Svep1*$^{-/-}$ mice in systolic or diastolic blood pressure or heart rate (Figure 4.12A-C). We further explored vascular function by titrating the *Svep1*$^{+/+}$ and *Svep1*$^{-/-}$ mice acutely with vaso-active compounds including phenylephrine, angiotensin II, acetylcholine, and sodium nitroprusside. Blood pressure was affected by the substances in a dose-dependent manner, and no significant differences were observed between *Svep1*$^{+/+}$ and *Svep1*$^{-/-}$ mice with any drug at any dose (Figure 4.12D-G). Similarly, no significant differences were observed between the two genotypes in vascular compliance of the ascending aorta or carotid artery, as determined using pressure-diameter measurements on dissected tissues (Figure 4.12H, I). These vascular phenotyping data support the metabolic phenotyping data and suggest the whole-body loss of SVEP1 is cardiometabolically well tolerated in adult mice.

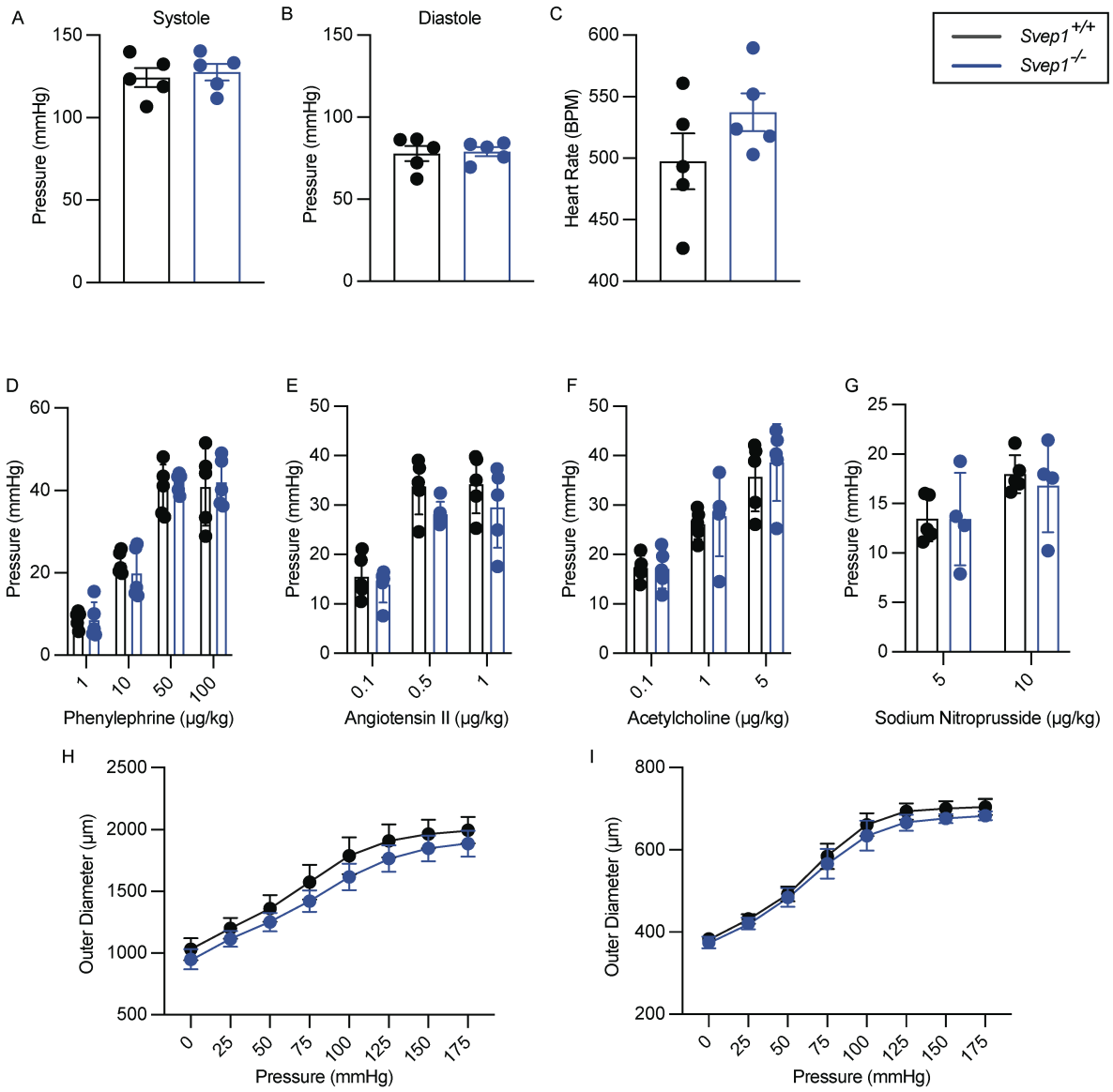


Figure 4.12 The effects of SVEP1 depletion on vascular function in mice.
(A) Systolic blood pressure of anesthetized *Svep1*$^{+/+}$ and *Svep1*$^{-/-}$ mice, as determined by arterial catheterization. (B) Diastolic blood pressure of anesthetized *Svep1*$^{+/+}$ and *Svep1*$^{-/-}$ mice. (C) Heart rate of anesthetized *Svep1*$^{+/+}$ and *Svep1*$^{-/-}$ mice. (D) Change in blood pressure upon venous phenylephrine administration in *Svep1*$^{+/+}$ and *Svep1*$^{-/-}$ mice. (E) Change in blood pressure upon venous angiotensin II administration in *Svep1*$^{+/+}$ and *Svep1*$^{-/-}$ mice. (F) Change in blood pressure upon venous acetylcholine administration in *Svep1*$^{+/+}$ and *Svep1*$^{-/-}$ mice. (G) Change in blood pressure upon venous sodium nitroprusside administration in *Svep1*$^{+/+}$ and *Svep1*$^{-/-}$ mice. N= 4-5. (H) Aortic compliance of the ex-vivo aortas from *Svep1*$^{+/+}$ and *Svep1*$^{-/-}$ mice as determined by pressure-diameter tracings. (G) Carotid artery compliance of the ex-vivo carotid arteries from *Svep1*$^{+/+}$ and *Svep1*$^{-/-}$ mice as determined by pressure-diameter tracings. N = 5 for all panels unless otherwise noted.

## 4.3 Discussion

Mendelian randomization and GWAS studies suggest that SVEP1 is causally related to T2D in humans (3, 6, 7). Preliminary results in mice supported this association and suggested that SVEP1 may protect against diabetes. This series of experiments described in this chapter were designed to rigorously test the hypothesis that SVEP1 promotes T2D in mice. We utilized a wide variety of murine SVEP1 depletion models, including mice lacking an SVEP1 allele from birth, whole body deletion of SVEP1 post-development, and deletion of SVEP1 and Itga9 in VSMCs. We did not appreciate significant differences between these mice and their littermate controls. This suggests that SVEP1 might not play a prominent role in systemic glucose metabolism in mice. We also tested the effects of deleting SVEP1 on blood pressure, vascular reactivity, and vascular compliance. As with the metabolic studies, we did not appreciate a vascular phenotype in mice lacking SVEP1.

Mouse models of cardiometabolic disease deviate from human disease in several important ways. As just one example, cardiometabolic disease generally manifests in humans after several decades of life. In contrast, mouse models are often studied in the first half of their total lifespan. Given the differences between mice and human pathogenesis, it is difficult to know how relevant these negative findings are to SVEP1's role in human biology. Nevertheless, these models suggest that loss of SVEP1 may be tolerated, which is an important consideration when evaluating SVEP1's potential to be targeted therapeutically.

## 4.4 Methods

### 4.4.1 Mice

The mice used in these experiments are described in chapters 2 and 5 of this dissertation. All mice used were bred into an *Apoe*$^{+/+}$ background prior to beginning the experiments. All mice were fed HFD beginning at 8 weeks of age.

### 4.4.2 Metabolic phenotyping

Mice were weighed and fasted prior to the metabolic challenge. For insulin tolerance tests (ITT), Humulin R (100 units/mL) was diluted 1:1000 in sterile PBS and injected intraperitoneally in mice at a dose of 0.75 units/kg. For glucose tolerance tests (GTT), a 10% or 20% glucose solution was prepared in sterile PBS and injected intraperitoneally at a final dose of 1 or 2g/kg. Tail vein glucose measurements were collected at 15–30-minute intervals using a glucometer. Mouse lean, fat, and total water mass were determined in male *Svep1*$^{+/+}$ and *Svep1*$^{-/-}$ mice fed HFD using EchoMRI (EchoMRI LLC). The EchoMRI was calibrated with canola oil. Measurements were gathered in duplicate for each mouse and averaged prior to analysis. Indirect calorimetry measurements were collected using the PhenoMaster System (TSE Systems) in collaboration with the Washington University Diabetes Research Center Diabetes Models Phenotyping Core. Mice fed HFD were placed in individual chambers and acclimated for several hours prior to data collection. Mice were fed HFD throughout the data collection. The measurements occurred at room temperature during standard 12-hour light/12-hour dark cycles.

### 4.4.3 Arterial blood pressure measurements

Central arterial blood pressure and heart rate were measured under inhaled 1.5% isoflurane anesthesia and while mice were maintained at 37°C using a heating pad and rectal thermometer, as done previously (159). Briefly, a midline incision was performed in the neck region; the thymus, muscle, and connective tissue were dissected away to isolate the right common carotid

artery. After tying it distally and clamping it proximally, an incision was made in the right common carotid artery through which a Millar pressure transducer (model SPR-1000, Houston, TX) was introduced, the clamp was removed, and the transducer advanced to the ascending aorta. Once instrumentation was complete, arterial blood pressure (systolic, diastolic, and mean) and heart rate were recorded via the PowerLab® data acquisition system (ADInstruments, Colorado Springs, CO). The average of a 3-minute period of stable recording was reported. Data were analyzed using LabChart® 8 for MAC software (ADInstruments).

To assess the blood pressure response to vasoactive agents, after baseline blood pressure measurement, dissection was performed to visualize the left internal jugular (IJ) vein as done previously (160). Once identified, a small incision was made and PE-10 tubing was introduced and kept in place with a 6-0 silk suture. While measuring arterial blood pressure, 50µL normal saline (NS) was injected via the IJ line as a bolus injection (1-2 seconds). After 2-3 minutes, baseline blood pressure was noted and increasing concentrations of either phenylephrine, angiotensin II, acetylcholine, or sodium nitroprusside (Sigma, St. Louis, MO) each in a ~10µL volume were injected in the IJ line and flushed with 40µL NS. After each drug, when blood pressure returned to baseline (2-3 minutes), the line was washed with 50µL NS for 3 minutes. The maximal change in blood pressure after each dose was reported. Mice were euthanized at the completion of the experiment.

### 4.4.4 Pressure myography

Following blood pressure measurement and euthanasia, ascending aorta and left common carotid artery were excised and placed in physiologic saline solution (PSS) composed of 130mM NaCl, 4.7mM KCl, 1.6mM $CaCl_2$, 1.18mM $MgSO_4$-$7H_2O$, 1.17mM $KH_2PO_4$, 14.8mM $NaHCO_3$, 5.5mM dextrose, and 0.026mM Ethylenediaminetetraacetic acid (EDTA, pH 7.4) overnight at

4°C. Vessels were cleaned of surrounding fat, mounted on a pressure arteriograph (Danish Myo Technology) and maintained in PSS at 37°C. Vessels were visualized with an inverted microscope connected to a CCD camera and a computerized system, which allows continuous recording of vessel diameter. Intravascular pressure was increased from 0 to 175 mmHg by 25-mmHg increments, the vessel outer diameter was recorded at each step (12 seconds per step). The average of three measurements at each pressure was reported.

# Chapter 5

# SVEP1 signals through the orphan receptor PEAR1 to promote vascular disease associated signaling and platelet reactivity[3]

## 5.1 Abstract

Sushi, von Willebrand factor type A, EGF and pentraxin domain containing 1 (SVEP1) is an extracellular matrix protein that causally promotes vascular disease and associates with platelet reactivity in humans. Here, we identify a disease-relevant and potentially targetable interaction between SVEP1 and the orphan receptor Platelet and Endothelial Aggregation Receptor 1 (PEAR1). This interaction promotes PEAR1 phosphorylation and disease associated AKT/mTOR signaling in vascular cells and platelets. Mice lacking SVEP1 have reduced platelet activation, and exogenous SVEP1 induces PEAR1-dependent activation of platelets. SVEP1 and PEAR1 causally and concordantly relate to platelet phenotypes and cardiovascular disease in humans. Targeting this novel interaction may be a viable therapeutic strategy to treat or prevent cardiovascular and thrombotic disease.

[3] Chapter 5 was modified and later licensed under a Creative Commons Attribution 4.0 International License by Nature Springer

https://creativecommons.org/licenses/by/4.0/

https://www.nature.com/articles/s41467-023-36486-0

Creators include: Jared S. Elenbaas, Upasana Pudupakkam, Katrina J. Ashworth, Chul Joo Kang, Ved Patel, Katherine Santana, In-Hyuk Jung, Paul C. Lee, Kendall H. Burks, Junedh M. Amrute, Robert P. Mecham, Carmen M. Halabi, Arturo Alisio, Jorge Di Paola & Nathan O. Stitziel

## 5.2 Introduction

Sushi, von Willebrand factor type A, EGF and pentraxin domain containing 1 (SVEP1) is a poorly characterized extracellular matrix (ECM) glycoprotein (1, 5) with a striking number of human disease associations. We became interested in SVEP1 upon finding a coding variant in the gene (p.D2702G) that associated with risk of coronary artery disease (CAD) (Figure 5.1A). We then sought to elucidate the disease mechanisms of the protein and evaluate the prospect of targeting it pharmacologically (6). The role of SVEP1 in the promotion of atherosclerosis was confirmed using mouse models, but its mechanisms of action remained elusive (3). In addition to CAD, genetic variation within the locus containing *SVEP1* is associated with hypertension (6), type 2 diabetes (6), altered outcomes in septic shock (21), and glaucoma (11, 12, 27). Recent studies utilizing aptamer-based multiplex protein assay plasma proteomics (SomaScan) (4) have identified additional associations of SVEP1 with human traits and diseases including pulmonary artery hypertension (161), heart failure (64), and longevity (14, 17). Combining genomics and plasma proteomics enables causal analysis of SVEP1's role in disease using Mendelian Randomization (MR). MR of plasma SVEP1 levels has revealed causal, positive associations of SVEP1 with CAD (3), hypertension (3), type 2 diabetes (3, 7), and dementia (13). Collectively, these data strongly support a deleterious role of increased SVEP1 protein levels in human aging-related disease.

In addition to its associations with chronic disease, a recent genome-wide association study (GWAS) of platelet reactivity identified an association between a coding variant within SVEP1 (SVEP1 p.R229G, Figure 5.1A) and platelet aggregation in response to adenosine diphosphate-stimulation (ADP) (18). The strongest genetic association with ADP-stimulated platelet aggregation in the same GWAS was an intronic variant of *Platelet and Endothelial Cell Receptor 1* (*PEAR1*), a gene coding for a cell-surface receptor expressed by platelets and various vascular

cells, among others (49). Numerous additional human studies have implicated PEAR1 in platelet aggregation (162-168), as well as CAD and related outcomes (162, 169-171).

PEAR1 shares many features with the receptor tyrosine kinase (RTK) family, such as dimerization, kinase activity, and likely glycosylation (49, 172); however, the PEAR1 dimer is phosphorylated by a Src family kinase (SFK) (49, 50) instead of through cross-phosphorylation (173). Antibodies that bind to the extracellular domain (ECD) of PEAR1 (PEAR1ECD) are capable of dimerizing and activating the protein, leading to its association with p85 PI3K and activation of AKT. It is speculated that PEAR1 may be a platelet binding partner (49, 50) or proteoglycan receptor (174), but its function in platelets remains poorly understood. PEAR1 also contributes to neoangiogenesis in endothelial cells (48) and glial engulfment (175-177).

Despite the numerous disease associations of SVEP1 and PEAR1, critical gaps remain in our understanding of the molecular mechanisms of these proteins. For example, the physiological ligand of PEAR1 has yet to be identified despite previous attempts to address this critical question (172, 178-180). Defining the disease mechanisms of SVEP1 and PEAR1 will further our understanding of pathophysiology and may generate novel approaches to treat and prevent disease. Here, we use human multi-omics, animal models, and cellular and molecular assays to identify SVEP1 as a PEAR1 ligand, characterize their interaction, and assess the therapeutic potential of blocking these proteins.

# 5.3 Results

## 5.3.1 Plasma SVEP1 concentration is altered by PEAR1

We first sought to identify candidate SVEP1 interactions using human genomics and aptamer-based plasma proteomics from the INTERVAL study of healthy volunteers (4). Genetic variation within the locus containing *SVEP1* on chromosome 9 influences plasma levels of SVEP1; these

cis-protein quantitative trait loci (cis-pQTL) have been described previously (3). Strikingly, genetic variation on chromosome 1 (a trans-protein quantitative trait locus, or trans-pQTL) also associates with altered plasma SVEP1 concentrations at a genome-wide level of significance. The trans pQTL variant most strongly associated with altered plasma SVEP1 concentration (rs145662369) is an intronic single nucleotide polymorphism (SNP) within the locus containing *PEAR1*. rs145662369 is not associated with altered expression of *PEAR1* in the Genotype-Tissue Expression database (GTEx); however, it is in perfect linkage disequilibrium ($r^2$=1) with rs147639000. rs147639000 is a missense polymorphism within an EGF-like domain of PEAR1's ectodomain (Figure 5.1B, p.D343N), and the minor allele (Asparagine at 343) is significantly associated with increased levels of plasma SVEP1 ($P = 6.5x10^{-16}$, Figure 5.1C, 5.2A,B). Plasma PEAR1 concentration is minimally altered in individuals harboring the PEAR1 D343N variant (P = 0.03, Figure 5.1D). A proteome-wide association analysis of PEAR1 D343N demonstrates that its impact on plasma protein is specific to SVEP1 among proteins measured by SomaScan (Figure 5.1E).

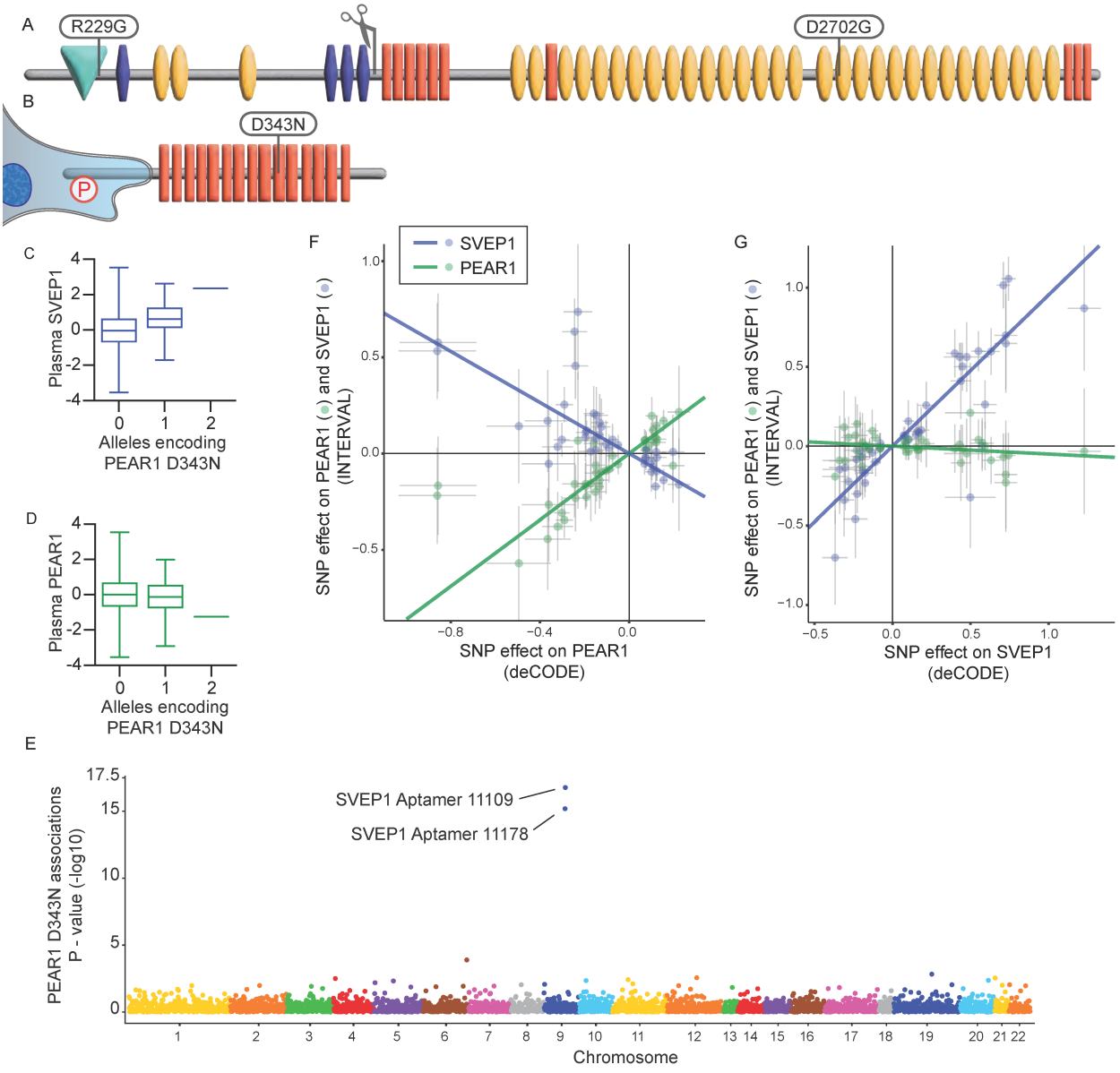


Figure 5.1 PEAR1 alters plasma levels of SVEP1.

(A,B) Schematic of SVEP1 (A) and PEAR1 (B) proteins. Domains were identified using the Simple Modular Architecture Research Tool (SMART) (181). Teal, von Willebrand factor type A domain; purple, putative ephrin-receptor like; yellow, complement control protein/SUSHI repeat; orange, epidermal growth factor (EGF)-like domain or calcium-binding EGF-like domain or laminin-type EGF-like domain; scissors, putative cleavage site (76); P, representative phosphorylation of the PEAR1 intracellular domain. Protein coding variants of interest are denoted at the corresponding peptide. (C) Plasma SVEP1 (aptamer 11109.56.3) box and whisker plot as a function of allelic copies of rs147639000 (PEAR1 p.D343N) in the INTERVAL database. Beta = 0.67, P = $6.5 \times 10^{-16}$. (D) Plasma PEAR1 (aptamer 8275.31.3) box and whisker plot as a function of allelic copies of rs147639000 (PEAR1 p.D343N) in the INTERVAL database. Beta = -0.18, P = 0.03. (E) Manhattan plot of associations between PEAR1 D343N and plasma proteins measured in INTERVAL. Each point represents the genomic location of the

gene coding for a measured protein. (F) Two-sample MR of estimated SNP effects (with 95% confidence intervals) on PEAR1 in deCODE (x-axis) and either PEAR1, green, or SVEP1, blue, in INTERVAL (y-axis). The causal estimate is designated by a line of the corresponding color. PEAR1 Beta = 0.86, P = $2.4 \times 10^{-37}$; SVEP1 Beta = -0.66, P = $3.5 \times 10^{-20}$. (G) Two-sample MR of estimated SNP effects (with 95% confidence intervals) on SVEP1 in deCODE (x-axis) and either PEAR1, green, or SVEP1, blue, in INTERVAL (y-axis). The causal estimate is designated by a line of the corresponding color. PEAR1 Beta = -0.07, P = 0.002; SVEP1 Beta = 0.84, P = $2.5 \times 10^{-54}$.

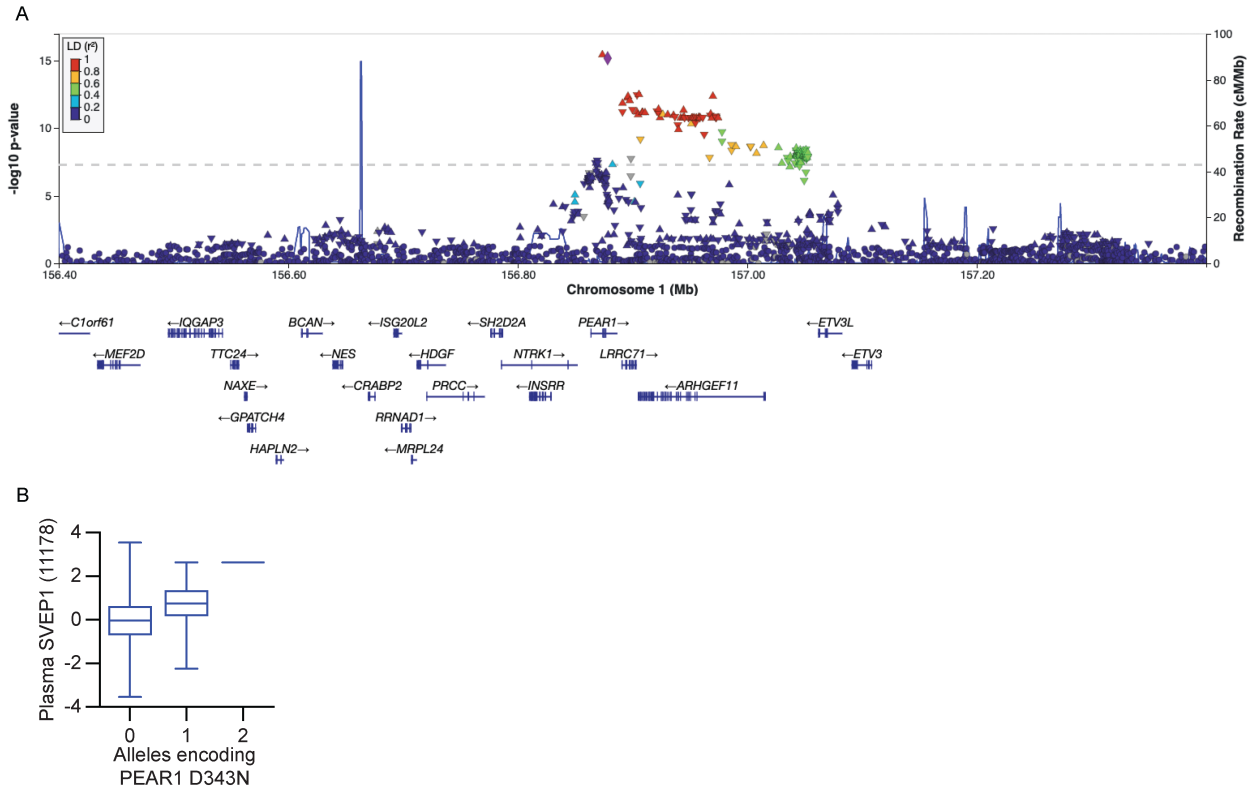


Figure 5.2 PEAR1 alters plasma levels of SVEP1, continued.
(A) LocusZoom (182) of the genetic locus containing PEAR1 and associations with altered plasma SVEP1 (aptamer 11109.56.3) from the INTERVAL database. Linkage disequilibrium with rs14763900 (purple diamond) is indicated. (B) Plasma SVEP1 (aptamer 11178.21.3) box and whisker plot as a function of allelic copies of rs147639000 (PEAR1 p.D343N) in the INTERVAL database. Beta = 0.70, P = $1.7 \times 10^{-17}$.

Given the impact of the PEAR1 D343N variant on plasma SVEP1 concentration and expression of PEAR1 on vascular endothelial cells (48), we hypothesized that PEAR1 binds and sequesters circulating SVEP1 from human plasma. To test this hypothesis, we asked whether genetic variation within the *PEAR1* locus that influences plasma PEAR1 concentrations also impacts plasma SVEP1 concentrations. To avoid potential sources of confounding in a one-sample MR, we generated a genetic instrument for plasma PEAR1 and SVEP1 levels using the recently published data from deCODE, a dataset of plasma protein levels measured by SomaScan in 35,559 Icelanders (64). Using the instruments generated from deCODE, we asked if the genetically determined plasma levels of these proteins were associated with plasma protein levels from INTERVAL. Both instruments were able to accurately predict plasma concentrations of their respective proteins (PEAR1 $P = 2.4x10^{-37}$, Figure 5.1F; SVEP1 $P = 2.5x10^{-54}$, Figure 5.1G), supporting the approach. Genetically encoded changes in plasma PEAR1 concentration were inversely related to plasma SVEP1 ($P = 3.5x10^{-20}$, Figure 5.1F). As expected, plasma concentrations of PEAR1 were minimally impacted by genetically encoded changes in plasma SVEP1 levels (P = 0.002, Figure 5.1G).

We then asked whether SVEP1 and PEAR1 physically interact using molecular assays. The extracellular domain (ECD) of PEAR1 (PEAR1ECD) co-immunoprecipitates with recombinant, Myc-tagged SVEP1 in pulldown assays (Figure 5.3A). An alternative PEAR1ECD construct containing a biotin tag also coimmunoprecipitates with SVEP1 (Figure 5.4A). Reciprocally, SVEP1 coimmunoprecipitates with the PEAR1ECD (Figure 5.3B). These molecular assays and MR analyses suggest SVEP1 and PEAR1 physically

interact.

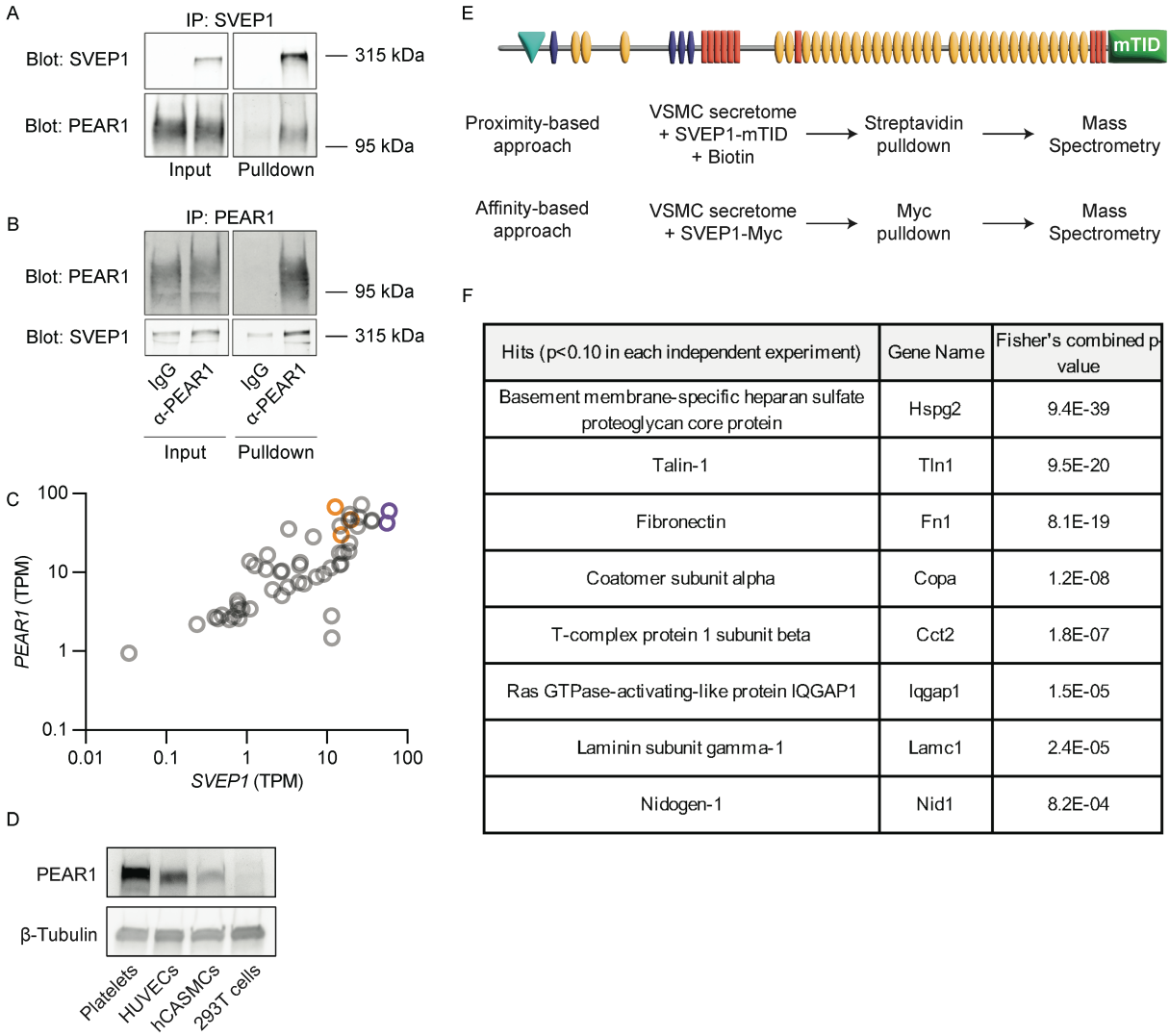


| Hits (p<0.10 in each independent experiment) | Gene Name | Fisher's combined p-value |
|---|---|---|
| Basement membrane-specific heparan sulfate proteoglycan core protein | Hspg2 | 9.4E-39 |
| Talin-1 | Tln1 | 9.5E-20 |
| Fibronectin | Fn1 | 8.1E-19 |
| Coatomer subunit alpha | Copa | 1.2E-08 |
| T-complex protein 1 subunit beta | Cct2 | 1.8E-07 |
| Ras GTPase-activating-like protein IQGAP1 | Iqgap1 | 1.5E-05 |
| Laminin subunit gamma-1 | Lamc1 | 2.4E-05 |
| Nidogen-1 | Nid1 | 8.2E-04 |

Figure 5.3 SVEP1 and PEAR1 physically interact and colocalize in tissue.
(A,B) Immunoblots of the indicated proteins after co-immunoprecipitation. Negative controls included no SVEP1 (A), or non-specific IgG (B). Additional details listed in Methods. (C) Expression of *PEAR1* and *SVEP1* in transcripts per million (TPM) in tissues from the GTEx database. Purple circles designate adipose tissues. Orange circles designate arterial tissues. Pearson r correlation = 0.74, P <0.0001. (D) Immunoblot analysis of PEAR1 levels using cell lysates from the indicated cell-type. β-Tubulin served as a loading control. (E) Schematic of proximity or affinity-based proteomics experiments. (F) List of proteins enriched in experiments represented in (E). Hits were identified as those proteins enriched at a confidence level of P <0.10 in each experiment. Fisher's combined p-value is a meta-analysis of the four experiments. Additional details listed in

Methods.

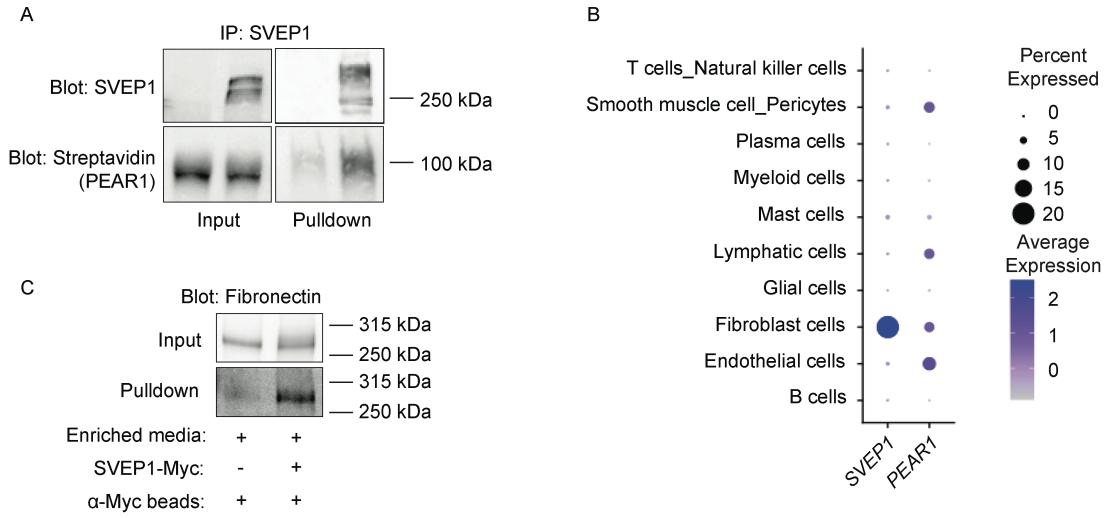


Figure 5.4 SVEP1 and PEAR1 physically interact and colocalize in tissue, continued. (A) Immunoblots of the indicated proteins after co-immunoprecipitation. Biotinylated PEAR1 was detected using a fluorescent streptavidin probe. The control sample did not contain SVEP1. Additional details listed in Methods. (B) *SVEP1* and *PEAR1* expression in single cell populations of human coronary arteries from publicly available data (183). (C) Immunoblots of Fibronectin from enriched VSMC media after co-immunoprecipitation of SVEP1 with α-Myc beads.

### 5.3.2 SVEP1 and PEAR1 are co-expressed in human tissues

SVEP1 circulates in human plasma, but the protein is thought to primarily reside within the ECM of the tissues where it is produced, similar to other ECM proteins (184). PEAR1 also acts locally as a receptor that signals intracellularly. We therefore sought to identify tissues that may harbor a

biologically relevant interaction between SVEP1 and PEAR1 by determining which tissues co-express their transcripts. The expression of *SVEP1* and *PEAR1* is highly correlated among tissues in GTEx (Figure 5.3C) and several tissues express high levels of both genes. For example, arterial and adipose tissues (orange and purple, respectively) express *SVEP1* and *PEAR1* and are particularly relevant to cardiometabolic disease. Bone marrow is not among the tissues analyzed in GTEx; however, other sources of expression data indicate high expression of *SVEP1* and *PEAR1* within this tissue (185). Single-cell RNA analysis of coronary arteries (183), the site of atherosclerosis that can lead to myocardial infarction, reveals that *SVEP1* is expressed predominantly by fibroblasts (Figure 5.4B), although studies in mice suggest that VSMCs may also express *Svep1* under pathological conditions (3). *PEAR1* is expressed by a variety of disease-relevant cell-types within coronary arteries, including fibroblasts, smooth muscle cells, and endothelial cells (Figure 5.5B). To assess protein expression of PEAR1, we collected platelet lysates from freshly isolated human platelets and cultured primary human umbilical vein endothelial cells (HUVECs), primary human coronary artery smooth muscle cells (hCASMCs), and 293T cells. Immunoblot assays for PEAR1 revealed that platelets, HUVECs, and hCASMCs express the protein. In contrast, 293T cells do not express an appreciable amount of PEAR1 (Figure 5.4D).

Receptors on the surface of cells interact with the ECM and influence cell behavior. The ECM is heterogenous and differences in its composition result in disparate effects on cells. Although SVEP1 is a canonical component of the ECM, antibodies that reliably recognize SVEP1 in situ have not been successfully developed; therefore, little is known about how and where SVEP1 may integrate into the ECM or which cell types it may influence. We used a combination of affinity and proximity-based experimental approaches to address this question. The bait proteins

for these experiments included recombinant SVEP1 fused to a Myc-tag or mini-Turbo ID (mTID), a promiscuous biotin ligase (186). The prey proteins were derived from enriched media from murine VSMCs (Figure 5.4E), a rich source of diverse ECM proteins. Two independent experiments were performed using each approach and a reproducibility criterion of $P < 0.10$ for enrichment was applied across all experimental data. In addition to SVEP1, a total of 8 proteins fulfilled this criterion (Figure 5.4F), including Basement membrane-specific heparan sulfate proteoglycan core protein (HSPG2, also known as Perlecan), Fibronectin, Laminin subunit gamma-1, and Nidogen-1. Pulldown of Fibronectin by SVEP1 was confirmed using coimmunoprecipitation assays (Figure 5.5C). Together, these proteins comprise the major non-collagen basement membrane components (187). This suggests SVEP1 may be integrated with the basement membrane where it could interact with numerous PEAR1-expressing cells.

### 5.3.3 SVEP1 signals through PEAR1 to activate AKT signaling

PEAR1 is phosphorylated by SFK upon its activation (49, 50). To test if SVEP1 can induce PEAR1 activation and phosphorylation, we exposed platelets to immobilized bovine serum albumin (BSA, a nonspecific negative control protein), immobilized SVEP1, or soluble PEAR1 polyclonal antibody (pAb, a positive control) (50, 172). Immunoblot assays revealed a robust phospho-tyrosine signal corresponding to 140kDa, the expected mass of PEAR1, after pulling down PEAR1 from lysates of cells exposed to SVEP1 and PEAR1 pAb but not BSA (Figure 5.5A); this result is consistent with activation of PEAR1 by SVEP1 (49). We then tested activation of downstream AKT signaling by probing the platelet lysates for phosphorylated AKT (pAKT) (50). Consistent with PEAR1 activation, both SVEP1 and PEAR1 pAb induced AKT phosphorylation in platelets, but BSA did not (Figure 5.5B). We then tested the response of PEAR1-expressing HUVECs and hCASMCs (Figure 5.3B) to SVEP1 using similar techniques.

Serum-containing media was used in these signaling assays as a PEAR1-independent, positive control for AKT signaling. AKT signaling was activated upon exposure to SVEP1, PEAR1 pAb, and serum-containing media in both cell types (Figure 5.5C,D), relative to BSA controls. Neither SVEP1 nor PEAR1 pAb activated AKT in 293T cells, which lack PEAR1 (Figure 5.5E). Serum did activate AKT signaling in 293T cells however, suggesting the AKT signaling axis was uncompromised in these cells. Reconstitution of PEAR1 in 293T cells by transfection of a *PEAR1*-expression plasmid resulted in constitutive AKT activation, such that SVEP1, PEAR1 pAb, and serum had no additional effect on pAKT levels in these cells (Figure 5.6A). Together, these findings are consistent with the hypothesis that SVEP1 signals through PEAR1 to activate AKT. To directly test this hypothesis, we performed transient PEAR1 knockdown in hCASMCs using small-interfering ribonucleic acid (siRNA), since hCASMCs express PEAR1 and are readily transfectable with siRNA. Cells treated with *PEAR1* siRNA had diminished PEAR1 protein levels compared to negative controls (Figure 5.5F, 5.6B) and were unable to activate AKT upon exposure to SVEP1 and PEAR1 pAb. Serum-containing media was able to activate AKT signaling regardless of siRNA treatment however, demonstrating an intact AKT signaling axis. These data demonstrate that SVEP1-induced AKT signaling is dependent on PEAR1.

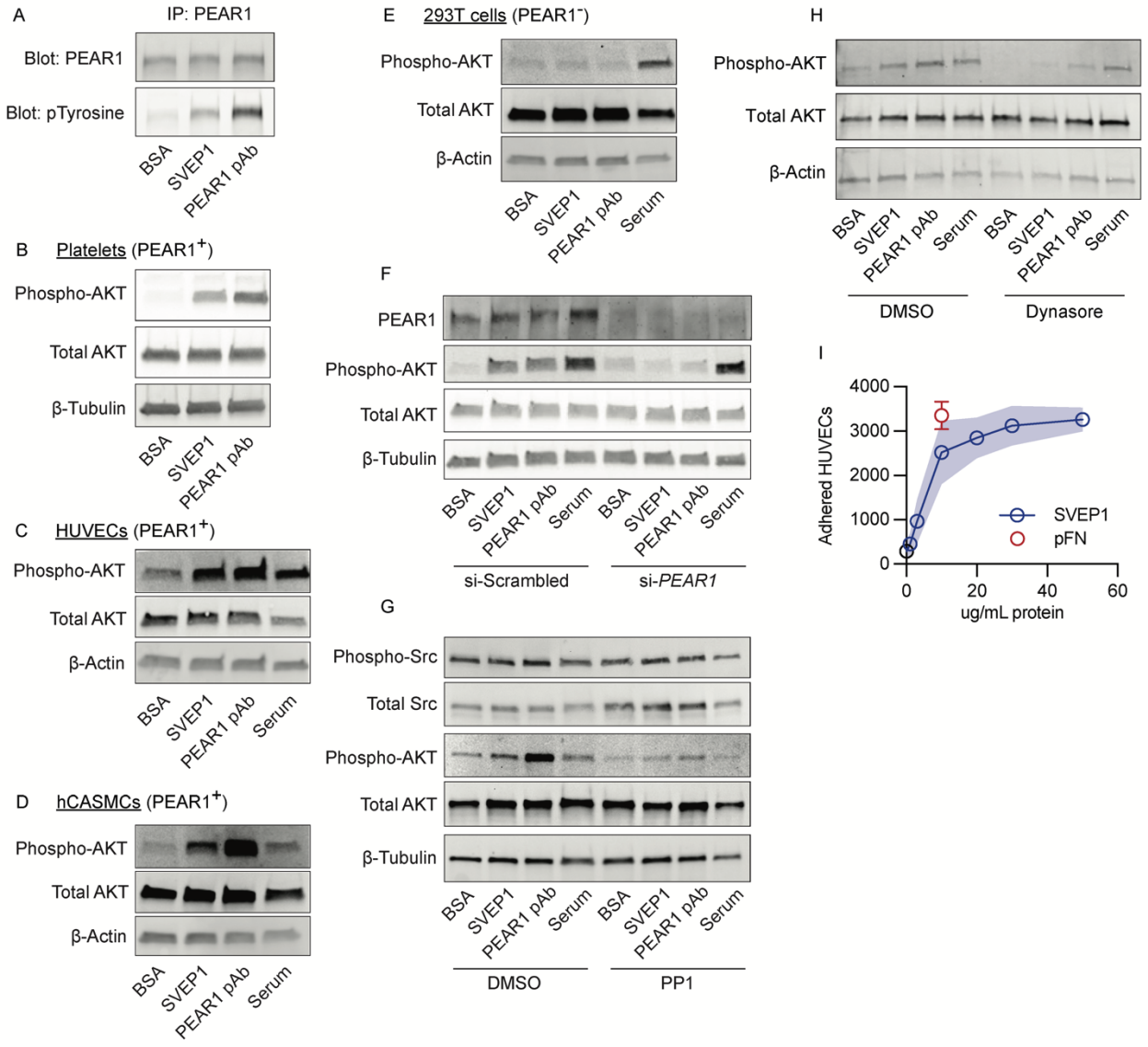


Figure 5.5 SVEP1 activates AKT signaling through PEAR1.
(A) Isolated human platelets were exposed to immobilized BSA, SVEP1, or soluble PEAR1pAb for 15 minutes prior to lysis. Lysates were subjected to immunoprecipitation with an anti-PEAR1 antibody and analyzed by immunoblot assays for PEAR1 and pTyrosine. The pTyrosine signal directly overlapped with the PEAR1 signal at approximately 140kDa. (B) Platelets were exposed to stimuli as described in (A). Lysates were analyzed by immunoblot assays for the indicated proteins. (C, D, E) HUVECs (C), hCASMCs (D), and 293T cells (E) were exposed to stimuli before lysis and analysis by immunoblot assays for the indicated proteins. (F) hCASMCs were transfected with scrambled siRNA or anti-*PEAR1* siRNA prior to exposure to the listed stimuli. Lysates were analyzed by immunoblot assays for the indicated proteins. (G, H) HUVECs were pretreated with DMSO (carrier), PP1 (SFK inhibitor, G), or Dynasore (dynamin inhibitor, H) prior to exposure to the listed stimuli. Lysates were analyzed by immunoblot assays for the

indicated proteins. (I) Adherence of HUVECs to increased concentrations of SVEP1 or pFN. Wells were precoated with the indicated protein and blocked with BSA prior to assay. Error bars represent 95% confidence intervals.

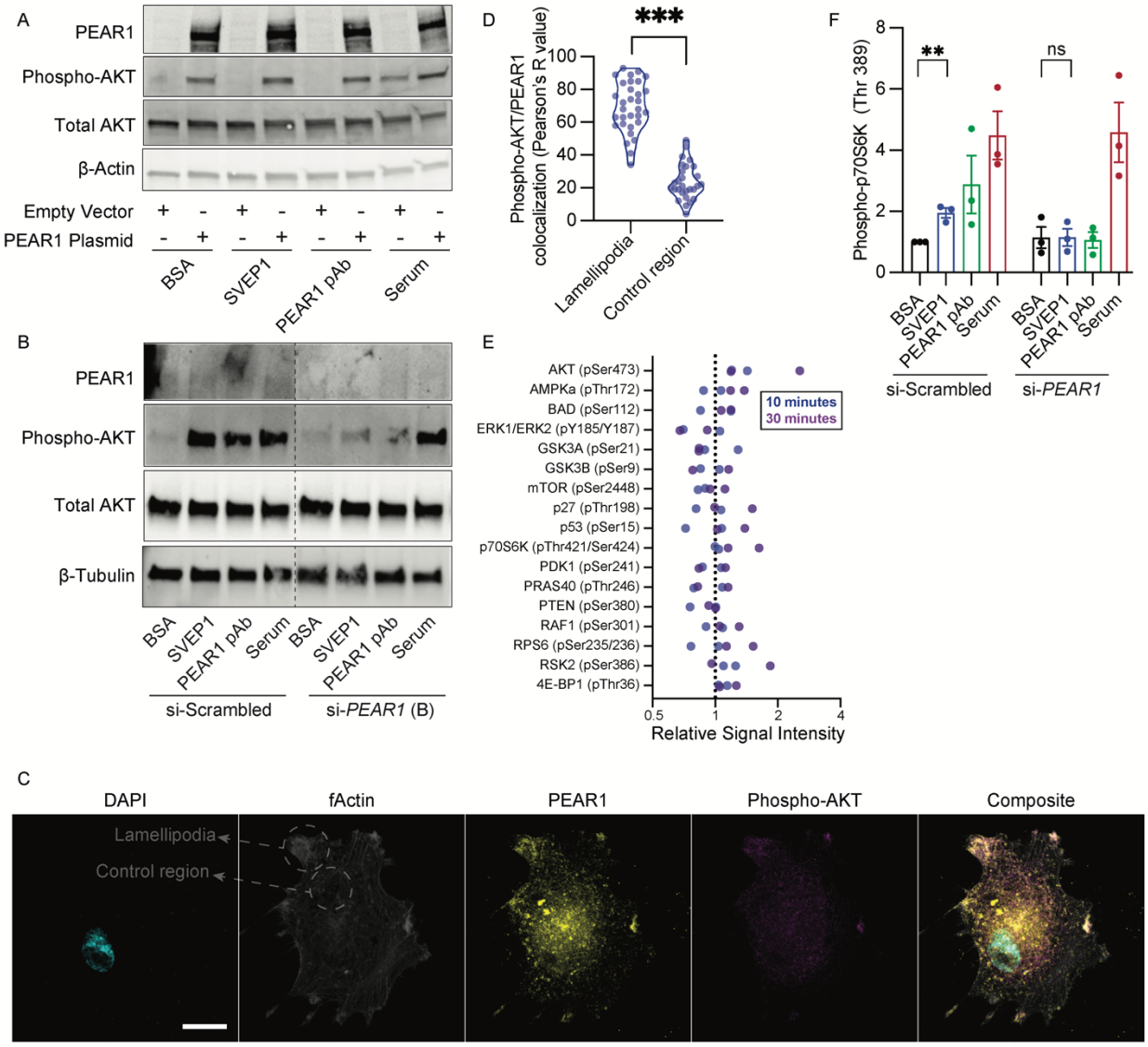


Figure 5.6 SVEP1 activates AKT signaling through PEAR1, continued.
(A) 293T cells were transfected with empty vector or a PEAR1-expression plasmid prior to exposure to the listed stimuli. Lysates were analyzed by immunoblot assays for the indicated proteins. (B) hCASMCs were transfected with scrambled siRNA or anti-*PEAR1* siRNA (construct B) prior to exposure to the listed stimuli. Lysates were analyzed by immunoblot assays for the indicated proteins. (C) Images of HUVECs seeded on immobilized SVEP1 for 60 minutes. Scale bar = 20μm. (D) Quantification of PEAR1 and pAKT colocalization in (C), as determined by the Pearson correlation coefficient. Lamellipodia were identified as bundles of fActin on the periphery of cells. Cellular regions not containing lamellipodia were used as control regions. N = 28-31, $P < 0.0001$, unpaired t test. (E) Densitometry quantification of the

listed phospho-protein using a phospho-array of HUVEC lysates from cells exposed to immobilized SVEP1 relative to BSA for 10 or 30 minutes. (F) Densitometry quantification of three independent experiments, represented in Figure 5.7D. Data are normalized to si-Scrambled, BSA conditions and represent the ratio of phospho-p70S6K (Thr 289) to total p70S6K. $P < 0.01$, unpaired t test.

Activation of AKT signaling by PEAR1 is SFK-dependent (50). To test whether SVEP1-induced AKT signaling was also dependent on SFK, we pretreated HUVECs with the SFK inhibitor PP1 or carrier dimethylsulfoxide (DMSO) prior to BSA, SVEP1, PEAR1 pAb, or serum exposure. As expected, PP1 abrogated the ability of SVEP1 and PEAR1 pAb to activate AKT signaling in HUVECs (Figure 5.5G). PEAR1 signaling is also thought to depend on its internalization through a clathrin-dependent mechanism (176, 188). To test whether SVEP1-induced AKT signaling was also dependent on this process, we treated cells with the dynamin inhibitor Dynasore (189) or carrier DMSO prior to exposure to the stimuli. HUVECs pretreated with DMSO exhibited increased pAKT upon exposure to SVEP1, PEAR1 pAb, and serum; however, the effects of SVEP1 and PEAR1 pAb were abrogated by Dynasore pretreatment (Figure 5.5H). These data demonstrate that the effects of SVEP1 on pAKT are dependent on SFK and endocytosis, consistent with canonical PEAR1 signaling.

SVEP1's most recognized cellular function is to promote cell adhesion (76). To test whether PEAR1-expressing HUVECs were able to adhere to SVEP1, we seeded the cells on tissue-culture plates coated with increasing concentrations of SVEP1 or plasma Fibronectin, a positive control, and blocked with BSA. After a brief incubation the non-adhered cells were removed by centrifugation and adhered cells were counted using automated microscopy. HUVECs adhered to SVEP1 in a dose-dependent manner up to 20μg/mL SVEP1 (Figure 5.5I).

### 5.3.4 PEAR1 and pAKT colocalize to lamellipodia of cells grown on SVEP1

Previous studies have reported that PEAR1 is localized to the filopodia and lamellipodia of cultured cells (48). These cellular structures are generated by actin polymerization and are sites of membrane protrusion and ECM adhesion (190). To test whether SVEP1 activates pAKT at regions of PEAR1 localization, we seeded hCASMCs and HUVECs on SVEP1 and stained for filamentous actin (fActin), PEAR1, and pAKT. Cells were imaged using fluorescent confocal microscopy and filopodia and lamellipodia were identified as bundles of fActin on the perimeter of the cells (190). hCASMCs treated with scrambled siRNA exhibited high colocalization of PEAR1 and pAKT on lamellipodia and lower colocalization within the cell body, a negative control region (Figure 5.7A, B). Similar colocalization was observed in HUVECs (Figure 5.6C, D). Knockdown of PEAR1 using siRNA diminished the colocalization in filopodia and lamellipodia (Figure 5.7A, B). Together these data suggest that PEAR1 on the surface of lamellipodia and filopodia activates pAKT locally when cells encounter immobilized SVEP1.

### 5.3.5 SVEP1 and PEAR1 activate downstream mTOR signaling

AKT is a central regulator of numerous signaling pathways; however, little is known about which pathways downstream of AKT are activated by PEAR1. We screened for AKT-related pathways that may be influenced by SVEP1/PEAR1 signaling using an AKT pathway phospho-array. Given the temporal nature of kinase activation, we exposed HUVECs to BSA or SVEP1 for either 10 or 30 minutes before lysing the cells and assessing pathway activation. Elevated pAKT was observed in cells exposed to SVEP1 in each experiment (Figure 5.6E), validating the methodology. Few changes were observed after 10 minutes of SVEP1 exposure; however, multiple phospho-proteins in the mammalian target of rapamycin (mTOR) signaling pathway were elevated after 30 minutes of SVEP1 exposure, including p70S6K, RPS6, and 4E-BP1 (Figure 5.6E). Immunoblot assays of phosphorylated mTOR (Ser 2448) and the mTOR-regulated

residue Thr 389 of p70S6K (191) further support an activation of mTOR signaling by SVEP1 (Figure 4C). Phosphorylation of p70S6K on residue 389 was also increased by the PEAR1pAb and serum after 30 minutes of exposure (Figure 5.7C). Transient knockdown of PEAR1 by siRNA abrogated mTOR activation by SVEP1, as determined by immunoblot assay of p70S6K phospho-Thr 389 relative to total p70S6K in hCASMCs (Figure 5.7D, 5.6F). Exposure of platelets to SVEP1 had similar effects on p70S6K Thr 389 (Figure 5.7E), consistent with mTOR activation. Small molecule inhibitors of SFK (PP1), endocytosis (Dynasore), AKT (MK-2206), and mTOR (Rapamycin) were added to platelets prior to SVEP1 exposure to test whether SVEP1-induced AKT/mTOR signaling was dependent on the respective protein or cell process. Activation of AKT by SVEP1 was completely abrogated by inhibition of SFK and AKT and partially abrogated by endocytosis inhibition. Phosphorylation of p70S6K Thr 389 was dependent on SFK and mTOR and partially dependent on endocytosis and AKT (Figure 5.7E). Taken together, these data suggest that activation of PEAR1 by SVEP1 induces AKT and downstream mTOR signaling.

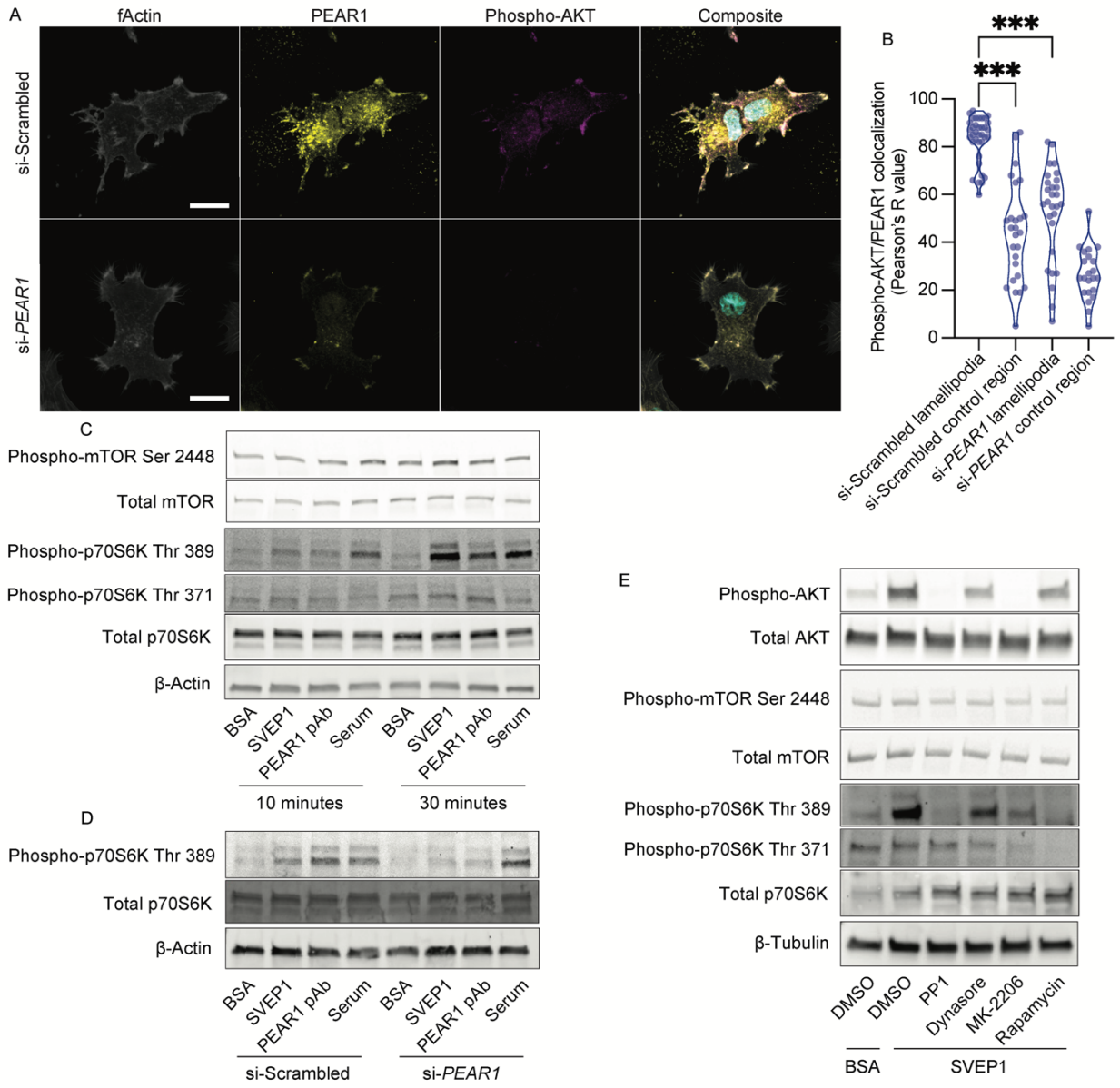


Figure 5.7 mTOR signaling is activated by SVEP1-induced PEAR1 signaling. (A) Images of hCASMCs pre-treated with scrambled siRNA or anti-*PEAR1* siRNA seeded on immobilized SVEP1 for 60 minutes. Scale bar = 20μm. Composite image includes DAPI (teal). (B) Quantification of PEAR1 and pAKT colocalization in (A), as determined by the Pearson correlation coefficient. Lamellipodia were identified as bundles of fActin on the periphery of cells. Cellular regions not containing lamellipodia were used as control regions. N = 22-36, P < 0.0001, ANOVA with post hoc unpaired t test. (C) HUVECs exposed to immobilized BSA or SVEP1, soluble PEAR1 pAb, or serum for 10 or 30 minutes. Lysates were analyzed by immunoblot assays for the indicated proteins. (D) hCASMCs were transfected with scrambled siRNA or anti-*PEAR1* siRNA prior to exposure to the listed stimuli. Lysates were analyzed by immunoblot assays for the indicated proteins. (E) Platelets were pretreated with DMSO (carrier), PP1 (SFK inhibitor), Dynasore (dynamin inhibitor), MK-2206 (AKT inhibitor), or Rapamycin

(mTOR inhibitor) prior to exposure to BSA or SVEP1. Lysates were analyzed by immunoblot assays for the indicated proteins.

### 5.3.6 SVEP1 induces platelet activation

Given the human genetic associations of *SVEP1* and *PEAR1* with platelet reactivity, we sought to characterize platelet phenotypes of *Svep1*$^{-/-}$ mice and littermate control *Svep1*$^{+/+}$ mice. Both genotypes of mice had similar platelet counts (Figure 5.8A). The levels of the platelet surface receptor CD41 were modestly lower in platelets from *Svep1*$^{-/-}$ mice compared to *Svep1*$^{+/+}$ controls (Figure 5.8B). This difference was variable between different mouse cohorts, however. To investigate platelet function, we tested the response of platelets to agonists including ADP and protease-activated receptor-4 activating peptide (PAR4-AP). We then measured platelet integrin αIIbβ3 activation (active CD41/61), using an antibody that detects its active conformation, and platelet alpha-granule secretion, using an antibody that recognizes P-selectin (CD62). ADP or PAR4-AP-stimulated platelets from *Svep1*$^{-/-}$ mice had significantly lower integrin activation as compared to stimulated platelets isolated from littermate controls (Figure 5.8C). Similarly, ADP-stimulation resulted in significantly lower P-selectin expression in platelets from *Svep1*$^{-/-}$ mice, as compared to controls (Figure 5.8D).

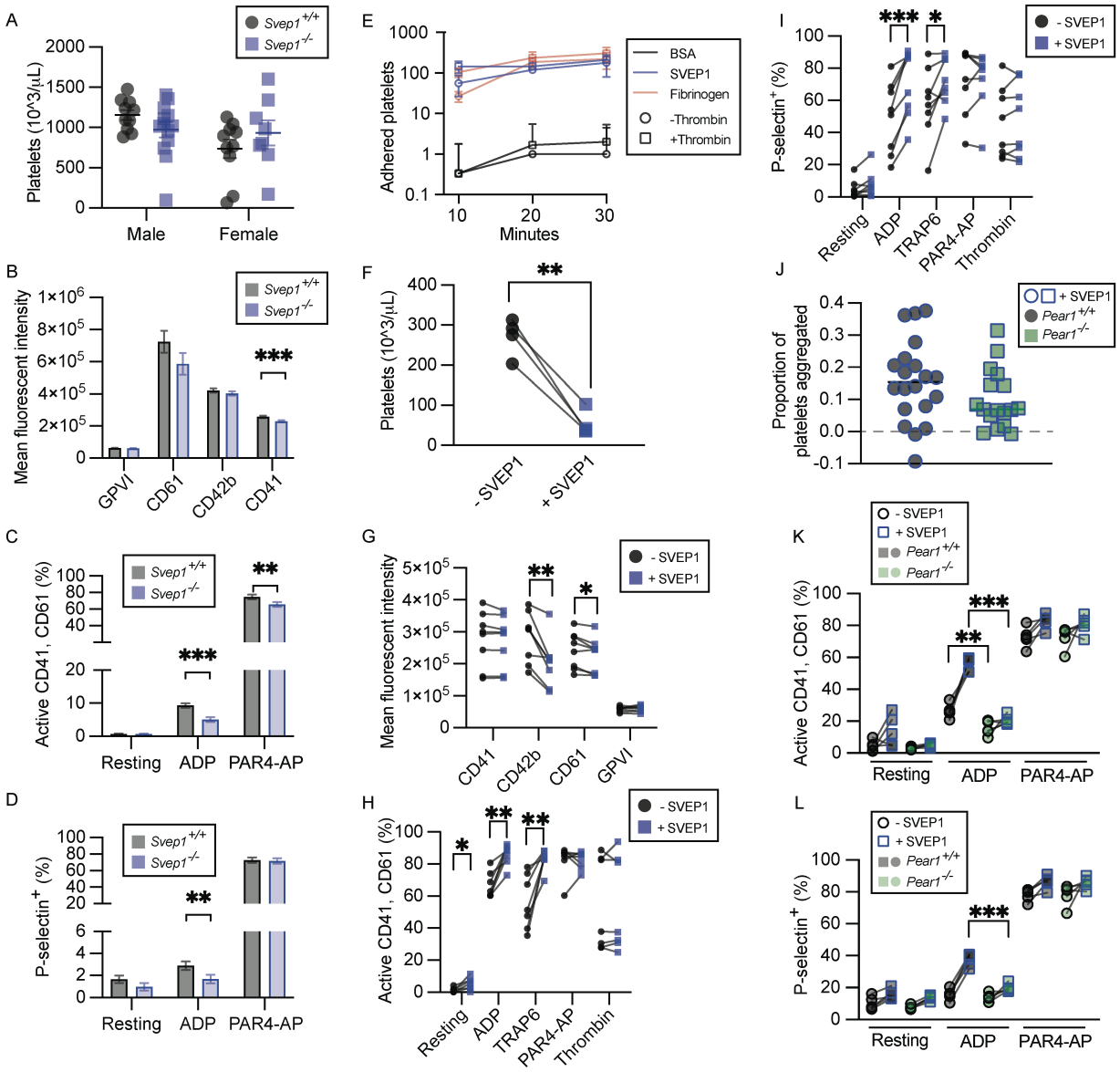


Figure 5.8 SVEP1 activates platelets.

(A) Platelet counts in whole blood from *Svep1*$^{+/+}$ and *Svep1*$^{-/-}$ mice. N = 8-13. (B) Mouse platelet receptor density determined by mean fluorescent intensity (MFI) in whole blood from *Svep1*$^{+/+}$ and *Svep1*$^{-/-}$, as determined by flow cytometry. N = 18-21. Bars represent least square means and error bars represent the standard error of difference (B-D). (C) Mouse activated CD41/61$^{+}$ platelets were determined by gating after flow cytometry of isolated platelets in resting conditions, or upon stimulation with ADP or PAR4-AP. N = 17-20. (D) Mouse P-selectin$^{+}$ platelets were determined by gating after flow cytometry of isolated platelets in resting conditions, or upon stimulation with ADP or PAR4-AP. N = 16-20. Two-way ANOVA (A-D). (E) Adherence of platelets to BSA (negative control), SVEP1, or Fibrinogen (positive control) coated coverslips for 10-30 minutes without an agonist or with addition of 0.1U/mL thrombin. N = 3. (F) Human whole blood platelet counts before and after addition of SVEP1. N = 4. Paired t test. (G) Human platelet receptor density determined by mean fluorescent intensity (MFI) of the

indicated proteins in freshly isolated platelets as determined by flow cytometry. N = 8. Paired t test. (H) Human activated CD41/61$^{+}$ platelets were determined by gating after flow cytometry of isolated platelets in resting conditions, or upon stimulation with 10μM ADP, 10μM TRAP6, or 0.1U/mL thrombin. N = 8. Paired t test. (I) Human P-selectin$^{+}$ platelets were determined by gating after flow cytometry of isolated platelets in resting conditions, or upon stimulation with 10μM ADP, 10μM TRAP6, or 0.1U/mL thrombin. N = 8. Paired t test. (J) The proportion of aggregated platelets was determined using murine whole blood cell counts from blood collected from *Pear1*$^{+/+}$ and *Pear1*$^{-/-}$ mice and treated with soluble SVEP1. The proportion of platelets aggregated was calculated as the difference in platelet count after addition of SVEP1 compared to before, taken as a proportion of the total platelets. N = 17-19. (K) Activated CD41/61$^{+}$ platelets were determined by gating after flow cytometry of isolated platelets before and after SVEP1 addition in resting conditions, or upon stimulation with ADP or PAR4-AP. N = 5. Unpaired t test. (L) P-selectin$^{+}$ platelets were determined by gating after flow cytometry of isolated platelets before and after SVEP1 addition in resting conditions, or upon stimulation with ADP or PAR4-AP. N = 5. Unpaired t test. *P < 0.05, **P < 0.01, ***P < 0.001.

Human platelets adhered to immobilized SVEP1 under static conditions with and without the presence of 0.1U/mL thrombin (Figure 5.8E). Recombinant SVEP1 was added to freshly isolated human platelets or whole blood to test the effect of soluble SVEP1 on platelets. Soluble, recombinant SVEP1 induced spontaneous platelet aggregation and agglutination of whole blood, as determined by decreases in whole blood platelet counts (Figure 5.8F). Platelets exposed to soluble SVEP1 had lower levels of receptor CD42b and CD61 (Figure 5.8G), suggesting receptor shedding and platelet pre-activation. Platelets exposed to SVEP1 also had increased integrin αIIbβ3 activation under basal conditions and upon stimulation with ADP and Thrombin receptor-activating peptide-6 (TRAP6) (Figure 5.8H). P-selectin expression was also increased in isolated platelets after addition of exogenous SVEP1 and stimulation with ADP and TRAP6 (Figure 5.8I). Similar effects were observed in platelets within whole blood upon exposure to SVEP1 (Figure 5.9A-C). The SVEP1 variant (p.R229G) that associates with increased platelet reactivity in humans is also associated with increased plasma SVEP1 (18, 64), supporting these findings.

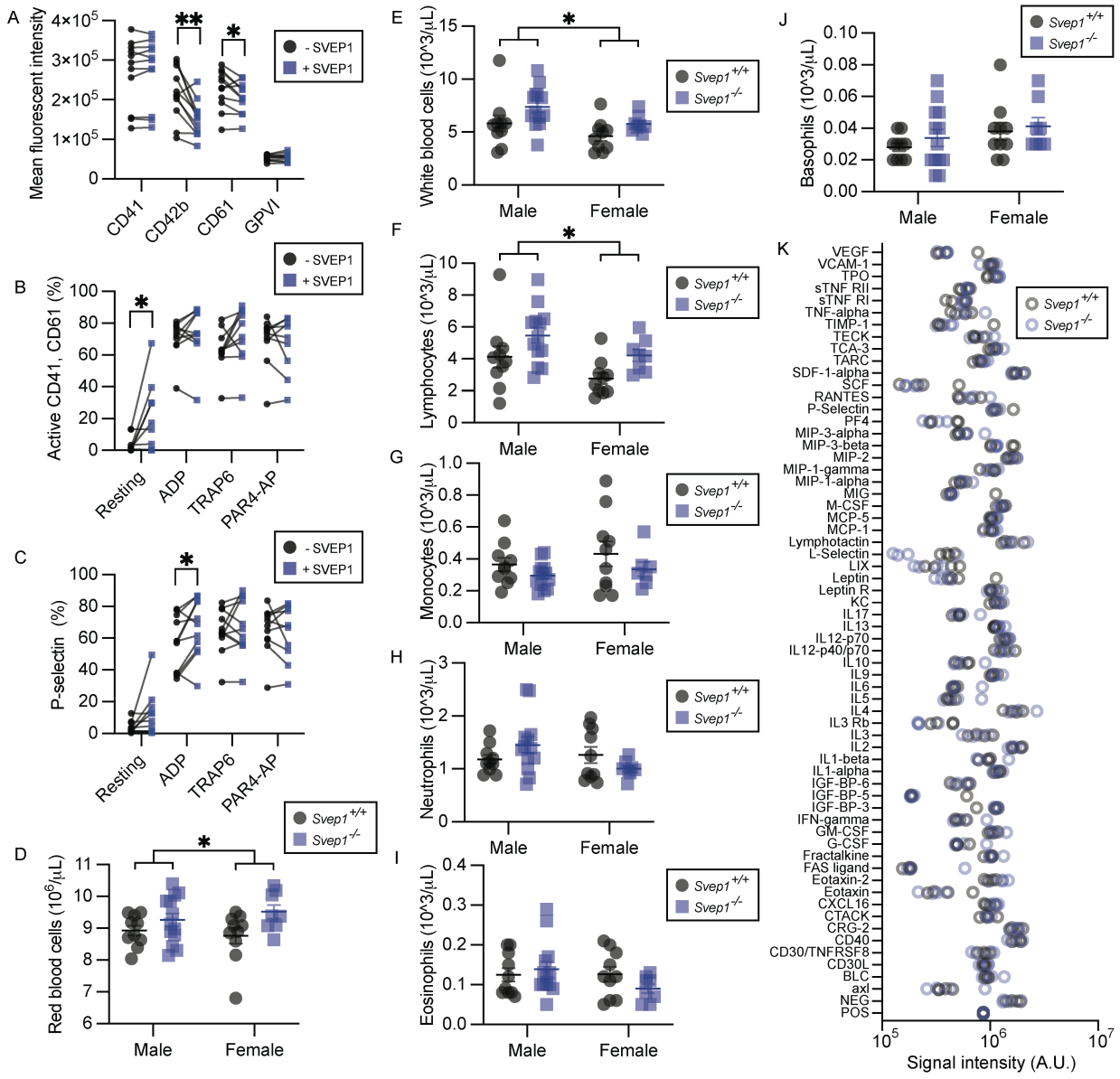


Figure 5.9 SVEP1 activates platelets, continued.
(A) Platelet receptor density determined by mean fluorescent intensity (MFI) of the indicated proteins in platelets from whole human blood as determined by flow cytometry. N = 11. Paired t test. (B, C) Activated CD41/61$^{+}$ (B) and P-selectin$^{+}$ (C) platelets were determined by gating after flow cytometry of platelets from whole human blood in resting conditions, or upon stimulation with 10μM ADP, 10μM TRAP6, or 0.1U/mL thrombin. N = 10-11. Paired t test. (D) RBC counts in whole blood isolated from *Svep1*$^{+/+}$ and *Svep1*$^{-/-}$ mice N = 20-21. (E-J) White blood cell count (E), lymphocyte count (F), monocyte count (G), neutrophil count (H), eosinophil count (I), and basophil count (J) of blood isolated from *Svep1*$^{+/+}$ and *Svep1*$^{-/-}$ mice as determined by hemocytometry. N = 20-21. *P < 0.05, **P < 0.01, ***P < 0.001, Two-way ANOVA for all panels, unless otherwise noted. (K) Densitometry quantification of the listed protein using a cytokine array of blood isolated from *Svep1*$^{+/+}$ and *Svep1*$^{-/-}$ mice. N = 4.

We then tested whether the effects of SVEP1 on platelets were dependent on PEAR1 using *Pear1*$^{-/-}$ mice (192). The effects of SVEP1 on platelet aggregation and agglutination were notably milder in platelets from mice (Figure 5.8J) compared to humans (Figure 5.8F), consistent with previous reports that murine PEAR1 plays a less prominent role in platelet function than human PEAR1 (193). Upon activation with ADP, murine platelets derived from *Pear1*$^{-/-}$ mice and incubated with SVEP1 had reduced integrin activation (Figure 5.8K) and P-selectin expression (Figure 5.8L) compared to platelets from control mice.

We therefore conclude, using three methodologically independent techniques (mouse models, exogenous SVEP1 assays, and human multi-omics) that SVEP1 promotes platelet activation, likely by signaling through PEAR1. Many of the effects of SVEP1/PEAR1 on platelet activation were potentiated by ADP; this finding is consistent with previous PEAR1 studies (50, 193) and the GWAS associations of *SVEP1* and *PEAR1* with platelet response to ADP-stimulation in humans (18).

Given the platelet phenotypes in *Svep1*$^{-/-}$ mice, we assessed additional hematological phenotypes in these mice and found that *Svep1*$^{-/-}$ mice had higher red blood cell (RBC) counts (Figure 5.9D) relative to control *Svep1*$^{+/+}$ mice. This is consistent with genetic association of *SVEP1* with human RBC phenotypes (20). In addition, blood from *Svep1*$^{-/-}$ mice had greater total numbers of white blood cells and lymphocytes (Figure 5.9E,F). Total numbers of monocytes, neutrophils, eosinophils, and basophils were not appreciably different between *Svep1*$^{+/+}$ and *Svep1*$^{-/-}$ mice (Figure 5.9G-J). We then assessed whether plasma cytokine levels may explain the hematological differences between *Svep1*$^{+/+}$ and *Svep1*$^{-/-}$ mice using a cytokine array. No significant differences in plasma cytokines were observed between *Svep1*$^{+/+}$ and *Svep1*$^{-/-}$ mice (Figure 5.9K), perhaps reflecting the modest effects of *Svep1* on immune cell populations.

### 5.3.7 SVEP1 and PEAR1 are causally related to human platelet phenotypes and CAD

We then asked whether SVEP1 and PEAR1 causally relate to human traits and disease. MR was used to test the impact of plasma SVEP1 and PEAR1 on mean platelet volume (MPV) and platelet count (PLT). We found that genetically determined increased plasma concentrations of both proteins associated with increased MPV (Figure 5.10A; SVEP1 $P = 5.1x10^{-6}$; PEAR1 $P = 1.8x10^{-8}$) and decreased PLT (Figure 5.10B; SVEP1 P = 0.015; PEAR1 $P = 2.3x10^{-5}$). Similarly, genetically encoded changes in plasma concentrations of both proteins are positively associated with risk of cardiovascular disease (Figure 5.10C; SVEP1 $P = 4.5x10^{-12}$; PEAR1 P = 0.0051). These data demonstrate that both SVEP1 and PEAR1 causally relate to platelet traits and CAD. The effects of the proteins are concordant, consistent with the hypothesis that the two proteins interact to influence disease.

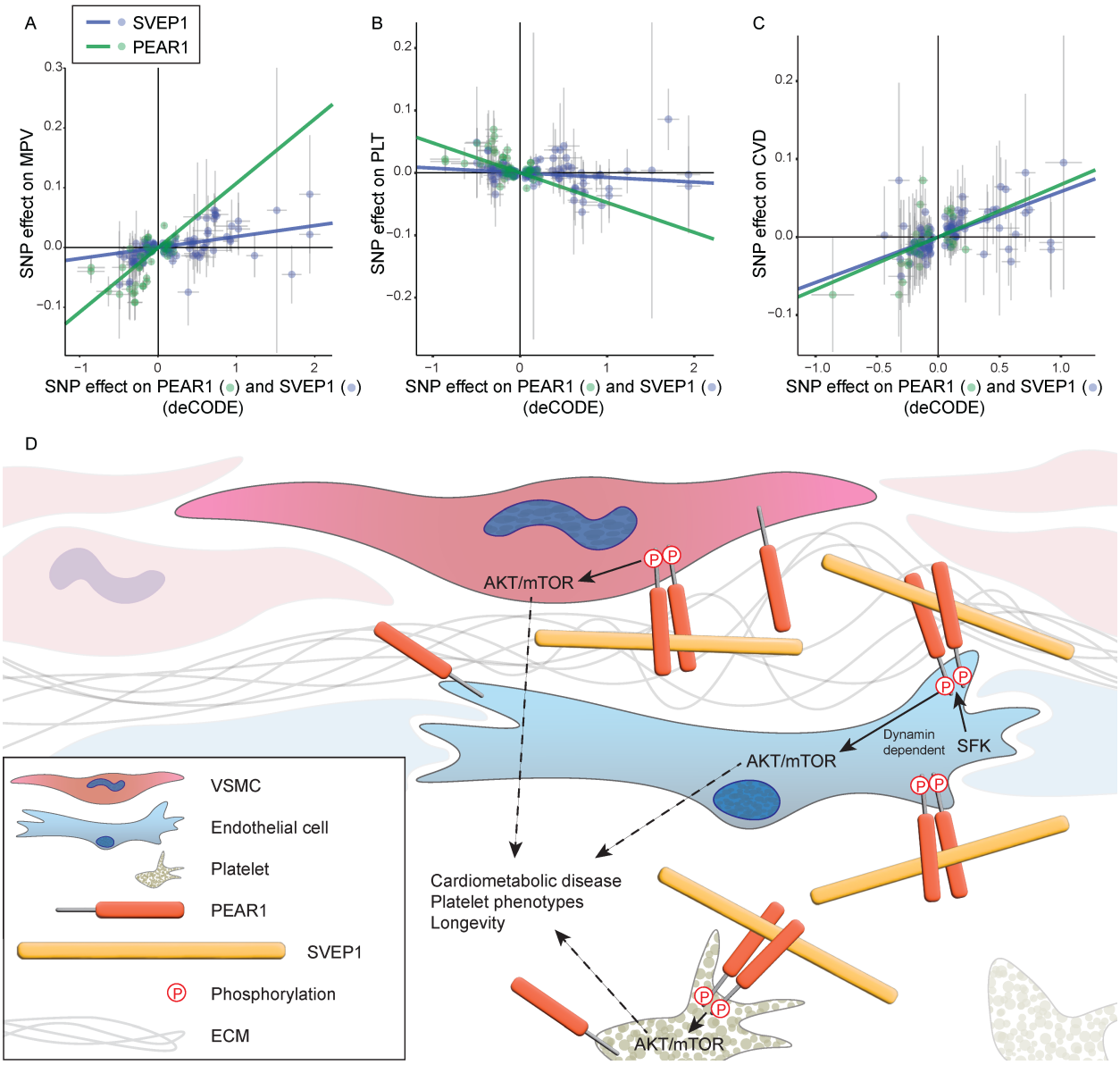


Figure 5.10 SVEP1 and PEAR1 causally and concordantly relate to human platelet traits and cardiovascular disease.

(A) Two-sample MR of estimated SNP effects (with 95% confidence intervals) on MPV (y-axis) and either PEAR1, green, or SVEP1, blue, in deCODE (x-axis). The causal estimate is designated by a line of the corresponding color. SVEP1 Beta = 0.018, P = $5.1 \times 10^{-6}$; PEAR1 Beta = 0.11, P = $1.8 \times 10^{-8}$. (B) Two-sample MR of estimated SNP effects (with 95% confidence intervals) on platelet count (y-axis) and either PEAR1, green, or SVEP1, blue, in deCODE (x-axis). The causal estimate is designated by a line of the corresponding color. SVEP1 Beta = -0.0075, P = 0.015; PEAR1 Beta = -0.048, P = $2.3 \times 10^{-5}$. (C) Two-sample MR of estimated SNP effects (with 95% confidence intervals) on cardiovascular disease (y-axis) and either PEAR1, green, or SVEP1, blue, in deCODE (x-axis). The causal estimate is designated by a line of the corresponding color. SVEP1 Beta = 0.058, P = $4.5 \times 10^{-12}$; PEAR1 Beta = 0.067, P = 0.0051. (D)

Model of the vascular wall and lumen. Solid lines represent experimentally tested relationships. Dashed lines represent relationships supported by indirect evidence.

## 5.4 Discussion

Recent genomic and proteomic studies have implicated SVEP1 and PEAR1 in a variety of overlapping human traits and diseases. Our understanding of the mechanisms of these proteins has been limited; however, since little was known about their molecular interactions. Previous studies have reported an interaction between PEAR1 and High affinity immunoglobulin epsilon receptor subunit alpha (FcεRIα) (178); however, the differing expression pattern of these two proteins, the inability of FcεRIα to activate platelets, and the lack of conservation in mouse suggests FcεRIα is not a physiological ligand of PEAR1 (174). Similarly, the only protein known to interact with SVEP1 is integrin α9β1. Both SVEP1 and integrin α9β1 play a role in lymphangiogenesis, however *Svep1*$^{-/-}$ mice die much earlier than *Itga9*$^{-/-}$ mice (embryonic day 18.5 vs postnatal day 14, respectively) (47). Svep1 plays a similar developmental role in zebrafish, but *itga9*$^{-/-}$ larvae do not phenocopy *svep1*$^{-/-}$ larvae and zebrafish Svep1 lacks an integrin α9β1 binding domain (79). These findings suggest the SVEP1 may have additional interactions related to its role in development and disease.

Here, we provide evidence that SVEP1 is a physiological ligand of PEAR1. The observation that PEAR1 D343N impacts plasma SVEP1 levels in humans led us to test the causal relationship between plasma PEAR1 and plasma SVEP1, since an inverse correlation would suggest PEAR1 can sequester plasma SVEP1. Indeed, genetically-encoded plasma PEAR1 levels are strongly inversely correlated with plasma SVEP1 levels. SVEP1 and PEAR1 physically interact and immobilized SVEP1 activates canonical PEAR1 signaling in a PEAR1-dependent fashion. We also found that mTOR signaling is activated downstream of SVEP1/PEAR1-induced AKT activation; these findings are summarized in Figure 5.10D. It is unclear whether activation of

AKT/mTOR by SVEP1/PEAR1 is directly responsible for their causal disease and trait associations; however, these pathways are well known to contribute to platelet biology (52, 55), cardiometabolic disease (53, 54, 57, 59), and longevity (58).

Several independent studies have reported associations between SVEP1 and PEAR1 in cardiovascular disease and platelet phenotypes (6, 18, 162, 169-171), yet causality is more difficult to assess. Here we provide evidence that both proteins causally relate to human cardiovascular disease and platelet phenotypes using MR and mouse models. Mendelian Randomization can be used to test causal relationships in human biology and disease without the resource constraints and ethical limitations of clinical trials. This method relies on SNPs within a population that influence a quantitative exposure, such as plasma protein concentration, and an outcome of interest. A critical assumption of this technique is that the SNP exclusively influences the exposure (194). Most SNPs comprising the genetic instruments in this manuscript are non-coding; therefore, their associated differences in plasma protein concentration are likely a manifestation of the quantitative differences in protein production rather than functional differences. Proteins are known to leak from tissue to plasma and rigorous techniques have demonstrated that SVEP1 behaves in this manner (10). Taken together, this suggests plasma protein concentration may be a proxy for tissue levels of the protein. The mechanisms of SVEP1 and PEAR1 ingress and stability in the plasma are unclear; however, the variables that regulate this process are randomly distributed across the cohort according to Mendel's law of independent assortment and therefore should not be a source of confounding. Given that plasma protein concentration may reflect tissue protein concentration, we conclude that the causal relationships of SVEP1 and PEAR1 described in this study are not limited to explanations pertaining to the

plasma. Nevertheless, the effects of the proteins on CAD, platelet volume, and platelet count are concordant, consistent with the disease mechanisms of SVEP1 and PEAR1 being inter-related. Several studies have independently concluded that increased SVEP1 in deleterious in humans (3, 4, 7, 13, 195). A single study in mice contrasts these conclusions by reporting that *Svep1* haploinsufficiency increased atherosclerosis (31); however the results were difficult to interpret due to confounding introduced by differing proportions of males and females in their control and experimental groups (32, 33). Our previous study avoided this source of bias and directly contradicted their conclusions using the same model in addition to complementary mouse models and outcomes (3). SVEP1 is critical for proper development in mice (79), but our findings suggest that it may be dispensable in the adult animal, since we did not appreciate any biologically significant adverse cardiometabolic phenotypes in aged, metabolically challenged *Svep1*$^{-/-}$ mice. The human population variance of genetically encoded SVEP1 and PEAR1 levels suggests a safe therapeutic window exists to target SVEP1 and/or PEAR1 and potentially reduce their associated disease burden. The interaction between SVEP1 and PEAR1 occurs within the extracellular space, making this interaction an intriguing target for pharmacological intervention. Additional studies will be necessary to further characterize the mechanisms by which SVEP1 and PEAR1 influence disease and evaluate the potential of therapeutically disrupting their interaction.

## 5.5 Methods

### 5.5.1 Study approval

Blood collection from consenting healthy controls was conducted in accordance with the Institutional Review Board of Washington University, St Louis. All animal studies were performed according to procedures and protocols approved by the Animal Studies and Institutional Animal Care and Use Committees of the Washington University School of Medicine.

### 5.5.2 Statistics

The specific statistical methods used to analyze each set of data are described in the figure legends and/or the specific methods section. The paired data were analyzed by a two-tailed, paired t test. The unpaired data were analyzed by a two-tailed, unpaired t test or a two-way analysis of variance (ANOVA) if another variable, such as sex, was a potential source of variation. One-way ANOVA was used when making multiple comparisons to a single reference group, followed by the indicated statistical test. Individual data points were shown whenever possible, however least squared means were used to simplify data visualization in limited cases. Data were excluded prior to analysis whenever a technical error was noted during data collection. Extreme outliers were excluded from the mouse hematological studies using the ROUT method under the most stringent threshold (Q = 0.1%). The cell culture and molecular data included in this manuscript are representative of at least two independent experiments. The animal experiments were performed at least once. The protein array experiments served as a screening tool and were performed once. Excluding the indirect calorimetry measurements, the animal experiments were performed in blinded and randomized fashion. The cellular studies, molecular studies, and the data analysis were performed in unblinded fashion. Densitometry of

immunoblots was performed using Image Lab and reported whenever the results were not abundantly clear. The data were analyzed and graphed in GraphPad PRISM 8 or 9. The data panels were imported and formatted into figures using Adobe Illustrator. Stars were used to denote statistical significance in the functional studies. *P< 0.05, **P< 0.01, ***P< 0.001.

### 5.5.3 Mendelian Randomization

Genome-wide summary statistics for plasma levels of SVEP1 (aptamer SVEP1.11109.56.3 and aptamer SVEP1.11178.21.3) and PEAR1 (aptamer PEAR1.8275.31 chosen for its ability to detect *PEAR1* cis-pQTLs (4)) were obtained from the previously published INTERVAL (4) and deCODE (64) studies in 3,301 European and 35,559 Icelandic individuals, respectively. We used unlinked GWAS markers ($r^2 \leq 0.2$) from deCODE (as estimated from 1000G European sequence data (196)) to generate instrumental variables for plasma levels of SVEP1 and PEAR1. As trans-pQTLs may affect protein levels in a variety of manners, we focused our analysis on cis-pQTLs by only including variants in a 250kb window surrounding the gene of interest and associated with altered plasma levels of the associated protein at a level exceeding genome-wide significance (P-value for respective plasma protein concentration $\leq 5 \times 10^{-8}$).

The reported outcomes included plasma levels of proteins from INTERVAL, platelet traits, and CAD. For blood platelet traits, we obtained previously published summary statistics for platelet count and mean platelet volume in Europeans (19). Summary statistics for CAD were obtained from the previously published meta-analysis of UK Biobank and CARIDoGRAMPlusC4D (74). Causal analysis was performed using the inverse-variant weighted method implemented in the R package TwoSampleMR (197).

### 5.5.4 Cell signaling and immunoblot assays

A list of cellular reagents is provided in Index A. Primary human umbilical vein endothelial cells (HUVECs) were obtained from Cell Applications Inc. and cultured according to the manufacture's recommendations. Primary human coronary artery smooth muscle cells were obtained from Invitrogen and were cultured according to the manufacture's recommendations. 293T cells were obtained from ATCC and were cultured according to the manufacture's recommendations. Mouse primary smooth muscle cells were obtained and cultured as described previously (3). Predesigned Silencer Select siRNA constructs targeting *PEAR1* and negative control siRNA were obtained from ThermoFisher. Transfections were performed using RNAiMAX or Lipofectamine 3000 transfection reagents according to the manufacturer's protocols. Cells were used for signaling assays 48 hours after transfection; efficient PEAR1 knockdown or PEAR1 overexpression was confirmed by immunoblot assays.

Prior to performing signaling assays, cells were trypsinized, centrifuged, suspended in basal media, and counted using an automated hemocytometer. Cells were further diluted in basal media to an assay-dependent concentration. Cells were then incubated with gentle agitation for 60 minutes to prevent cell attachment and reduce basal signaling. PP1, Dynasore, MK-2206, and Rapamycin were diluted in DMSO and used in assay concentrations of 10μM, 100μM, 10μM, and 1μM, respectively, for the final 20-30 minutes of incubation in basal media. An equal volume of DMSO was used as the negative control condition. 1mL of the cell-culture was then seeded on 24-well tissue culture plates pre-coated with 15-30μg/mL BSA or SVEP1 and washed with Dulbecco's phosphate-buffered saline (DPBS). 1 μg PEAR1 polyclonal antibody was added as a specific positive control. 20% growth media or 2% fetal bovine serum, labelled "Serum" in figures, was added as a non-specific positive control. The cells were centrifuged at 300G for 3 minutes with the exception of platelets, which were centrifuged at 500G for 5 minutes. The cells

were then incubated at 37°C for 8 – 45 minutes, depending on the cell type and pathway of interest. The cells were lysed in radioimmunoprecipitation buffer (RIPA) containing a cocktail of protease and phosphatase inhibitors and universal nuclease. Immunoblots were performed by standard techniques, as briefly follows. Protein content was determined using a bicinchoninic acid assay with BSA standards (#23225, Pierce BCA Protein Assay Kit). Cell lysates were then reduced with dithiothreitol (DTT) in lithium dodecyl sulfate (LDS) sample buffer (#NP0007, Invitrogen). Equal protein amounts were added to polyacrylamide gels (#4561086, BioRad) and electrophoresed prior to transferring to a nitrocellulose or polyvinylidene fluoride membrane (#1620260, BioRad). Membranes were blocked in 5% BSA/Tris-buffered saline (TBS) with 0.1% Tween 20 for 30 minutes. The indicated primary antibodies were incubated with the pre-blocked membranes overnight at 4°C. Membranes were washed with TBS with 0.1% Tween 20, probed with fluorescent secondary antibodies, and imaged. β-actin or β-tubulin served as a loading control.

For the protein array assays, HUVEC cell lysates were used with the C-Series Human and Mouse AKT Pathway Phosphorylation Array C1 (Raybiotech Inc.) according to the manufacturer's protocol. The signal intensity was normalized to the lysates from negative control BSA-coated wells. Plasma was pooled from two *Svep1*$^{+/+}$ or *Svep1*$^{-/-}$ mice to constitute a single biological replicate for the mouse cytokine array C3 assay; two samples were derived from each sex of each mouse genotype for the assay.

### 5.5.5 Adhesion assay

Wells of a 96 well plate were pre-coated with 0, 1, 3, 10, 20, 30, and 50µg/mL recombinant SVEP1 or 10µg/mL plasma fibronectin (pFn, as a positive control) in DPBS. Subsequently, wells were blocked with 100mg/mL BSA and washed with DPBS. HUVECs were collected and

resuspended in basal media. 5,000 cells were added to each well. Cells were centrifuged and incubated at 37°C for 10 minutes. The plate was gently centrifuged upside down to remove non-adhered cells. Adhered cells were fixed with 4% paraformaldehyde, stained with 4′,6-diamidino-2-phenylindole (DAPI), and counted by automated microscopy as done previously (3).

### 5.5.6 Immunoprecipitation

For the PEAR1 immunoprecipitation (IP): 150µg of cell lysates from human platelets exposed to immobilized BSA, SVEP1, or a soluble polyclonal PEAR1 antibody for 15 minutes were incubated with 2µg PEAR1 monoclonal antibody (R&D Systems) for 2 hours. Subsequently, 20µL of BSA-blocked Invitrogen Protein A Dynabeads slurry was added, followed by rotation for 45 minutes. The beads were separated using magnetism and washed with RIPA buffer 4-5 times, then resuspended with reducing LDS sample buffer and analyzed by immunoblot assay. Bands for p-tyrosine and PEAR1 were detected at ~140kDa.

For the SVEP1/PEAR1 Co-IP: Recombinant SVEP1-Myc and PEAR1ECD-Bio-His or PEAR1ECD (R&D Systems) was added to assay buffer in microcentrifuge tubes in a 3:1 mass ratio, resulting in an approximately equal molar ratio. The assay buffer consisted of 1mg/mL BSA, 0.01% Tween 20, and 10mM $Ca^{2+}$ in PBS. The proteins were incubated together for two hours while rotating. Where indicated, 2µg primary antibodies were added during the final 30 minutes of the initial incubation. Following the incubation, aliquots were reserved as the input fraction. Subsequently, 6-10µL slurry of Pierce Anti-c-Myc Magnetic Beads, Invitrogen Dynabeads Protein G beads, or Pierce Streptavidin Magnetic Bead slurry were added, followed by a 1-hour incubation at 20°C with gentle agitation. Beads were washed in PBS + 0.01% Tween 20 and resuspended reducing LDS sample buffer and analyzed by immunoblot assay. Bands for

SVEP1 were detected at approximately 300kDa. Bands for PEAR1ECD were detected at approximately 105kDa.

### 5.5.7 Cell imaging and colocalization analysis

HUVECs or si-RNA transfected hCASMCs were trypsinized and seeded on chamber slides precoated with 30μg/mL SVEP1. Cells were incubated for one hour at 37°C, rinsed with DPBS, and fixed with 4% paraformaldehyde. Cells were washed, then blocked and permeabilized with 0.3% Triton X-100 and 5% chicken serum in TBS. Cells were incubated with PEAR1 pAb and anti-pAKT antibody for two hours, washed with TBS + 0.1% Tween 20, and incubated with secondary antibodies and phalloidin stain (for fActin), for 1 hour. Chambers not treated with the primary antibody were used as a negative control. Cells were washed and treated with Prolong Diamond Antifade with DAPI overnight at room temperature. The cells were imaged the following day using confocal microscopy. The fluorescent channel for fActin was used to identify cells and focus the microscope for imaging. Composite images were split into composite pseudocolors using Fiji. The fActin channel was used to identify lamellipodia (bundles of fActin on the periphery of cells) and control, non-lamellipodia cellular regions (see Figure S3C for representative images). The Fiji plugin Coloc 2 was used to measure intensity-independent colocalization between the PEAR1 and pAKT channels. Pearson's correlation coefficient was reported as a measure of colocalization between PEAR1 and pAKT.

### 5.5.8 Human blood collections and platelet isolation

Whole blood was collected by venipuncture into either heparin vacutainers (BD, Franklin Lakes) for whole blood experiments or acid-citrate-dextrose (ACD) vacutainers (BD, Franklin Lakes) for platelet isolation studies. For platelet isolation, samples were supplemented with apyrase (Sigma, St Louis) and prostaglandin E1 (Cayman Chemical, Ann Arbor) and platelet rich plasma

(PRP) was prepared by centrifugation of the ACD whole blood for 20 minutes at 200G. Platelets were isolated from the PRP by centrifugation for 10 minutes at 1000G and re-suspended in modified Tyrode's buffer twice at desired platelet counts and kept at 37°C until used. Isolated platelets were used within 2 hours of preparation.

### 5.5.9 Static adhesion assays

Coverslips were pre-coated with either 15µg/mL recombinant SVEP1, 100µg/mL fibrinogen (as a positive control) or 1% BSA (as a negative control) in phosphate-buffered saline (PBS). Subsequently, coverslips were blocked with 1% BSA and washed with PBS. Human platelets were isolated from whole blood and re-suspended in Tyrode's buffer. $2x10^7$/mL basal or thrombin activated platelets were added to coverslips and incubated at 37°C for 10, 20, or 30 minutes. After incubation, non-adherent platelets were removed and the coverslips were washed with PBS, fixed with 1.5% paraformaldehyde, permeabilized with 0.01% Triton-X and stained with TRITC phalloidin. Platelets were visualized using fluorescent microscopy. Images of the adhered platelets were captured using fluorescent microscopy and counted manually by a blinded observer.

### 5.5.10 Blood cell counts and flow cytometry

Complete blood counts (CBC) and washed platelet counts were determined using a hematology analyzer Element HT5 (Heska, Loveland). For platelet aggregation experiments, whole blood platelet count was measured prior to SVEP1 addition and 15 minutes after addition of 15µg/mL SVEP1. For flow cytometry, diluted whole blood or isolated platelets were pre-incubated with their respective fluorescent antibodies for 15 minutes and fixed. For murine whole blood: CD41-VioBlue, CD61-PE (Mitlenyi Biotec, Bergisch Gladbach, Germany), CD42b-DL649, GPVI-FITC (Emfret, Eibelstadt, Germany) and for human whole blood and isolated platelets: CD41-

FITC, CD61-APC, CD42b-PE (Biolegend, San Diego), GPVI-BV421 (BD, Franklin Lakes). Platelet surface receptor levels were quantified by flow cytometry on a CytoFlex analyzer.

### 5.5.11 Quantification of Platelet Integrin αIIbβ3 Activation and P-Selectin Expression

Diluted human whole blood or isolated human platelets were treated with SVEP1 as described previously, pre-incubated with FITC-PAC-1 and P-selectin-PE antibodies (BD, Franklin Lakes), and stimulated with either ADP (10μM) (Chronolog, Harverton); Thrombin receptor-activating peptide-6 (TRAP-6; 10μM) (Tocris, Bristol, UK); Protease-activated receptor-4 activating peptide (PAR4-AP; 100μM) (Abcam, Cambridge, UK) or Thrombin (0.1U/mL) (Chronolog, Harverton) for 15 minutes. Samples were immediately fixed and run using a CytoFlex analyzer and (Beckman Coulter, Pasadena) and analysis was performed with Kaluza software (Beckman Coulter, Pasadena).

For murine whole blood flow cytometry, whole blood was collected from the retro-orbital plexus using heparinized capillary tubes. Diluted whole blood was pre-incubated with fluorescently conjugated JON/A-FITC and CD62P-PE antibodies (Emfret, Eibelstadt, Germany) and stimulated with either ADP (10μM), PAR4-AP (100μM) or Thrombin (0.1U/mL) for 15 minutes. After incubation, samples were immediately fixed and read on a CytoFlex analyzer.

### 5.5.12 Mice

The generation and validation of an inducible *Svep1*$^{-/-}$ allele and mouse model was described previously (3). In brief, mice were generated by KOMP (Knockout Mouse Project) and crossed with mice expressing the flippase FLP recombinase under the control of the promoter of the human actin beta gene to generate *Svep1*$^{flx/flx}$ mice. We crossed these mice with *Rosa26-CreER*$^{T2}$ (no. 008463, the Jackson Laboratory) mice to generate *Svep1*$^{flx/+}$*Rosa26-CreER*$^{T2}$ mice. Male and female *Svep1*$^{flx/+}$*Rosa26-CreER*$^{T2}$ were crossed to generate experimental

*Svep1*$^{flx/flx}$*Rosa26-CreER*$^{T2}$ (*Svep1*$^{-/-}$) and *Svep1*$^{+/+}$*Rosa26-CreER*$^{T2}$ (*Svep1*$^{+/+}$) littermate control mice. To activate Cre-recombinase, mice were injected intraperitoneally with 2.5mg of tamoxifen (no. T5648, Sigma-Aldrich) in 0.1mL of peanut oil (no. P2144, Sigma-Aldrich) for 5 consecutive days starting at 6 weeks of age. Tamoxifen treatment was performed with all experimental and control mice in an identical manner. Given the cardiometabolic and age-related disease associations of *SVEP1* in humans, we used aged *Svep1*$^{-/-}$ and control *Svep1*$^{+/+}$ mice fed a western diet comprised of 21% fat by weight (42% kcal from fat) and 0.2% cholesterol (#TD.88137, Envigo Teklad) beginning at 8 weeks of age. This diet was referred to as "HFD" throughout the text. The metabolic phenotyping of these mice occurred between 8-9 months of age, the hematological phenotyping occurred between 10-12 months of age, and the vascular phenotyping occurred between 12-13 months of age.

The mice referred in this text as "*Pear1*$^{-/-}$" are the *Pear1*$^{tm1a(KOMP)Wtsi}$ mice generated by KOMP (generously provided by Dr. Bruce Carter, Vanderbilt University). The "*Pear1*$^{+/+}$" control mice are age and background matched C57BL/6NCrl mice (Charles River Laboratories) and were acclimated in the same facility as the *Pear1*$^{-/-}$ mice for at least one week prior to the experiments. The *Pear1*$^{-/-}$ and *Pear1*$^{+/+}$ mice were fed a standard chow diet and were assessed at 6 weeks of age. All mice were housed in the Washington University School of Medicine animal facility and maintained on a 12-hour light/12-hour dark cycle with a room temperature of 22 ± 1°C.

### 5.5.13 Proteomic pulldown assays

Affinity based proteomics: Murine VSMCs were grown to confluence in serum-containing media and changed to serum-free media to generate enriched media. Recombinant, Myc-tagged SVEP1 was added to the media after two days of enrichment and incubated for 1 hour. An aliquot was removed after incubation as the "input" fraction. Media was then added to a slurry of

Pierce Anti-c-Myc Magnetic Beads + 0.05% Tween 20 and incubated for 30 minutes while rocking at 4°C. The beads were then washed twice with $Ca^{2+}$ and $Mg^{2+}$-containing PBS (D8662, Sigma) + 0.05% Tween 20 and twice with $Ca^{2+}$ and $Mg^{2+}$-containing PBS before a final resuspension in PBS. An aliquot of the beads was reserved as the pulldown fraction for validation. Proximity based proteomics: recombinant SVEP1-Myc or SVEP1-mTID was added to enriched VSMC media with 500µM exogenous biotin and 1mM adenosine triphosphate (ATP). The samples were incubated for 4 hours prior to dialysis. Protease arrest (G-Biosciences) was added and excess biotin was dialyzed using a 10kDa molecular weight cut-off (MWKO) Slide-A-Lyzer™ dialysis Cassette (ThermoFisher Scientific) in buffered saline + 1mM EDTA. The samples were then transferred to 10kDa MWKO Vivasin column (Sartorius Stedim Biotech), centrifuged, resuspended in RIPA buffer, centrifuged, and added to pre-washed Pierce Streptavidin Magnetic Beads. The samples and beads were incubated for 1 hour at room temperature or overnight at 4°C and then washed with the following solutions: RIPA buffer, 1M KCl, 0.1M $Na_2CO_3$, 2M urea in 10mM Tris HCl (pH = 8.0), and PBS (186). The beads were then resuspended in PBS for peptide preparation.

### 5.5.14 Peptide preparation

The peptides were prepared using a previously described method for on-bead tryptic digestion (198). The beads were washed four times with 1mL of 50mM ammonium bicarbonate buffer (pH = 8.0) (ABC). The washed beads were resuspended in 40µL of ABC buffer containing 8M urea. The protein disulfide bonds were reduced using 2µL of 0.5M TCEP and incubation for 60 minutes at 30 ºC. The reduced proteins were alkylated using 4µL of a 0.5M solution of iodoacetamide with incubation for 30 minutes at RT in the dark. The urea was diluted to a concentration of 1.5M by adding 167µL of 50mM ABC buffer. After addition of LysC (1mAU),

the samples were incubated for 2 hours at 30°C in a Thermomixer with gyration at 750rpm. Trypsin (1µg) was added and the samples were incubated overnight at 30°C in the Thermomixer gyrating at 750rpm. The peptides were transferred to a 1.5mL tube, the beads were washed with 50µL of ABC buffer and the transfer and wash volumes were combined. Any residual detergent was removed by ethyl acetate extraction (199). The peptide samples were acidified with TFA to a final concentration of 1% (vol/vol) TFA (pH < 2.0). The pH was checked with pH paper. The peptides were desalted using two micro-tips (porous graphite carbon, BIOMETNT3CAR) (Glygen) on a Beckman robot (Biomek NX), as previously described (200). The peptides were eluted with 60% (vol/vol) MeCN in 0.1% (vol/vol) TFA. After adding TFA to a final concentration of 5%, the peptides were dried in a Speed-Vac (Thermo Scientific, Model No. Savant DNA 120 concentrator). The peptides were dissolved in 20µL of 1% (vol/vol) MeCN in water. An aliquot (10%) was removed for quantification using the Pierce Quantitative Fluorometric Peptide Assay kit (Thermo Scientific, Cat. No. 23290). The remainder was transferred to autosampler vials (Sun-Sri, Cat. No. 200046), dried and stored at -80ºC. Peptides were also prepared after release of proteins from antibody beads. The beads were washed with 1mL of 50mM cold phosphate buffered saline (pH 8.0) (PBS) followed by elution with 30µL of SDS buffer (4% (wt/vol), 100mM Tris-HCl pH 8.0). The protein disulfide bonds were reduced using 100mM DTT with heating to 95ºC for 10 minutes. Peptides were prepared as previously described using a modification (198, 199) of the filter-aided sample preparation method (FASP) (201).The samples were mixed with 200µL of 100mM Tris-HCL buffer, pH 8.5 containing 8M urea (UA buffer). The samples were transferred to the top chamber of a 30,000 MWCO cutoff filtration unit (Millipore, part# MRCF0R030) and spun in a microcentrifuge at 14,000G for 10 minutes. An additional 200µL of UA buffer was added and the filter unit was spun at 14,000G

for 15 to 20 minutes. The cysteine residues were alkylated using 100µL of 50mM Iodoacetamide (Pierce, Ref. No. A39271) in UA buffer. Iodoacetamide in UA buffer was added to the top chamber of the filtration unit. The samples were gyrated at 550rpm for 30 minutes in the dark at RT using a Thermomixer (Eppendorf). The filter was spun at 14,000rcf for 15 minutes and the flow through discarded. Unreacted iodoacetamide was washed through the filter with two sequential additions of 200µL of 100mM Tris-HCl buffer, pH 8.5 containing 8M urea and centrifugation at 14,000rcf for 15 to 20 minutes after each buffer addition. The flow through was discarded after each buffer exchange-centrifugation cycle. The urea buffer was exchanged with digestion buffer (DB), 50mM ammonium bicarbonate buffer, pH 8. Two sequential additions of DB (200µL) with centrifugation after each addition to the top chamber was performed. The top filter units were transferred to a new collection tube and 100µL DB containing 1mAU of LysC (Wako Chemicals, cat. no. 129-02541) was added and samples were incubated at 37°C for 2 hours. Trypsin (1µg) (Promega, Cat. No. V5113) was added and samples were incubated overnight at 37°C. The filters were spun at 14,000rcf for 15 minutes to recover the peptides in the lower chamber. The filter was washed with 50µL of 100mM ABC buffer and the wash was combined with the peptides. Residual detergent was removed by ethyl acetate extraction (199, 201). After extraction, the peptides were dried in a Speedvac concentrator (Thermo Scientific, Savant DNA 120 Speedvac Concentrator) for 15 minutes. The dried peptides were dissolved in 1% (vol/vol) TFA and desalted using two micro-tips (porous graphite carbon, BIOMEKNT3CAR) (Glygen) on a Beckman robot (Biomek NX), as previously described (200). The peptides were eluted with 60µL of 60% (vol/vol) MeCN in 0.1% (vol/vol) TFA and dried in a Speed-Vac (Thermo Scientific, Model No. Savant DNA 120 concentrator) after adding TFA to 5% (vol/vol). The peptides were dissolved in 20µL of 1% (vol/vol) MeCNA in water. An

aliquot (10%) was removed for quantification using the Pierce Quantitative Fluorometric Peptide Assay kit (Thermo Scientific, Cat. No. 23290). The remaining peptides were transferred to autosampler vials (Sun-Sri, Cat. No. 200046), dried and stored at -80°C.

### 5.5.15 UPLC-timTOF mass spectrometry

The peptides were analyzed using a nano-Elute chromatograph coupled online to a hybrid trapped ion mobility-quadrupole time of flight mass spectrometer (timsTOF Pro, Bruker Daltonics, Bremen Germany) with a modified nano-electrospray source (CaptiveSpray, Bruker Daltonics). The mass spectrometer was operated in PASEF mode (202). The samples in 1% (vol/vol) aqueous FA were loaded (2µL) onto a 75µm i.d. × 25 cm Aurora Series column with CSI emitter (Ionopticks) on a Bruker nano-ELUTE (Bruker Daltonics). The column temperature was set to 50°C. The column was equilibrated using constant pressure (800 bar) with 8 column volumes of solvent A (0.1% (vol/vol) aqueous FA). Sample loading was performed at constant pressure (800bar) at a volume of 1 x sample pick-up volume plus 2µL. The peptides were eluted using the one column separation mode with a flow rate of 400nL/min and using solvents A and B (0.1% (vol/vol) FA/MeCN): solvent A containing 2% B increased to 15% B over 60 minutes, to 25% B over 30 minutes, to 35% B over 10 min, to 80% B over 10 minutes and constant 80% B for 10 minutes. The MS1 and MS2 spectra were recorded from m/z 100 to 1700. Suitable precursor ions for PASEF-MS/MS were selected in real time from TIMS-MS survey scans by a PASEF scheduling algorithm (202). A polygon filter was applied to the m/z and ion mobility plane to select features most likely representing peptide precursors rather than singly charged background ions. The quadrupole isolation width was set to 2Th for $m/z < 700$ and 3Th for $m/z > 700$, and the collision energy was ramped stepwise as a function of increasing ion mobility: 52eV for 0–19% of the ramp time; 47eV from 19–38%; 42eV from 38–57%; 37eV from 57–76%; and

32eV for the remainder. The TIMS elution voltage was calibrated linearly using the Agilent ESI-L Tuning Mix (m/z 622, 922, 1222).

### 5.5.16 UPLC-Orbitrap mass spectrometry

The samples in formic acid (1%) were loaded (2.5µL) onto a 75µm i.d. × 50 cm Acclaim PepMap 100 C18 RSLC column (Thermo-Fisher Scientific) on an EASY nanoLC (Thermo Fisher Scientific) at a constant pressure of 700bar at 100% A (0.1%FA). Prior to sample loading the column was equilibrated to 100% A for a total of 11µL at 700bar pressure. Peptide chromatography was initiated with mobile phase A (1% FA) containing 2% B (100%ACN, 1%FA) for 5 minutes, then increased to 20% B over 100 minutes, to 32% B over 20 minutes, to 95% B over 1 minute and held at 95% B for 19 minutes, with a flow rate of 300nL/minute. For lower flow rate (250nL/minute), 95% B was held for 29 minutes. The data was acquired in data-dependent acquisition (DDA) mode. The full-scan mass spectra were acquired with the Orbitrap mass analyzer with a scan range of m/z = 325 to 1500 (350 to 1500) and a mass resolving power set to 70,000. Ten data-dependent high-energy collisional dissociations were performed with a mass resolving power set to 17,500, a fixed lower value of m/z 100, an isolation width of 2Da, and a normalized collision energy setting of 27. The maximum injection time was 60ms for parent-ion analysis and product-ion analysis. The target ions that were selected for MS/MS were dynamically excluded for 20 seconds. The automatic gain control (AGC) was set at a target value of 3e6 ions for full MS scans and 1e5 ions for MS2. Peptide ions with charge states of one or > 8 were excluded for HCD acquisition.

### 5.5.17 Identification of proteins

The data from the tims-TOF Data mass spectrometer were converted to peak lists using DataAnalysis (version 5.2, Bruker Daltonics). The MS2 spectra with charges +2, +3 and +4 were

analyzed using Mascot software (203)(Matrix Science, London, UK; version 2.5.1). Mascot was set up to search against a UniProt (ver October 2013) database of mouse proteins (43,296 entries), assuming the digestion enzyme was trypsin with a maximum of 2 missed cleavages allowed. The searches were performed with a fragment ion mass tolerance of 50ppm and a parent ion tolerance of 50ppm. Carbamidomethylation of cysteine was specified in Mascot as a fixed modification. Deamidation of asparagine, deamidation of glutamine, acetylation of protein N-terminus and oxidation of methionine were specified as variable modifications. Peptides and proteins were filtered at 1% false-discovery rate (FDR) by searching against a reversed protein sequence database. MS raw data were converted to peak lists using Proteome Discoverer (version 2.1.0.81, Thermo-Fischer Scientific). MS/MS spectra with charges greater than or equal to two were analyzed using Mascot search engine (203)(Matrix Science, London, UK; version 2.7.0). Mascot was set up to search against a UniProt database of mouse (version October 2013, 43,296 entries), assuming the digestion enzyme was trypsin with a maximum of 4 missed cleavages allowed. The searches were performed with a fragment ion mass tolerance of 0.02Da and a parent ion tolerance of 20ppm. Carbamidomethylation of cysteine was specified in Mascot as a fixed modification. Deamidation of asparagine, formation of pyro-glutamic acid from N-terminal glutamine, acetylation of protein N-terminus and oxidation of methionine were specified as variable modifications. Peptides and proteins were filtered at 1% false-discovery rate (FDR) by searching against a reversed protein sequence database.

### 5.5.18 Mass spectrometry analysis

A cumulative binomial distribution was used to determine which proteins were enriched at a threshold of $P < 0.10$ in the samples containing SVEP1 compared to negative control samples. The probability of success on a single trial was set to the null hypothesis of 0.5. Proteins were

considered “Hits” if they achieved a reproducibility criterion of $P < 0.10$ three controlled experiments and a fourth experiment that lacked an experimental negative control. A meta-analysis was performed on the three independent, controlled experiments using Fisher’s method.

### 5.5.19 Gene cloning

Full length PEAR1: Human *PEAR1* cDNA was obtained from a pDONR221 plasmid (HSCD00863115, DNASU plasmid repository) by PCR and cloned into a modified pCMV6 plasmid (OriGene, Rockville, MD) with a Myc and poly-histidine C-terminal tag. The empty pCMV6 plasmid was used as the empty vector control in experiments. SVEP1 miniTurbo fusion protein (SVEP1-mTID): MiniTurbo cDNA (the promiscuous biotin ligase (186)) was amplified by PCR from the V5-miniTurbo-NES-pCDNA3 plasmid (a gift from Alice Ting, Addgene, plasmid 107170) and cloned downstream of the murine *Svep1* sequence and upstream of the Myc and poly-histidine tag in the pCMV6 plasmid. PEAR1ECD-Bio-His: The plasmid used for the PEAR1 ecto-domain expression was pTT3-PEAR1-bio-His (178) (a gift from Gavin Wright, Addgene plasmid 51860). *Svep1*: cloning of mouse *Svep1* cDNA, protein expression, and purification was described in detail previously (3). Briefly, all proteins were expressed in 293F cells (Invitrogen) and grown in FreeStyle expression media. Plasmids were transfected with 3μg/mL of vector DNA plus 9μg/mL Polyethylenimine (PEI) (25kDa linear PEI, Polysciences, Inc.) at a cell density of $2.5 \times 10^6$ cells/mL. For the PEAR1 ecto-domain biotinylation, 0.3μg/μL of secreted BirA-8his plasmid (a gift from Gavin Wright, Addgene plasmid 32408) was co-transfected and supplemented with 0.1mM biotin. Proteins were purified in an NGC chromatographic system (BioRad Lab) with 5 mL Nuvia IMAC resin (BioRad Lab) and polished using a Superose 6 increase 10/300 column (GE LifeSciences) with PBS as a carrier buffer.

## 5.6 Chapter acknowledgements

This work was supported in part by grants from the National Institutes of Health (NIH) to JSE (T32GM007200, T32HL134635, and F30HL152521), CMH (K08HL135400), NOS (R01HL159171, R01HL131961, UM1HG008853, P01HL151328), by the Longer Life Foundation: A RGA/Washington University Collaboration (LLF 2021-007 to NOS), by the Foundation for Barnes-Jewish Hospital (NOS), and by the Diabetes Research Center at Washington University under NIH award number P30DK020579. Proteomic assays were funded in part by the Washington University Institute of Clinical and Translational Science under NIH award number UL1TR002345. The content is solely the responsibility of the authors and does not necessarily represent the official views of the National Institutes of Health. We thank Dr. Bruce Carter from Vanderbilt University for providing *Pear1*$^{-/-}$ mice. We thank the Washington University School of Medicine diabetes research center mouse phenotyping core for their help with the metabolic phenotyping. The expert technical assistance of Petra Erdmann-Gilmore, Dr. Yiling Mi and Rose Connors is gratefully acknowledged. The proteomic experiments were performed at the Washington University Proteomics Shared Resource (WU-PSR), R Reid Townsend MD, PhD (Director), and Robert Sprung, PhD (Co-Director). The WU-PSR is supported in part by the WU Institute of Clinical and Translational Sciences (NCATS UL1 TR000448), the Mass Spectrometry Research Resource (NIGMS P41 GM103422; R24GM136766) and the Siteman Comprehensive Cancer Center Support Grant (NCI P30 CA091842). The Genotype-Tissue Expression (GTEx) Project was supported by the Common Fund of the Office of the Director of the National Institutes of Health, and by NCI, NHGRI, NHLBI, NIDA, NIMH, and NINDS. The data used for the analyses described in this manuscript were obtained from the GTEx Portal on 10/20/21. Participants in the INTERVAL randomized controlled trial were recruited with the active collaboration of NHS Blood and Transplant

England (www.nhsbt.nhs.uk), which has supported field work and other elements of the trial. DNA extraction and genotyping was co-funded by the National Institute for Health Research (NIHR), the NIHR BioResource (http://bioresource.nihr.ac.uk) and the NIHR [Cambridge Biomedical Research Centre at the Cambridge University Hospitals NHS Foundation Trust]. The INTERVAL study was funded by NHSBT (11-01-GEN). The academic coordinating centre for INTERVAL was supported by core funding from: NIHR Blood and Transplant Research Unit in Donor Health and Genomics (NIHR BTRU-2014-10024), UK Medical Research Council (MR/L003120/1), British Heart Foundation (SP/09/002; RG/13/13/30194; RG/18/13/33946) and the NIHR [Cambridge Biomedical Research Centre at the Cambridge University Hospitals NHS Foundation Trust]. Proteomic assays were funded by the academic coordinating centre for INTERVAL and MRL, Merck & Co., Inc. A complete list of the investigators and contributors to the INTERVAL trial is provided elsewhere (63). The academic coordinating centre would like to thank blood donor centre staff and blood donors for participating in the INTERVAL trial. This work was supported by Health Data Research UK, which is funded by the UK Medical Research Council, Engineering and Physical Sciences Research Council, Economic and Social Research Council, Department of Health and Social Care (England), Chief Scientist Office of the Scottish Government Health and Social Care Directorates, Health and Social Care Research and Development Division (Welsh Government), Public Health Agency (Northern Ireland), British Heart Foundation and Wellcome. The views expressed are those of the authors and not necessarily those of the NHS, the NIHR or the Department of Health and Social Care.

# Chapter 6

# Future directions

## 6.1 Introduction

The first robust association between SVEP1 and human disease was described in 2016 (6). Significant progress has been made since then in understanding this protein and how it relates to disease. Many basic questions about SVEP1 remain, however. This chapter outlines the gaps in our knowledge and the most pressing questions about SVEP1 and its contribution to human disease.

## 6.2 Determine the location of SVEP1 in situ

One of the most important and unanswered questions regarding SVEP1 is where it is contained within tissue. Transcription-based technologies have provided insight into which tissues and cell-types express the gene (3, 25), but the localization of the protein is more difficult to determine. As an ECM protein, SVEP1 may be integrated within a specific region of the heterogeneous matrix. Determination of where SVEP1 is integrated would bring clarity to it interactions and function. Several studies have claimed to identify SVEP1 using antibodies raised against the protein, but none have reported the appropriate controls (2, 31). These controls are critical for antibody validation and undermine the reports. This is of particular concern for SVEP1, since it is comprised primarily of domains that are contained within other proteins.

There are several ways to resolve this question. This first approach is to generate and/or rigorously characterize an antibody that recognizes SVEP1 within tissue sections (61). Another approach may be to generate an animal model with a conditional allele that codes for tagged

SVEP1. The insertion of a tag could disrupt protein function, but its detection may be more specific than other approaches. This reagent would also enable studies about the spatiotemporal nature of SVEP1 production and degradation. In addition, this approach could provide insight into which tissues are the source of plasma SVEP1. Additional approaches may also be considered, including developing a traceable small molecule with high affinity and specificity for SVEP1. A tagged DNA aptamer that recognizes SVEP1 could also be used for this purpose.

## 6.3 Characterize the molecular mechanisms by which SVEP1 influences cells

The work of our lab and others has built a small body of knowledge about the molecular mechanisms of SVEP1. Various SVEP1 binding partners have been proposed and/or validated, and SVEP1 can influence several signaling pathways. Despite the progress in understanding SVEP1's molecular mechanisms, the details remain unclear. Many of the proposed binding partners have not yet been rigorously tested, for example. Given the size and composition of SVEP1, it is likely the protein contains numerous binding partners. Determining the precise mechanism of SVEP1's influence on cells may be complicated by this factor. Regardless, there are several mechanistic hypotheses that have yet to be explored regarding SVEP1's molecular mechanisms. Structure-function studies and knockout models will be critical in deciphering the answers to this question.

## 6.4 Characterize the tissue-level mechanisms related to SVEP1's causal association with disease

We are beginning to understand the molecular mechanisms and cellular effects of SVEP1, but how this leads to disease remains unclear. It is plausible that the molecular mechanisms underlying SVEP1's disease associations may be conserved between different diseases, but the effects on various tissues may manifest differently. Given that SVEP1 promotes AKT/mTOR

signaling, one might speculate that SVEP1 promotes cellular senescence in tissues that contain the protein (58). Animal models and a deeper understanding of SVEP1's molecular interactions will be critical in exploring these questions. The diseases associated with SVEP1 tend to be chronic and manifest in mid to late life, presenting a challenge to experimental investigation.

## 6.5 Interrogate the contribution of SVEP1 to additional traits and diseases

Our investigation of SVEP1 has focused on characterizing its role in atherosclerosis, T2D, and platelet phenotypes (3). Additional studies have described the contribution of SVEP1 to vascular development (25, 26, 28) and to a lesser extent, glaucoma (27). SVEP1's role in several additional diseases with which it is associated have not been reported. These are described in Chapter 1 and include heart failure, dementia, and longevity. Understanding how SVEP1 contributes to these traits and diseases is important in its own respect but holds the potential to reveal shared mechanisms underlying SVEP1's impact on biology. Broadening our understanding of SVEP1 is also important to our evaluation of its therapeutic potential, as discussed below.

## 6.6 Evaluate the therapeutic potential of SVEP1

SVEP1 causally relates to disease and exists within the extracellular space. This makes the protein an intriguing candidate for therapeutic intervention. One limitation to targeting SVEP1 is its critical role in development. However, most of the diseases associated with SVEP1 are chronic and may be addressed after development or risk of pregnancy. Genetically encoded plasma levels of SVEP1 vary within populations (3), suggesting a safe therapeutic window exists to target the protein. Similarly, we have not detected any negative effects after constitutive deletion of a single *Svep1* allele in mice. Biallelic loss of *Svep1* post-development also appears to

be well-tolerated in mice. A more thorough phenotyping of mice lacking SVEP1 will be important, especially of organ systems related to the disease associations of SVEP1. It would be prudent to determine the long-term effects of SVEP1 depletion on lymphatic function, ocular pressure, hematopoiesis, and neurodegeneration, for example.

One challenge to evaluating the therapeutic potential of blocking SVEP1 is our limited understanding of how it promotes disease. If SVEP1 functions through interactions with a multitude of binding partners, for example, then the entire protein may need to be inhibited. Conversely, if SVEP1 promotes disease primarily through a specific interaction or region of the protein, then blocking that region of the protein may be sufficient to confer protection. It is also not clear which tissues govern SVEP1's pathogenic effects since plasma levels of the protein may reflect its composition within tissue. Once again, studies in animal models should yield answers to these questions and provide insight into the therapeutic potential of targeting SVEP1.

## 6.7 Develop therapeutic approaches to block SVEP1 function

Therapeutic approaches to block SVEP1 function should be explored. A biologic approach, such as monoclonal antibody inhibition, is one feasible approach. It may be possible to develop a highly specific anti-SVEP1 antibody to functionally block the protein or target it for degradation, for example. This approach has several benefits and has been employed to inhibit proteins within the extracellular space (204). One potential limitation is that an antibody may not have access to SVEP1 at its disease-relevant position within tissue.

Another therapeutic approach is through a small molecule inhibitor of SVEP1 or its interactions. This approach may avoid the potential issues related to accessibility that could limit a biologic approach. Perhaps the most promising approach to small molecule inhibition of SVEP1 would be

to disrupt the interaction between SVEP1 and PEAR1. We have successfully produced recombinant SVEP1 and PEAR1 proteins and validated their interaction. This enables a variety of small molecule screening approaches to identify a small molecule that disrupts their interaction. Other approaches to pharmaceutically inhibit SVEP1 may also be considered as we gain a deeper understanding of how this interesting protein promotes disease.

## 6.8 Conclusions

Described herein is the current state of our knowledge regarding SVEP1 and its causal role in human disease. The coming of age of aptamer-based proteomics and the ability to generate robust instrumental variables that correspond to SVEP1 exposure will likely lead to the discovery of additional causal associations between SVEP1 and human traits and disease. The current constellation of diseases associated with SVEP1 is nonetheless stunning. The challenge for future investigation will be to rigorously define how SVEP1 influences disease. Given the common thread of chronicity among diseases associated with SVEP1, it is likely that there is a shared mechanistic process. The questions raised by this research provides a novel lens to interrogate the chronic disease crisis that defines human health at this point in history.

# References


1. Gilges D, Vinit MA, Callebaut I, Coulombel L, Cacheux V, Romeo PH, et al. Polydom: a secreted protein with pentraxin, complement control protein, epidermal growth factor and von Willebrand factor A domains. *Biochem J.* 2000;352 Pt 1:49-59.

2. Sato-Nishiuchi R, Nakano I, Ozawa A, Sato Y, Takeichi M, Kiyozumi D, et al. Polydom/SVEP1 is a ligand for integrin α9β1. *Journal of Biological Chemistry.* 2012;287(30):25615-30.

3. Jung I-H, Elenbaas JS, Alisio A, Santana K, Young EP, Kang CJ, et al. SVEP1 is a human coronary artery disease locus that promotes atherosclerosis. *Science Translational Medicine.* 2021;13(586):eabe0357.

4. Sun BB, Maranville JC, Peters JE, Stacey D, Staley JR, Blackshaw J, et al. Genomic atlas of the human plasma proteome. *Nature.* 2018;558(7708):73-9.

5. Zhang Y, Mao Y, Zhao W, Su T, Zhong Y, Fu L, et al. Glyco-CPLL: An Integrated Method for In-Depth and Comprehensive N-Glycoproteome Profiling of Human Plasma. *Journal of Proteome Research.* 2020;19(2):655-66.

6. Stitziel NO, Stirrups KE, Masca NG, Erdmann J, Ferrario PG, Konig IR, et al. Coding Variation in ANGPTL4, LPL, and SVEP1 and the Risk of Coronary Disease. *N Engl J Med.* 2016;374(12):1134-44.

7. Emilsson V, Gudmundsdottir V, Gudjonsson A, Jonmundsson T, Jonsson BG, Karim MA, et al. Coding and regulatory variants are associated with serum protein levels and disease. *Nature Communications.* 2022;13(1):481.

8. Ortiz-Fernández L, Saruhan-Direskeneli G, Alibaz-Oner F, Kaymaz-Tahra S, Coit P, Kong X, et al. Identification of susceptibility loci for Takayasu arteritis through a large multi-ancestral genome-wide association study. *The American Journal of Human Genetics.* 2021;108(1):84-99.

9. Williams SA, Ostroff R, Hinterberg MA, Coresh J, Ballantyne CM, Matsushita K, et al. A proteomic surrogate for cardiovascular outcomes that is sensitive to multiple mechanisms of change in risk. *Science Translational Medicine.* 2022;14(639):eabj9625.

10. Pernemalm M, Sandberg A, Zhu Y, Boekel J, Tamburro D, Schwenk JM, et al. In-depth human plasma proteome analysis captures tissue proteins and transfer of protein variants across the placenta. *Elife.* 2019;8.

11. Gharahkhani P, Jorgenson E, Hysi P, Khawaja AP, Pendergrass S, Han X, et al. Genome-wide meta-analysis identifies 127 open-angle glaucoma loci with consistent effect across ancestries. *Nature communications.* 2021;12(1):1-16.

12. Young TL, Whisenhunt KN, Jin J, LaMartina SM, Martin SM, Souma T, et al. SVEP1 as a genetic modifier of TEK-related primary congenital glaucoma. *Investigative ophthalmology & visual science.* 2020;61(12):6-.

13. Walker KA, Chen J, Zhang J, Fornage M, Yang Y, Zhou L, et al. Large-scale plasma proteomic analysis identifies proteins and pathways associated with dementia risk. *Nature Aging.* 2021;1(5):473-89.

14. Sebastiani P, Federico A, Morris M, Gurinovich A, Tanaka T, Chandler KB, et al. Protein signatures of centenarians and their offspring suggest centenarians age slower than other humans. *Aging cell.* 2021;20(2):e13290.

15. Lindbohm JV, Mars N, Walker KA, Singh-Manoux A, Livingston G, Brunner EJ, et al. Plasma proteins, cognitive decline, and 20-year risk of dementia in the Whitehall II and Atherosclerosis Risk in Communities studies. *Alzheimer's & Dementia.* 2022;18(4):612-24.

16. Lehallier B, Gate D, Schaum N, Nanasi T, Lee SE, Yousef H, et al. Undulating changes in human plasma proteome profiles across the lifespan. *Nature Medicine.* 2019;25(12):1843-50.

17. Perrot N, Pelletier W, Bourgault J, Couture C, Li Z, Mitchell PL, et al. A trans-omic Mendelian randomization study of parental lifespan uncovers novel aging biology and therapeutic candidates for chronic diseases. *Aging Cell.* 2021;20(11):e13497.

18. Keramati AR, Chen M-H, Rodriguez BA, Yanek LR, Bhan A, Gaynor BJ, et al. Genome sequencing unveils a regulatory landscape of platelet reactivity. *Nature Communications.* 2021;12(1):1-13.

19. Chen MH, Raffield LM, Mousas A, Sakaue S, Huffman JE, Moscati A, et al. Trans-ethnic and Ancestry-Specific Blood-Cell Genetics in 746,667 Individuals from 5 Global Populations. *Cell.* 2020;182(5):1198-213.e14.

20. Kuchenbaecker K, Gilly A, Suveges D, Southam L, Giannakopoulou O, Kilian B, et al. Insights into the genetic architecture of haematological traits from deep phenotyping and whole-genome sequencing for two Mediterranean isolated populations. *Scientific Reports.* 2022;12(1):1131.

21. Nakada T-a, Russell JA, Boyd JH, Thair SA, and Walley KR. Identification of a Nonsynonymous Polymorphism in the SVEP1 Gene Associated With Altered Clinical Outcomes in Septic Shock*. *Critical Care Medicine.* 2015;43(1):101-8.

22. Luxán G, and Dimmeler S. The vasculature: a therapeutic target in heart failure? *Cardiovascular Research.* 2022;118(1):53-64.

23. Allingham RR, de Kater AW, and Ethier RC. Schlemm 's Canal and Primary Open Angle Glaucoma: Correlation Between Schlemm 's Canal Dimensions and Outflow Facility. *Experimental Eye Research.* 1996;62(1):101-10.

24. O'Brien JT, and Thomas A. Vascular dementia. *The Lancet.* 2015;386(10004):1698-706.

25. Karpanen T, Padberg Y, Pavert SAvd, Dierkes C, Morooka N, Peterson-Maduro J, et al. An Evolutionarily Conserved Role for Polydom/Svep1 During Lymphatic Vessel Formation. *Circulation Research.* 2017;120(8):1263-75.

26. Morooka N, Futaki S, Sato-Nishiuchi R, Nishino M, Totani Y, Shimono C, et al. Polydom Is an Extracellular Matrix Protein Involved in Lymphatic Vessel Remodeling. *Circ Res.* 2017;120(8):1276-88.

27. Thomson BR, Liu P, Onay T, Du J, Tompson SW, Misener S, et al. Cellular crosstalk regulates the aqueous humor outflow pathway and provides new targets for glaucoma therapies. *Nature communications.* 2021;12(1):1-16.

28. Coxam B, Collins RT, Hußmann M, Huisman Y, Meier K, Jung S, et al. Svep1 stabilises developmental vascular anastomosis in reduced flow conditions. *Development.* 2022;149(6).

29. Armstrong DL, McGowen MR, Weckle A, Pantham P, Caravas J, Agnew D, et al. The core transcriptome of mammalian placentas and the divergence of expression with placental shape. *Placenta.* 2017;57:71-8.

30. Karczewski KJ, Francioli LC, Tiao G, Cummings BB, Alföldi J, Wang Q, et al. The mutational constraint spectrum quantified from variation in 141,456 humans. *Nature.* 2020;581(7809):434-43.

31. Winkler MJ, Müller P, Sharifi AM, Wobst J, Winter H, Mokry M, et al. Functional investigation of the coronary artery disease gene SVEP1. *Basic Research in Cardiology.* 2020;115(6):67.

32. Maeda N, Johnson L, Kim S, Hagaman J, Friedman M, and Reddick R. Anatomical differences and atherosclerosis in apolipoprotein E-deficient mice with 129/SvEv and C57BL/6 genetic backgrounds. *Atherosclerosis.* 2007;195(1):75-82.

33. Man JJ, Beckman JA, and Jaffe IZ. Sex as a Biological Variable in Atherosclerosis. *Circ Res.* 2020;126(9):1297-319.

34. Handford PA, Mayhew M, Baron M, Winship PR, Campbell ID, and Brownlee GG. Key residues involved in calcium-binding motifs in EGF-like domains. *Nature.* 1991;351(6322):164-7.

35. Whittaker CA, and Hynes RO. Distribution and evolution of von Willebrand/integrin A domains: widely dispersed domains with roles in cell adhesion and elsewhere. *Molecular biology of the cell.* 2002;13(10):3369-87.

36. Blum M, Chang H-Y, Chuguransky S, Grego T, Kandasaamy S, Mitchell A, et al. The InterPro protein families and domains database: 20 years on. *Nucleic acids research.* 2021;49(D1):D344-D54.

37. Tuckwell D. Evolution of von Willebrand factor A (VWA) domains. *Biochemical Society Transactions.* 1999;27(6):835-40.

38. Norman DG, Barlow PN, Baron M, Day AJ, Sim RB, and Campbell ID. Three-dimensional structure of a complement control protein module in solution. *J Mol Biol.* 1991;219(4):717-25.

39. Callebaut I, Gilgès D, Vigon I, and Mornon JP. HYR, an extracellular module involved in cellular adhesion and related to the immunoglobulin-like fold. *Protein Sci.* 2000;9(7):1382-90.

40. The UniProt C. UniProt: the universal protein knowledgebase in 2021. *Nucleic Acids Research.* 2021;49(D1):D480-D9.

41. Zhang Y, Mao Y, Zhao W, Su T, Zhong Y, Fu L, et al. Glyco-CPLL: An Integrated Method for In-Depth and Comprehensive N-Glycoproteome Profiling of Human Plasma. *J Proteome Res.* 2020;19(2):655-66.

42. Halim A, Nilsson J, Rüetschi U, Hesse C, and Larson G. Human urinary glycoproteomics; attachment site specific analysis of N- and O-linked glycosylations by CID and ECD. *Mol Cell Proteomics.* 2012;11(4):M111.013649.

43. Takada Y, Ye X, and Simon S. The integrins. *Genome Biol.* 2007;8(5):215.

44. Palmer EL, Rüegg C, Ferrando R, Pytela R, and Sheppard D. Sequence and tissue distribution of the integrin alpha 9 subunit, a novel partner of beta 1 that is widely distributed in epithelia and muscle. *Journal of Cell Biology.* 1993;123(5):1289-97.

45. Bazigou E, Xie S, Chen C, Weston A, Miura N, Sorokin L, et al. Integrin-α9 Is Required for Fibronectin Matrix Assembly during Lymphatic Valve Morphogenesis. *Developmental Cell.* 2009;17(2):175-86.

46. Thomas DS, Carolin S, Mike E, Harald A, Konstanze G, Claudia AM, et al. The integrin α9β1 on hematopoietic stem and progenitor cells: involvement in cell adhesion, proliferation and differentiation. *Haematologica.* 2009;94(11):1493-501.

47. Huang XZ, Wu JF, Ferrando R, Lee JH, Wang YL, Farese RV, Jr., et al. Fatal bilateral chylothorax in mice lacking the integrin alpha9beta1. *Mol Cell Biol.* 2000;20(14):5208-15.

48. Vandenbriele C, Kauskot A, Vandersmissen I, Criel M, Geenens R, Craps S, et al. Platelet endothelial aggregation receptor-1: a novel modifier of neoangiogenesis. *Cardiovasc Res.* 2015;108(1):124-38.

49. Nanda N, Bao M, Lin H, Clauser K, Komuves L, Quertermous T, et al. Platelet endothelial aggregation receptor 1 (PEAR1), a novel epidermal growth factor repeat-containing transmembrane receptor, participates in platelet contact-induced activation. *J Biol Chem.* 2005;280(26):24680-9.

50. Kauskot A, Di Michele M, Loyen S, Freson K, Verhamme P, and Hoylaerts MF. A novel mechanism of sustained platelet αIIbβ3 activation via PEAR1. *Blood.* 2012;119(17):4056-65.

51. Kauskot A, Vandenbriele C, Louwette S, Gijsbers R, Tousseyn T, Freson K, et al. PEAR1 attenuates megakaryopoiesis via control of the PI3K/PTEN pathway. *Blood.* 2013;121(26):5208-17.

52. Woulfe DS. Akt signaling in platelets and thrombosis. *Expert Rev Hematol.* 2010;3(1):81-91.

53. Huang X, Liu G, Guo J, and Su Z. The PI3K/AKT pathway in obesity and type 2 diabetes. *Int J Biol Sci.* 2018;14(11):1483-96.

54. Zhao Y, Qian Y, Sun Z, Shen X, Cai Y, Li L, et al. Role of PI3K in the Progression and Regression of Atherosclerosis. *Frontiers in Pharmacology.* 2021;12.

55. Aslan JE, Tormoen GW, Loren CP, Pang J, and McCarty OJT. S6K1 and mTOR regulate Rac1-driven platelet activation and aggregation. *Blood.* 2011;118(11):3129-36.

56. Saxton RA, and Sabatini DM. mTOR Signaling in Growth, Metabolism, and Disease. *Cell.* 2017;168(6):960-76.

57. Sciarretta S, Forte M, Frati G, and Sadoshima J. New insights into the role of mTOR signaling in the cardiovascular system. *Circulation research.* 2018;122(3):489-505.

58. Weichhart T. mTOR as Regulator of Lifespan, Aging, and Cellular Senescence: A Mini-Review. *Gerontology.* 2018;64(2):127-34.

59. Kumar V, Evans LC, Kurth T, Yang C, Wollner C, Nasci V, et al. Therapeutic suppression of mTOR (mammalian target of rapamycin) signaling prevents and reverses salt-induced hypertension and kidney injury in Dahl salt-sensitive rats. *Hypertension.* 2019;73(3):630-9.

60. Huber S, Bruns CJ, Schmid G, Hermann PC, Conrad C, Niess H, et al. Inhibition of the mammalian target of rapamycin impedes lymphangiogenesis. *Kidney Int.* 2007;71(8):771-7.

61. Uhlen M, Bandrowski A, Carr S, Edwards A, Ellenberg J, Lundberg E, et al. A proposal for validation of antibodies. *Nature Methods.* 2016;13(10):823-7.

62. Ojha H, Ghosh P, Singh Panwar H, Shende R, Gondane A, Mande SC, et al. Spatially conserved motifs in complement control protein domains determine functionality in

regulators of complement activation-family proteins. *Communications Biology.* 2019;2(1):290.

63. Di Angelantonio E, Thompson SG, Kaptoge S, Moore C, Walker M, Armitage J, et al. Efficiency and safety of varying the frequency of whole blood donation (INTERVAL): a randomised trial of 45 000 donors. *Lancet.* 2017;390(10110):2360-71.

64. Ferkingstad E, Sulem P, Atlason BA, Sveinbjornsson G, Magnusson MI, Styrmisdottir EL, et al. Large-scale integration of the plasma proteome with genetics and disease. *Nat Genet.* 2021;53(12):1712-21.

65. Weber C, and Noels H. Atherosclerosis: current pathogenesis and therapeutic options. *Nat Med.* 2011;17(11):1410-22.

66. Dzau VJ, Braun-Dullaeus RC, and Sedding DG. Vascular proliferation and atherosclerosis: new perspectives and therapeutic strategies. *Nat Med.* 2002;8(11):1249-56.

67. Liu X, and Ntambi JM. Atherosclerosis: keep your macrophages in shape. *Nat Med.* 2009;15(12):1357-8.

68. Hansson GK, and Klareskog L. Pulling down the plug on atherosclerosis: cooling down the inflammasome. *Nat Med.* 2011;17(7):790-1.

69. Ross R. Genetically modified mice as models of transplant atherosclerosis. *Nat Med.* 1996;2(5):527-8.

70. Randolph GJ. Proliferating macrophages prevail in atherosclerosis. *Nat Med.* 2013;19(9):1094-5.

71. Rader DJ, and FitzGerald GA. State of the art: atherosclerosis in a limited edition. *Nat Med.* 1998;4(8):899-900.

72. Virella G, and Lopes-Virella MF. Humoral immunity and atherosclerosis. *Nat Med.* 2003;9(3):243-4; author reply 4-5.

73. C Baigent AK, P M Kearney, L Blackwell, G Buck, C Pollicino, A Kirby, T Sourjina, R Peto, R Collins, R Simes, Cholesterol Treatment Trialists' (CTT) Collaborators. Efficacy and Safety of Cholesterol-Lowering Treatment: Prospective Meta-Analysis of Data From 90,056 Participants in 14 Randomised Trials of Statins. *Lancet.* 2005;366:1267-78.

74. van der Harst P, and Verweij N. Identification of 64 Novel Genetic Loci Provides an Expanded View on the Genetic Architecture of Coronary Artery Disease. *Circulation research.* 2018;122(3):433-43.

75. Shur I, Socher R, Hameiri M, Fried A, and Benayahu D. Molecular and cellular characterization of SEL-OB/SVEP1 in osteogenic cells in vivo and in vitro. *J Cell Physiol.* 2006;206(2):420-7.

76. Sato-Nishiuchi R, Nakano I, Ozawa A, Sato Y, Takeichi M, Kiyozumi D, et al. Polydom/SVEP1 is a ligand for integrin alpha9beta1. *J Biol Chem.* 2012;287(30):25615-30.

77. Levy D, Ehret GB, Rice K, Verwoert GC, Launer LJ, Dehghan A, et al. Genome-wide association study of blood pressure and hypertension. *Nat Genet.* 2009;41(6):677-87.

78. Takeuchi F, Isono M, Katsuya T, Yamamoto K, Yokota M, Sugiyama T, et al. Blood pressure and hypertension are associated with 7 loci in the Japanese population. *Circulation.* 2010;121(21):2302-9.

79. Karpanen T, Padberg Y, van de Pavert SA, Dierkes C, Morooka N, Peterson-Maduro J, et al. An Evolutionarily Conserved Role for Polydom/Svep1 During Lymphatic Vessel Formation. *Circulation research.* 2017;120(8):1263-75.

80. Samuelov L, Li Q, Bochner R, Najor NA, Albrecht L, Malchin N, et al. SVEP1 plays a crucial role in epidermal differentiation. *Exp Dermatol.* 2017;26(5):423-30.

81. Cangemi C, Skov V, Poulsen MK, Funder J, Twal WO, Gall MA, et al. Fibulin-1 is a marker for arterial extracellular matrix alterations in type 2 diabetes. *Clin Chem.* 2011;57(11):1556-65.

82. Ayari H, and Bricca G. Identification of two genes potentially associated in iron-heme homeostasis in human carotid plaque using microarray analysis. *J Biosci.* 2013;38(2):311-5.

83. Kalluri AS, Vellarikkal SK, Edelman ER, Nguyen L, Subramanian A, Ellinor PT, et al. Single-Cell Analysis of the Normal Mouse Aorta Reveals Functionally Distinct Endothelial Cell Populations. *Circulation.* 2019;140(2):147-63.

84. Bennett MR, Sinha S, and Owens GK. Vascular Smooth Muscle Cells in Atherosclerosis. *Circ Res.* 2016;118(4):692-702.

85. Wei Li MF, Sekhar P Reddy, Dae-Yeul Yu, Masayuki Yamamoto, Roy L Silverstein. CD36 Participates in a Signaling Pathway That Regulates ROS Formation in Murine VSMCs. *J Clin Invest.* 2010;120:3996-4006.

86. Majesky MW. Developmental basis of vascular smooth muscle diversity. *Arterioscler Thromb Vasc Biol.* 2007;27(6):1248-58.

87. Burgess S, Scott RA, Timpson NJ, Davey Smith G, Thompson SG, and Consortium E-I. Using published data in Mendelian randomization: a blueprint for efficient identification of causal risk factors. *European journal of epidemiology.* 2015;30(7):543-52.

88. Weng S, Zemany L, Standley KN, Novack DV, La Regina M, Bernal-Mizrachi C, et al. Beta3 integrin deficiency promotes atherosclerosis and pulmonary inflammation in high-fat-fed, hyperlipidemic mice. *Proc Natl Acad Sci U S A.* 2003;100(11):6730-5.

89. Misra A, Feng Z, Chandran RR, Kabir I, Rotllan N, Aryal B, et al. Integrin beta3 regulates clonality and fate of smooth muscle-derived atherosclerotic plaque cells. *Nat Commun.* 2018;9(1):2073.

90. Schreiber TD, Steinl C, Essl M, Abele H, Geiger K, Muller CA, et al. The integrin alpha9beta1 on hematopoietic stem and progenitor cells: involvement in cell adhesion, proliferation and differentiation. *Haematologica.* 2009;94(11):1493-501.

91. Chen C, Kudo M, Rutaganira F, Takano H, Lee C, Atakilit A, et al. Integrin alpha9beta1 in airway smooth muscle suppresses exaggerated airway narrowing. *J Clin Invest.* 2012;122(8):2916-27.

92. Danussi C, Petrucco A, Wassermann B, Pivetta E, Modica TM, Del Bel Belluz L, et al. EMILIN1-alpha4/alpha9 integrin interaction inhibits dermal fibroblast and keratinocyte proliferation. *The Journal of cell biology.* 2011;195(1):131-45.

93. Gupta SK, and Vlahakis NE. Integrin alpha9beta1: Unique signaling pathways reveal diverse biological roles. *Cell Adh Migr.* 2010;4(2):194-8.

94. Kanayama M, Kurotaki D, Morimoto J, Asano T, Matsui Y, Nakayama Y, et al. Alpha9 integrin and its ligands constitute critical joint microenvironments for development of autoimmune arthritis. *J Immunol.* 2009;182(12):8015-25.

95. Mostovich LA, Prudnikova TY, Kondratov AG, Loginova D, Vavilov PV, Rykova VI, et al. Integrin alpha9 (ITGA9) expression and epigenetic silencing in human breast tumors. *Cell Adh Migr.* 2011;5(5):395-401.

96. Roy S, Bingle L, Marshall JF, Bass R, Ellis V, Speight PM, et al. The role of alpha9beta1 integrin in modulating epithelial cell behaviour. *J Oral Pathol Med.* 2011;40(10):755-61.

97. Johnson JL. Emerging regulators of vascular smooth muscle cell function in the development and progression of atherosclerosis. *Cardiovascular research.* 2014;103(4):452-60.

98. Mitchell AL, Attwood TK, Babbitt PC, Blum M, Bork P, Bridge A, et al. InterPro in 2019: improving coverage, classification and access to protein sequence annotations. *Nucleic Acids Res.* 2019;47(D1):D351-D60.

99. Sonnhammer EL, and Ostlund G. InParanoid 8: orthology analysis between 273 proteomes, mostly eukaryotic. *Nucleic Acids Res.* 2015;43(Database issue):D234-9.

100. Marchler-Bauer A, Lu S, Anderson JB, Chitsaz F, Derbyshire MK, DeWeese-Scott C, et al. CDD: a Conserved Domain Database for the functional annotation of proteins. *Nucleic Acids Res.* 2011;39(Database issue):D225-9.

101. Zhang L, and Ward REt. uninflatable encodes a novel ectodermal apical surface protein required for tracheal inflation in Drosophila. *Dev Biol.* 2009;336(2):201-12.

102. Ghabrial AS, and Krasnow MA. Social interactions among epithelial cells during tracheal branching morphogenesis. *Nature.* 2006;441(7094):746-9.

103. Loubery S, Seum C, Moraleda A, Daeden A, Furthauer M, and Gonzalez-Gaitan M. Uninflatable and Notch control the targeting of Sara endosomes during asymmetric division. *Curr Biol.* 2014;24(18):2142-8.

104. Xie G, Zhang H, Du G, Huang Q, Liang X, Ma J, et al. Uif, a large transmembrane protein with EGF-like repeats, can antagonize Notch signaling in Drosophila. *PLoS One.* 2012;7(4):e36362.

105. Davis-Knowlton J, Turner JE, Turner A, Damian-Loring S, Hagler N, Henderson T, et al. Characterization of smooth muscle cells from human atherosclerotic lesions and their responses to Notch signaling. *Lab Invest.* 2019;99(3):290-304.

106. Schweisguth F. Regulation of notch signaling activity. *Curr Biol.* 2004;14(3):R129-38.

107. Deford P, Brown K, Richards RL, King A, Newburn K, Westover K, et al. MAGP2 controls Notch via interactions with RGD binding integrins: Identification of a novel ECM-integrin-Notch signaling axis. *Exp Cell Res.* 2016;341(1):84-91.

108. Chen PY, Qin L, Li G, Tellides G, and Simons M. Smooth muscle FGF/TGFbeta cross talk regulates atherosclerosis progression. *EMBO molecular medicine.* 2016;8(7):712-28.

109. Shang T, Yednock T, and Issekutz AC. alpha9beta1 integrin is expressed on human neutrophils and contributes to neutrophil migration through human lung and synovial fibroblast barriers. *J Leukoc Biol.* 1999;66(5):809-16.

110. Chistiakov DA, Bobryshev YV, and Orekhov AN. Changes in transcriptome of macrophages in atherosclerosis. *J Cell Mol Med.* 2015;19(6):1163-73.

111. Young EP, and Stitziel NO. Capitalizing on Insights from Human Genetics to Identify Novel Therapeutic Targets for Coronary Artery Disease. *Annu Rev Med.* 2019;70:19-32.

112. Basatemur GL, Jorgensen HF, Clarke MCH, Bennett MR, and Mallat Z. Vascular smooth muscle cells in atherosclerosis. *Nat Rev Cardiol.* 2019;16(12):727-44.

113. Wirka RC, Wagh D, Paik DT, Pjanic M, Nguyen T, Miller CL, et al. Atheroprotective roles of smooth muscle cell phenotypic modulation and the TCF21 disease gene as revealed by single-cell analysis. *Nat Med.* 2019;25(8):1280-9.

114. Bauer RC, Tohyama J, Cui J, Cheng L, Yang J, Zhang X, et al. Knockout of Adamts7, a novel coronary artery disease locus in humans, reduces atherosclerosis in mice. *Circulation.* 2015;131(13):1202-13.

115. Shankman LS, Gomez D, Cherepanova OA, Salmon M, Alencar GF, Haskins RM, et al. KLF4-dependent phenotypic modulation of smooth muscle cells has a key role in atherosclerotic plaque pathogenesis. *Nat Med.* 2015;21(6):628-37.

116. Liu B, Pjanic M, Wang T, Nguyen T, Gloudemans M, Rao A, et al. Genetic Regulatory Mechanisms of Smooth Muscle Cells Map to Coronary Artery Disease Risk Loci. *Am J Hum Genet.* 2018;103(3):377-88.

117. Fukuda D, Aikawa E, Swirski FK, Novobrantseva TI, Kotelianski V, Gorgun CZ, et al. Notch ligand delta-like 4 blockade attenuates atherosclerosis and metabolic disorders. *Proc Natl Acad Sci U S A.* 2012;109(27):E1868-77.

118. Boucher J, Gridley T, and Liaw L. Molecular pathways of notch signaling in vascular smooth muscle cells. *Front Physiol.* 2012;3:81.

119. Cherepanova OA, Gomez D, Shankman LS, Swiatlowska P, Williams J, Sarmento OF, et al. Activation of the pluripotency factor OCT4 in smooth muscle cells is atheroprotective. *Nat Med.* 2016;22(6):657-65.

120. Sundstrom J, and Vasan RS. Circulating biomarkers of extracellular matrix remodeling and risk of atherosclerotic events. *Curr Opin Lipidol.* 2006;17(1):45-53.

121. Langley SR, Willeit K, Didangelos A, Matic LP, Skroblin P, Barallobre-Barreiro J, et al. Extracellular matrix proteomics identifies molecular signature of symptomatic carotid plaques. *J Clin Invest.* 2017;127(4):1546-60.

122. Andrews MR, Czvitkovich S, Dassie E, Vogelaar CF, Faissner A, Blits B, et al. Alpha9 integrin promotes neurite outgrowth on tenascin-C and enhances sensory axon regeneration. *J Neurosci.* 2009;29(17):5546-57.

123. Hakkinen L, Hildebrand HC, Berndt A, Kosmehl H, and Larjava H. Immunolocalization of tenascin-C, alpha9 integrin subunit, and alphavbeta6 integrin during wound healing in human oral mucosa. *J Histochem Cytochem.* 2000;48(7):985-98.

124. Smith LL, Cheung HK, Ling LE, Chen J, Sheppard D, Pytela R, et al. Osteopontin N-terminal domain contains a cryptic adhesive sequence recognized by alpha9beta1 integrin. *J Biol Chem.* 1996;271(45):28485-91.

125. Nishimichi N, Higashikawa F, Kinoh HH, Tateishi Y, Matsuda H, and Yokosaki Y. Polymeric osteopontin employs integrin alpha9beta1 as a receptor and attracts neutrophils by presenting a de novo binding site. *J Biol Chem.* 2009;284(22):14769-76.

126. Kessler T ZL, Liu Z, Yin X, Huang Y, Wang Y, Fu Y, Mayr M, Ge Q, Xu Q, Zhu Y, Wang X, Schmidt K, de Wit C, Erdmann J, Schunkert H, Aherrahrou Z, Kong W. ADAMTS-7 inhibits re-endothelialization of injured arteries and promotes vascular remodeling through cleavage of thrombospondin-1. *Circulation.* 2015;131:1191-201.

127. Alexander MR, and Owens GK. Epigenetic Control of Smooth Muscle Cell Differentiation and Phenotypic Switching in Vascular Development and Disease. *Annual Review of Physiology.* 2012;74(1):13-40.

128. Benditt EP, and Benditt JM. Evidence for a monoclonal origin of human atherosclerotic plaques. *Proceedings of the National Academy of Sciences.* 1973;70(6):1753-6.

129. Grootaert MOJ, and Bennett MR. Vascular smooth muscle cells in atherosclerosis: time for a re-assessment. *Cardiovascular Research.* 2021;117(11):2326-39.

130. Seita J, and Weissman IL. Hematopoietic stem cell: self-renewal versus differentiation. *Wiley Interdisciplinary Reviews: Systems Biology and Medicine.* 2010;2(6):640-53.

131. Desiere F, Deutsch EW, King NL, Nesvizhskii AI, Mallick P, Eng J, et al. The PeptideAtlas project. *Nucleic Acids Research.* 2006;34(suppl_1):D655-D8.

132. Yoshida T, and Owens GK. Molecular determinants of vascular smooth muscle cell diversity. *Circulation research.* 2005;96(3):280-91.

133. Scholzen T, and Gerdes J. The Ki-67 protein: from the known and the unknown. *J Cell Physiol.* 2000;182(3):311-22.

134. Lengsfeld AM, Löw I, Wieland T, Dancker P, and Hasselbach W. Interaction of phalloidin with actin. *Proceedings of the National Academy of Sciences.* 1974;71(7):2803-7.

135. Dobnikar L, Taylor AL, Chappell J, Oldach P, Harman JL, Oerton E, et al. Disease-relevant transcriptional signatures identified in individual smooth muscle cells from healthy mouse vessels. *Nature Communications.* 2018;9(1):4567.

136. Rong JX, Shapiro M, Trogan E, and Fisher EA. Transdifferentiation of mouse aortic smooth muscle cells to a macrophage-like state after cholesterol loading. *Proceedings of the National Academy of Sciences.* 2003;100(23):13531-6.

137. Morrow D, Guha S, Sweeney C, Birney Y, Walshe T, O'Brien C, et al. Notch and vascular smooth muscle cell phenotype. *Circulation research.* 2008;103(12):1370-82.

138. Li Y, Takeshita K, Liu P-Y, Satoh M, Oyama N, Mukai Y, et al. Smooth muscle Notch1 mediates neointimal formation after vascular injury. *Circulation.* 2009;119(20):2686-92.

139. Doi H, Iso T, Sato H, Yamazaki M, Matsui H, Tanaka T, et al. Jagged1-selective notch signaling induces smooth muscle differentiation via a RBP-Jκ-dependent pathway. *Journal of Biological Chemistry.* 2006;281(39):28555-64.

140. Fukuda D, Aikawa E, Swirski FK, Novobrantseva TI, Kotelianski V, Gorgun CZ, et al. Notch ligand delta-like 4 blockade attenuates atherosclerosis and metabolic disorders. *Proceedings of the national Academy of Sciences.* 2012;109(27):E1868-E77.

141. Hale AT, Tian H, Anih E, Recio FO, Shatat MA, Johnson T, et al. Endothelial Krüppel-like factor 4 regulates angiogenesis and the Notch signaling pathway. *Journal of Biological Chemistry.* 2014;289(17):12016-28.

142. Ghaleb AM, Aggarwal G, Bialkowska AB, Nandan MO, and Yang VW. Notch inhibits expression of the Krüppel-like factor 4 tumor suppressor in the intestinal epithelium. *Molecular Cancer Research.* 2008;6(12):1920-7.

143. Masia A, Almazan-Moga A, Velasco P, Reventós J, Torán N, Sanchez de Toledo J, et al. Notch-mediated induction of N-cadherin and α9-integrin confers higher invasive phenotype on rhabdomyosarcoma cells. *British journal of cancer.* 2012;107(8):1374-83.

144. Zheng X, Li A, Zhao L, Zhou T, Shen Q, Cui Q, et al. Key role of microRNA-15a in the KLF4 suppressions of proliferation and angiogenesis in endothelial and vascular smooth muscle cells. *Biochemical and biophysical research communications.* 2013;437(4):625-31.

145. Garvey SM, Sinden DS, Bortz PDS, and Wamhoff BR. Cyclosporine up-regulates Krüppel-like factor-4 (KLF4) in vascular smooth muscle cells and drives phenotypic modulation in vivo. *Journal of Pharmacology and Experimental Therapeutics.* 2010;333(1):34-42.

146. Wassmann S, Wassmann K, Jung A, Velten M, Knuefermann P, Petoumenos V, et al. Induction of p53 by GKLF is essential for inhibition of proliferation of vascular smooth muscle cells. *Journal of molecular and cellular cardiology.* 2007;43(3):301-7.

147. Stein MI, Zhu J, and Emerson SG. Molecular pathways regulating the self-renewal of hematopoietic stem cells. *Experimental hematology.* 2004;32(12):1129-36.

148. Alquier T, and Poitout V. Considerations and guidelines for mouse metabolic phenotyping in diabetes research. *Diabetologia.* 2018;61(3):526-38.

149. Fraulob JC, Ogg-Diamantino R, Fernandes-Santos C, Aguila MB, and Mandarim-de-Lacerda CA. A Mouse Model of Metabolic Syndrome: Insulin Resistance, Fatty Liver and Non-Alcoholic Fatty Pancreas Disease (NAFPD) in C57BL/6 Mice Fed a High Fat Diet. *J Clin Biochem Nutr.* 2010;46(3):212-23.

150. Ehrlund A, Acosta JR, Björk C, Hedén P, Douagi I, Arner P, et al. The cell-type specific transcriptome in human adipose tissue and influence of obesity on adipocyte progenitors. *Scientific data.* 2017;4(1):1-11.

151. Heilbronn L, Smith S, and Ravussin E. Failure of fat cell proliferation, mitochondrial function and fat oxidation results in ectopic fat storage, insulin resistance and type II diabetes mellitus. *International journal of obesity.* 2004;28(4):S12-S21.

152. Blüher M. Adipose tissue dysfunction contributes to obesity related metabolic diseases. *Best practice & research Clinical endocrinology & metabolism.* 2013;27(2):163-77.

153. Kokosar M, Benrick A, Perfilyev A, Fornes R, Nilsson E, Maliqueo M, et al. Epigenetic and transcriptional alterations in human adipose tissue of polycystic ovary syndrome. *Scientific reports.* 2016;6(1):1-18.

154. Mortensen SB, Jensen CH, Schneider M, Thomassen M, Kruse TA, Laborda J, et al. Membrane-tethered delta-like 1 homolog (DLK1) restricts adipose tissue size by inhibiting preadipocyte proliferation. *Diabetes.* 2012;61(11):2814-22.

155. Urs S, Turner B, Tang Y, Rostama B, Small D, and Liaw L. Effect of soluble Jagged1-mediated inhibition of Notch signaling on proliferation and differentiation of an adipocyte progenitor cell model. *Adipocyte.* 2012;1(1):46-57.

156. Surwit RS, Kuhn CM, Cochrane C, McCubbin JA, and Feinglos MN. Diet-induced type II diabetes in C57BL/6J mice. *Diabetes.* 1988;37(9):1163-7.

157. Wang C-Y, and Liao JK. *mTOR*. Springer; 2012:421-33.

158. Weisbrod RM, Shiang T, Al Sayah L, Fry JL, Bajpai S, Reinhart-King CA, et al. Arterial stiffening precedes systolic hypertension in diet-induced obesity. *Hypertension.* 2013;62(6):1105-10.

159. Lin M, Roth RA, Kozel BA, Mecham RP, and Halabi CM. Loss of Angiotensin II Type 2 Receptor Improves Blood Pressure in Elastin Insufficiency. *Front Cardiovasc Med.* 2021;8:782138.

160. Li P, Halabi CM, Stewart R, Butler A, Brown B, Xia X, et al. Sodium-activated potassium channels moderate excitability in vascular smooth muscle. *J Physiol.* 2019;597(20):5093-108.

161. Rhodes CJ, Wharton J, Swietlik EM, Harbaum L, Girerd B, Coghlan JG, et al. Using the Plasma Proteome for Risk Stratifying Patients with Pulmonary Arterial Hypertension. *American Journal of Respiratory and Critical Care Medicine.* 2022(ja).

162. Ansari N, Najafi S, Shahrabi S, and Saki N. PEAR1 polymorphisms as a prognostic factor in hemostasis and cardiovascular diseases. *J Thromb Thrombolysis.* 2021;51(1):89-95.

163. Eicher JD, Lettre G, and Johnson AD. The genetics of platelet count and volume in humans. *Platelets.* 2018;29(2):125-30.

164. Keramati AR, Yanek LR, Iyer K, Taub MA, Ruczinski I, Becker DM, et al. Targeted deep sequencing of the PEAR1 locus for platelet aggregation in European and African American families. *Platelets.* 2019;30(3):380-6.

165. Kim Y, Suktitipat B, Yanek LR, Faraday N, Wilson AF, Becker DM, et al. Targeted deep resequencing identifies coding variants in the PEAR1 gene that play a role in platelet aggregation. *PLoS One.* 2013;8(5):e64179.

166. Kunicki TJ, Williams SA, and Nugent DJ. Genetic variants that affect platelet function. *Current opinion in hematology.* 2012;19(5):371-9.

167. Jones CI, Bray S, Garner SF, Stephens J, de Bono B, Angenent WG, et al. A functional genomics approach reveals novel quantitative trait loci associated with platelet signaling pathways. *Blood.* 2009;114(7):1405-16.

168. Johnson AD, Yanek LR, Chen MH, Faraday N, Larson MG, Tofler G, et al. Genome-wide meta-analyses identifies seven loci associated with platelet aggregation in response to agonists. *Nat Genet.* 2010;42(7):608-13.

169. Nie XY, Li JL, Qin SB, Fu Y, Liang GK, Shi LW, et al. Genetic mutations in PEAR1 associated with cardiovascular outcomes in Chinese patients with acute coronary syndrome. *Thromb Res.* 2018;163:77-82.

170. Lewis JP, Ryan K, O'Connell JR, Horenstein RB, Damcott CM, Gibson Q, et al. Genetic variation in PEAR1 is associated with platelet aggregation and cardiovascular outcomes. *Circulation: Cardiovascular Genetics.* 2013;6(2):184-92.

171. Stimpfle F, Bauer M, Rath D, Schaeffeler E, Schwab M, Gawaz M, et al. Variants of PEAR1 are associated with outcome in patients with ACS and stable CAD undergoing PCI. *Frontiers in pharmacology.* 2018;9:490.

172. Kardeby C, Fälker K, Haining EJ, Criel M, Lindkvist M, Barroso R, et al. Synthetic glycopolymers and natural fucoidans cause human platelet aggregation via PEAR1 and GPIbα. *Blood Adv.* 2019;3(3):275-87.

173. Cadena DL, and Gill GN. Receptor tyrosine kinases. *The FASEB Journal.* 1992;6(6):2332-7.

174. Kardeby C, Damaskinaki F-N, Sun Y, and Watson SP. Is the endogenous ligand for PEAR1 a proteoglycan: clues from the sea. *Platelets.* 2021;32(6):779-85.

175. Scheib JL, Sullivan CS, and Carter BD. Jedi-1 and MEGF10 signal engulfment of apoptotic neurons through the tyrosine kinase Syk. *Journal of Neuroscience.* 2012;32(38):13022-31.

176. Sullivan CS, Scheib JL, Ma Z, Dang RP, Schafer JM, Hickman FE, et al. The adaptor protein GULP promotes Jedi-1-mediated phagocytosis through a clathrin-dependent mechanism. *Mol Biol Cell.* 2014;25(12):1925-36.

177. Wu H-H, Bellmunt E, Scheib JL, Venegas V, Burkert C, Reichardt LF, et al. Glial precursors clear sensory neuron corpses during development via Jedi-1, an engulfment receptor. *Nature neuroscience.* 2009;12(12):1534-41.

178. Sun Y, Vandenbriele C, Kauskot A, Verhamme P, Hoylaerts MF, and Wright GJ. A Human Platelet Receptor Protein Microarray Identifies the High Affinity Immunoglobulin E Receptor Subunit α (FcεR1α) as an Activating Platelet Endothelium Aggregation Receptor 1 (PEAR1) Ligand. *Mol Cell Proteomics.* 2015;14(5):1265-74.

179. Kardeby C, Damaskinaki FN, Sun Y, and Watson SP. Is the endogenous ligand for PEAR1 a proteoglycan: clues from the sea. *Platelets.* 2021;32(6):779-85.

180. Vandenbriele C, Sun Y, Criel M, Cludts K, Van kerckhoven S, Izzi B, et al. Dextran sulfate triggers platelet aggregation via direct activation of PEAR1. *Platelets.* 2016;27(4):365-72.

181. Letunic I, Khedkar S, and Bork P. SMART: recent updates, new developments and status in 2020. *Nucleic Acids Research.* 2020;49(D1):D458-D60.

182. Boughton AP, Welch RP, Flickinger M, VandeHaar P, Taliun D, Abecasis GR, et al. LocusZoom.js: interactive and embeddable visualization of genetic association study results. *Bioinformatics.* 2021;37(18):3017-8.

183. Wirka RC, Wagh D, Paik DT, Pjanic M, Nguyen T, Miller CL, et al. Atheroprotective roles of smooth muscle cell phenotypic modulation and the TCF21 disease gene as revealed by single-cell analysis. *Nature Medicine.* 2019;25(8):1280-9.

184. To WS, and Midwood KS. Plasma and cellular fibronectin: distinct and independent functions during tissue repair. *Fibrogenesis & Tissue Repair.* 2011;4(1):21.

185. Tikhonova AN, Dolgalev I, Hu H, Sivaraj KK, Hoxha E, Cuesta-Domínguez Á, et al. The bone marrow microenvironment at single-cell resolution. *Nature.* 2019;569(7755):222-8.

186. Branon TC, Bosch JA, Sanchez AD, Udeshi ND, Svinkina T, Carr SA, et al. Efficient proximity labeling in living cells and organisms with TurboID. *Nature Biotechnology.* 2018;36(9):880-7.

187. Davis GE, and Senger DR. Endothelial extracellular matrix: biosynthesis, remodeling, and functions during vascular morphogenesis and neovessel stabilization. *Circ Res.* 2005;97(11):1093-107.

188. Scheib JL, Sullivan CS, and Carter BD. Jedi-1 and MEGF10 signal engulfment of apoptotic neurons through the tyrosine kinase Syk. *J Neurosci.* 2012;32(38):13022-31.

189. Kirchhausen T, Macia E, and Pelish HE. Use of dynasore, the small molecule inhibitor of dynamin, in the regulation of endocytosis. *Methods Enzymol.* 2008;438:77-93.

190. Ridley AJ, Schwartz MA, Burridge K, Firtel RA, Ginsberg MH, Borisy G, et al. Cell migration: integrating signals from front to back. *Science.* 2003;302(5651):1704-9.

191. Holz MK, and Blenis J. Identification of S6 kinase 1 as a novel mammalian target of rapamycin (mTOR)-phosphorylating kinase. *J Biol Chem.* 2005;280(28):26089-93.

192. Trevisan AJ, Bauer MB, Brindley RL, Currie KPM, and Carter BD. Jedi-1 deficiency increases sensory neuron excitability through a non-cell autonomous mechanism. *Sci Rep.* 2020;10(1):1300.

193. Criel M, Izzi B, Vandenbriele C, Liesenborghs L, Van Kerckhoven S, Lox M, et al. Absence of Pear1 does not affect murine platelet function in vivo. *Thromb Res.* 2016;146:76-83.

194. Zheng J, Baird D, Borges M-C, Bowden J, Hemani G, Haycock P, et al. Recent developments in Mendelian randomization studies. *Current epidemiology reports.* 2017;4(4):330-45.

195. Ferkingstad E, Sulem P, Atlason BA, Sveinbjornsson G, Magnusson MI, Styrmisdottir EL, et al. Large-scale integration of the plasma proteome with genetics and disease. *Nature genetics.* 2021;53(12):1712-21.

196. Auton A, Brooks LD, Durbin RM, Garrison EP, Kang HM, Korbel JO, et al. A global reference for human genetic variation. *Nature.* 2015;526(7571):68-74.

197. Hemani G, Zheng J, Elsworth B, Wade KH, Haberland V, Baird D, et al. The MR-Base platform supports systematic causal inference across the human phenome. *Elife.* 2018;7.

198. Kim DI, Jensen SC, Noble KA, Kc B, Roux KH, Motamedchaboki K, et al. An improved smaller biotin ligase for BioID proximity labeling. *Mol Biol Cell.* 2016;27(8):1188-96.

199. Erde J, Loo RR, and Loo JA. Improving Proteome Coverage and Sample Recovery with Enhanced FASP (eFASP) for Quantitative Proteomic Experiments. *Methods Mol Biol.* 2017;1550:11-8.

200. Chen ZW, Fuchs K, Sieghart W, Townsend RR, and Evers AS. Deep amino acid sequencing of native brain GABAA receptors using high-resolution mass spectrometry. *Mol Cell Proteomics.* 2012;11(1):M111.011445.

201. Wiśniewski JR, Zougman A, Nagaraj N, and Mann M. Universal sample preparation method for proteome analysis. *Nat Methods.* 2009;6(5):359-62.

202. Meier F, Brunner AD, Koch S, Koch H, Lubeck M, Krause M, et al. Online Parallel Accumulation-Serial Fragmentation (PASEF) with a Novel Trapped Ion Mobility Mass Spectrometer. *Mol Cell Proteomics.* 2018;17(12):2534-45.

203. Perkins DN, Pappin DJ, Creasy DM, and Cottrell JS. Probability-based protein identification by searching sequence databases using mass spectrometry data. *Electrophoresis.* 1999;20(18):3551-67.

204. Singh S, Tank NK, Dwiwedi P, Charan J, Kaur R, Sidhu P, et al. Monoclonal antibodies: a review. *Current clinical pharmacology.* 2018;13(2):85-99.